Bipolar Cascade Lasers

by

Steven G. Patterson

B.S. University of Cincinnati (1993)
S.M. Massachusetts Institute of Technology (1995)

Submitted to the
Department of Electrical Engineering and Computer Science
In partial fulfillment of the requirements for the degree of

Doctor of Philosophy

at the

MASSACHUSETTS INSTITUTE of TECHNOLOGY

SEPTEMBER 2000

Author _____
Department of Electrical Engineering and Computer Science
July 31, 2000

Certified by _____
Rajeev J. Ram
Professor of Electrical Engineering
Thesis Supervisor

Accepted by _____
Arthur C. Smith
Chairman, Department Committee on Graduate Students

Bipolar Cascade Lasers

by

Steven G. Patterson

Submitted to the Department of Electrical Engineering and Computer Science
on August 4, 2000 in Partial Fulfillment of the
Requirements for the Degree of Doctor of Philosophy in
Electrical Engineering

ABSTRACT

This thesis addresses issues of the design and modeling of the Bipolar Cascade Laser (BCL), a new type of quantum well laser. BCLs consist of multiple single stage lasers electrically coupled via tunnel junctions. The BCL ideally operates by having each injected electron participate in a recombination event in the topmost active region, then tunnel from the valence band of the first active region into the conduction band of the next active region, participate in another recombination event, and so on through each stage of the cascade. As each electron may produce more than one photon the quantum efficiency of the device can, in theory, exceed 100%. This work resulted in the first room temperature, continuous-wave operation of a BCL, with a record 99.3% differential slope efficiency. The device was fully characterized and modeled to include light output and voltage versus current bias, modulation response and thermal properties. A new single-mode bipolar cascade laser, the bipolar cascade antiresonant reflecting optical waveguide laser, was proposed and modeled.

Thesis Supervisor: Rajeev J. Ram
Title: Professor of Electrical Engineering

Acknowledgements

The graduate experience varies greatly amongst students for a variety of reasons, not the least of which is one's faculty advisor. In this regard I have been most fortunate. Rajeev was kind enough to take me on as a student late in my graduate career, provided tremendous guidance throughout the course of this work, is truly gifted in his amazing physical insight which he readily shares, has always seemed to remember that graduate school is also about educating students and, perhaps most importantly, supported me when others might have (and did) run for cover.

I'd like to thank my thesis committee, Terry Orlando and Shaoul Ezekiel, for reading the thesis and making numerous helpful comments. Thanks to Terry for also attempting to provide valuable help at a more difficult time during this thesis work.

My most sincere appreciation goes to the members of my research group. I'd like to thank Matthew for his sense of humor, for always being supportive, for always having something positive to say, for getting everything together the day of my defense, and for never turning me away whenever I needed a friendly ear. Erwin always seemed to have something nice to say about everyone, even me, and provided entertaining and lively conversation about women, dating and many other aspects of life. Erwin deserves special mention for daring to be different, particularly in an institution that (despite its remonstrations to the contrary) admires only homogeneity in thought and action. Harry generated plenty of laughter and good will through his boyish enthusiasm and charm, was always eager to help out even without being asked, saved me endless hours of mindless drudgery through his mastery of Matlab and Labview, and often reminded me that engineering can still be fun. Kevin was a breath of fresh air to the group bringing in an enthusiasm for things outside the lab, filling me in on the many aspects of life in Cambridge, Boston and at MIT. Thanks also to Kevin for tolerating the mini-music (especially the country stuff), oh and of course, for being the only really normal guy in the group. My first impressions of Margaret (a.k.a. Bob) were of an extremely warm and sweet person and these initial impressions have only grown stronger with time. Her genuine smile and easy going manner, not to mention her baking, have made her presence in and about the lab a delight. Farhan's mastery of condensed matter physics, his willingness to share his knowledge of the same and our common ground of prior military service made for many interesting and fruitful interactions. A special thanks to Holger for maintaining the soft spoken and humble manner with which he arrived, particularly in an institution that seems to honor pomposity and arrogance above all else. Peter is relatively new to the group and the unfortunate paucity of available time has not permitted a closer acquaintance but his friendly manner and insightful questions have made him a welcome addition to the group.

I have been equally blessed to have acquired so many wonderful friends over the years. Dave, as different as we may be, has remained a true friend over the years, providing countless hours of conversation and a tireless patience with my miscellaneous ramblings. Thanks also, in no small measure, for the splendid bottle of scotch. Amy has helped me better understand the other half, always seemed to be in the office during her MIT years whenever I needed a quick chat or to share a cup of coffee, and embraces life in a manner which I find truly inspiring. Enrique, the salsa king of Boston, livened my days at MIT with many a trip to the Muddy, by continuing to attempt to teach me to

dance even when I was clearly a danger to myself and those around me, and by just being what is best described as a buddy. Mark has helped me prove that there is indeed hope for the world if a highly intelligent, double majoring, avowed liberal, Rhodes Scholar, professor of physics could provide such enduring friendship to such an uncredentialed, barely made it to college, Neanderthal former Ranger-type. Glenn I met as an undergrad while interning and it is through his encouragement that I realized that MIT was not beyond my grasp. He has remained a dear friend in spite of the large physical distance separating us over the years. Reggie is the sort of friend whom, no matter the length of time since we last spoke, immediately allows me to feel at home, welcome and reconnected. Bob and Kirstin have been supportive beyond mere description in words and no amount of space is adequate to do justice to the contributions they've made over the years to the betterment of my life. Felicia has always been a source of inspiration, encouraging me long ago to take the road which brought to where I am today. It would be hard to imagine a better sister. My parents taught me long ago about the importance of self-reliance and that hard work eventually does indeed pay off.

Finally, I'd like to express my continuing admiration for the men, past, present and future, of the Ranger Regiment. It is there that I learned almost everything of intrinsic value in life. The rest has been mere technical details.

Contents

List of Figures:

List of Tables:

Chapter 1: Introduction

1. Introduction

Semiconductor lasers are becoming increasingly pervasive in a wide variety of fields. They have become an enabling technology in areas as diverse as basic science, telecommunications, medicine, atmospheric sensing, manufacturing, home entertainment and beyond. In each case the laser's properties are engineered to meet the requirements of the specific task at hand; everything from the laser's output power, modulation bandwidth, and emission wavelength to thermal properties, differential slope efficiency, and threshold current may be optimized by the clever designer. Until fairly recently one element of the laser's properties remained beyond the control of the laser engineer, however. For each electron injected into the laser one could hope to get but a single photon from the laser.

The ratio of the number of emitted photons to the number of electrons injected into the semiconductor laser is known as the quantum efficiency of the device [1]. If each injected electron produces a single output photon the device has a quantum efficiency of 100%. In practice, for conventional semiconductor lasers, it is never the case that a quantum efficiency of 100% is achieved. Some of the electrons injected into the laser do not reach the active region, others reach it but leak out before they can combine with a hole in a radiative emission process. Other electrons recombine with holes in non-radiative processes. Even when the electron produces a photon it may not couple out of the laser's optical cavity before being lost through absorption or scattering at an interface. Photons may also emit into modes of the optical cavity other than the desired lasing mode. Even very careful design, where all the latter mentioned processes are carefully engineered to ensure maximum conversion of injected electrons to photons and maximum output coupling of the photons, has only resulted in a peak slope efficiency of 97.6% at an emission wavelength of 806 nm [2].

Most applications are in some way sensitive to the lasers quantum efficiency. In particular, for optical links requiring direct modulation of the semiconductor laser, the signal-to-noise ratio of the link goes to the square of the laser's quantum efficiency [3].

It is therefore desirable to build lasers that maximize the device's quantum efficiency; specifically, to build lasers that are capable of emitting more than one photon for each injected electron. Recently a class of laser, known as the cascade laser, has been developed which allows more than one photon to be emitted for each injected electron.

1.1 Cascade lasers

A number of different types of cascade lasers exist. There are unipolar (intraband) cascade lasers [4], type-II bipolar (interband) cascade lasers [5], and type-I bipolar (interband) cascade lasers [6]. The first uses only electrons in the stimulated emission process (hence the name unipolar), while the latter two use both electrons and holes (bipolar) in indirect and direct interband transitions, respectively. Independent of type, all cascade lasers operate on a similar principle. An injected electron goes through a radiative transition, then quantum mechanically tunnels from a low energy state to a high energy state where it may participate in another recombination event and so on through each stage of the cascade. In this way more than one photon may be emitted for each injected electron. Cascade lasers are capable of demonstrating voltage, incremental resistance, and differential slope efficiencies that are ideally the sum of the individual laser junctions in the cascade.

Fig.1-1 shows a schematic of a unipolar cascade laser. The laser operates by the injection of an electron into a gain section consisting of one or more quantum wells. The gain section has been bandgap engineered so that the electron participates in an intersubband (intraband) transition. A superlattice section lies adjacent to the gain layers acting as a forbidden region to prevent the electron from escaping the gain section prior to recombining. After recombining the electron may tunnel to the next gain section and so on through the cascade.

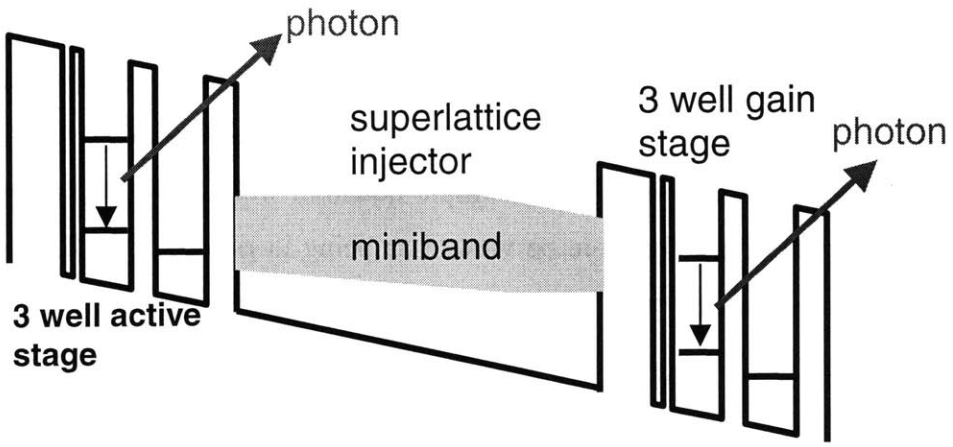

Figure 1-1. A unipolar cascade laser. Each gain stage is separated from the next by a superlattice. The superlattice miniband serves as a blocking layer to prevent carrier leakage from the active stages prior to intraband radiative recombination. The electron then tunnels to the next stage and so on through the cascade.

Fig. 1-2 shows a schematic of a type-II bipolar cascade laser. In this type of cascade laser the electron participates in an *indirect* transition between the conduction and valence band prior to the tunneling process which allows the electron to continue down the cascade. In both the unipolar cascade laser and the type-II bipolar cascade laser the emission wavelength is in the range of 2-10 μm. In order to reach wavelengths more compatible with those required by telecommunications systems the use of direct interband transitions is dictated.

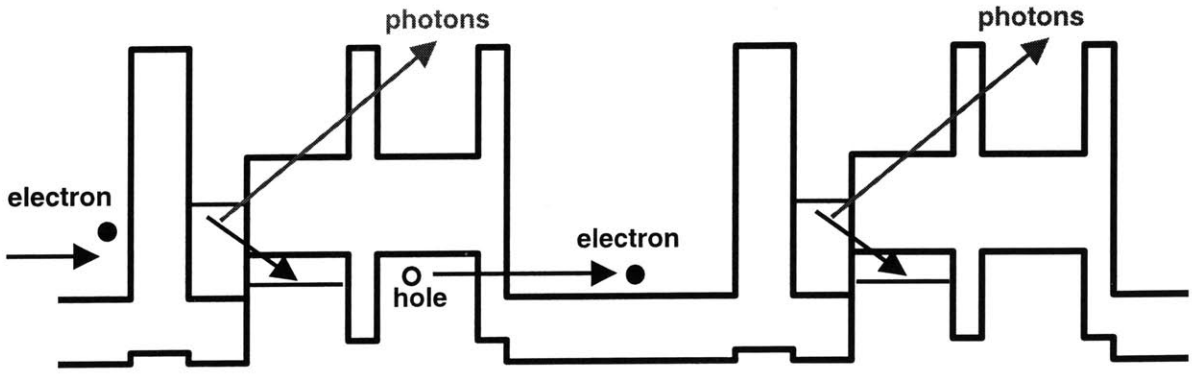

Figure 1-2. The type-II bipolar cascade laser. The radiative transitions are interband (conduction-to-valence band) but are indirect. This type of cascade laser is also referred to as a broken gap device.

The primary aim of this work was the investigation of direct interband transition bipolar cascade laser, heretofore referred to simply as the bipolar cascade laser (BCL). In order to better appreciate the difference between a conventional multiple quantum well laser and a BCL the reader is referred to Fig. 1-3. In the conventional laser an injected electron may go into any *one* of the multiple quantum wells, but never more than one. The quantum wells may therefore be viewed as being in *parallel.* This is conceptually equivalent to the arrangement of Fig. 1-4, wherein three single quantum well diode lasers are electrically attached in parallel with a single current source. Fig. 1-5 shows a three quantum well (or, equivalently, three gain section) BCL. In this case the injected electron can participate in a recombination event in the first quantum well, quantum mechanically tunnel from the valence band of the first gain section to the conduction band of the second gain section, and on through to the third gain section. In this case the electron goes through *all* the quantum wells and they are seen as being connected in *series.*

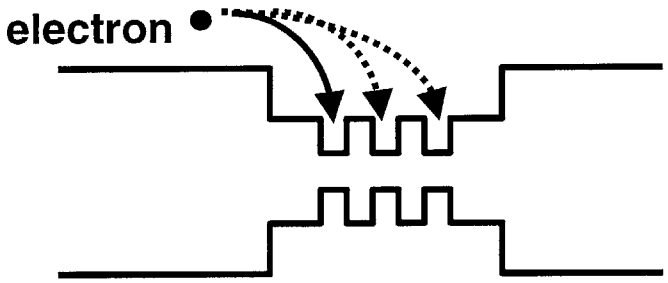

Figure 1-3. In a conventional multiple quantum well laser an injected electron may go into any one of the quantum wells and recombine, but only one. The wells can be viewed as being connected in parallel.

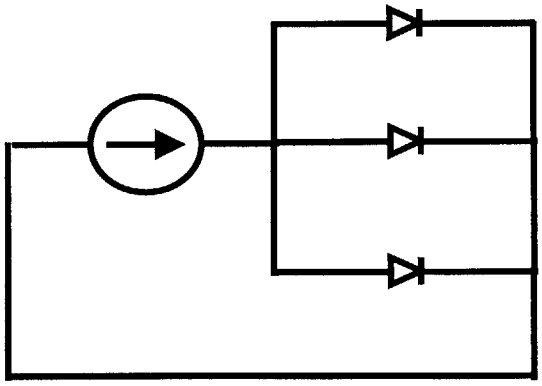

Figure 1-4. The circuit equivalent of Fig. 1-3. Each diode is a single quantum well laser.

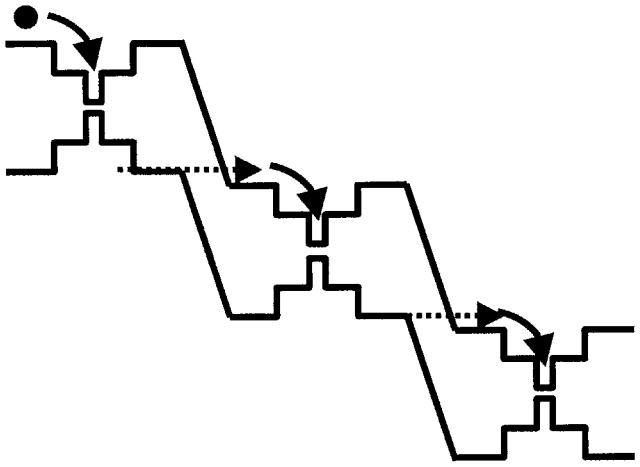

Figure 1-5. A cascade laser. The laser contains three quantum wells as in Fig.3 but now each electron may recombine in the first well, tunnel to the next well and so on through the cascade. The quantum wells may then be seen as being electrically in series.

Fig. 1-6 shows the discrete circuit schematic of the latter described device. Several diode lasers are connected in series with a single current source. Assuming that enough photons can be generated (by connecting a sufficiently large number of lasers in series) to compensate for any loss in transporting the photons to a photodetector, it is conceivable that more electrons will be generated at the receiver than were put in at the source. This results in the concept of radio frequency (RF) gain. More signal electrons are detected than are put in to the source laser. It is important to realize that this is not "creating energy". The voltage drop across the series connected diodes is equal to N times the voltage drop across a single diode, where N is the number of diodes in series. Gain only occurs in the "small signal" sense.

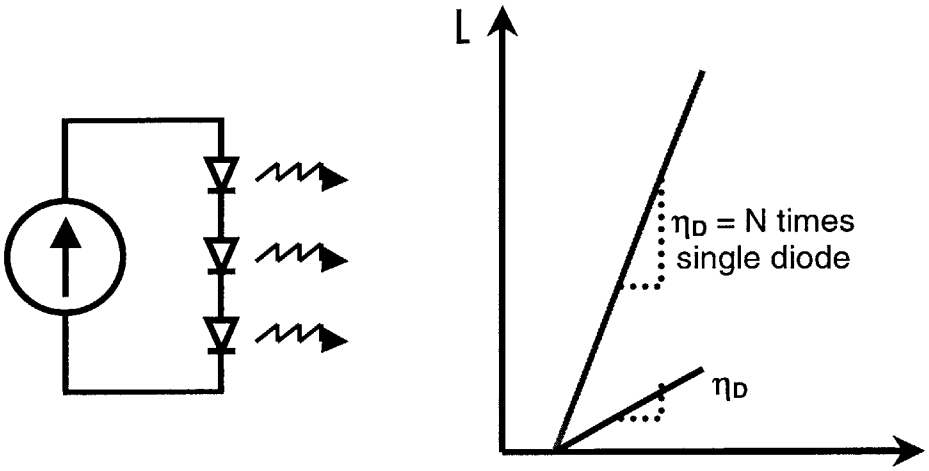

a) b)

Figure 1-6. a) The circuit equivalent of Fig. 1-5. b) The result of placing the quantum wells in series is to increase the slope efficiency of the device from η to $N \cdot \eta_D$, where N is the number of stages in the cascade.

Fig. 1-7a shows the realization of this concept using off-the-shelf Fujitsu distributed feedback lasers [5]. The lasers were electrically coupled in series via wire bonding. The output of each laser was coupled into a single mode fiber, and the fiber bundle was end-coupled into a broad area photodiode. Link transparency (i.e. one electron was detected for each electron injected) was achieved with four lasers in the series and link gain (i.e. more than one electron was detected for each injected electron) was achieved with five and six lasers in the cascade (Fig. 1-7b). A concomitant reduction in the noise figure of the cascade was measured with each additional laser in the cascade. Unfortunately, the parasitics introduced by the bonding of the lasers in series reduced the modulation bandwidth from the 3 GHz obtainable using a single laser to only 50 MHz for the series cascade. A more viable approach is to achieve the electrical series connection of the individual lasers during the epitaxial process through the use of highly doped tunnel junctions. This thesis concerns itself with such devices.

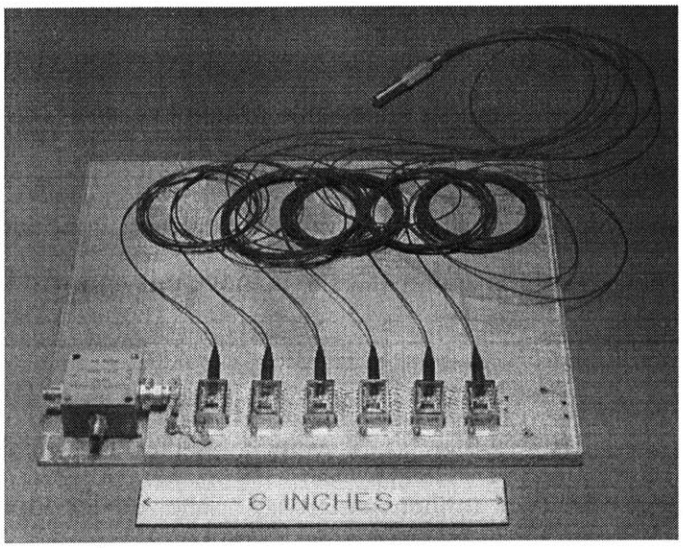

a)

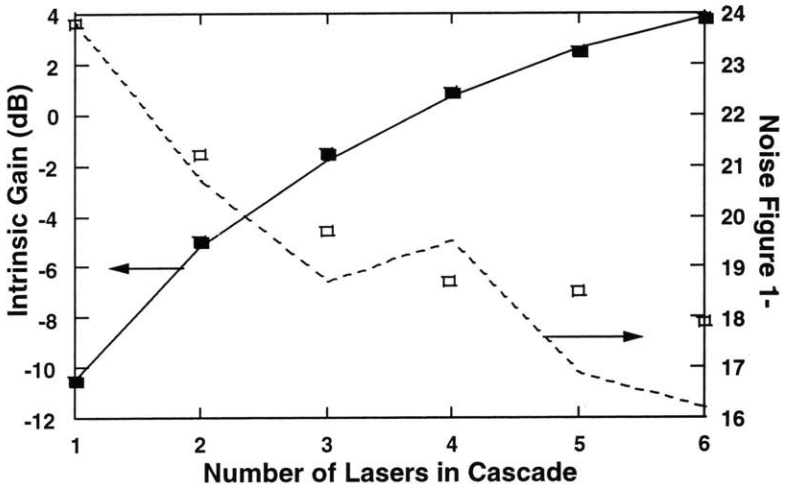

b)

Figure 1-7. a) The proof-of-concept experimental set-up used in generating the data of Fig. 1-7 b. Off-the-shelf Fujitsu distributed feedback lasers were connected in series via wire bonding. Each laser was individually coupled into a single-mode optical fiber. The fiber bundle was end coupled into a broad area photodetector. b) With 4 lasers in the cascade, link transparency was achieved (1 electron injected for each electron detected). Using 5 and 6 lasers in the cascade resulted in link gain (more than one electron detected for each electron injected). Increasing the number of lasers in the cascade also reduced the noise figure. Each laser had a modulation bandwidth of 3 GHz but the cascade bandwidth was only 50 MHz. [5]

1.2 A brief history of bipolar cascade lasers

It is worthwhile to consider the historical evolution of the BCL. While all the devices described below operate on the same principle each is different from the others in some critical way. Careful study of each of these devices indicated the design flaws that prevented them from demonstrating room temperature, continuous wave performance. The necessary design details and physics to achieve this end will be addressed thoroughly in Chapters 2 and 3.

The BCL was first introduced by van der Ziel, et al. in 1982 [6]. Three bulk 850 nm active region edge emitting lasers were connected electrically in series during the epitaxial process via two tunnel junctions. The device operated pulsed at room temperature with a duty cycle of ~0.1%. A differential efficiency of 80% was achieved.

Little was done with the concept until Garcia, et al. [7] realized a similar device with an eye toward high power arrays in 1997. The devices consisted of a two-stage cascade operating at 950 nm in the topmost junction and 980 nm in the bottom most junction. The active regions were made of three quantum wells each. These devices also operated room temperature and pulsed. A differential efficiency of 79% was achieved.

Kim, et al. [10] also achieved room temperature pulsed operation of a three-stage device operating at 1.55 μm in 1999. This edge emitter was unique in that all of the three gain stages were contained inside of a single waveguide. A pulsed slope efficiency of 125% was obtained.

BCL designs were not limited to edge emitters. Schmid, et al. [8] achieved continuous wave operation of a two stage BCL in a vertical cavity surface emitting laser (VCSEL) at an operating temperature of 95 K in 1998. Two gain sections of three quantum wells each were cascaded at an emission wavelength of 980 nm.

We achieved the first room temperature, continuous wave operation of a BCL [9]. A two-stage device operating at 990 nm achieved a quantum efficiency of 99.3%. Since that time a continuous wave, room temperature demonstration of a BCL VCSEL has been made by T. Knödl, et al. [12] at 980 nm and a room temperature pulsed VCSEL by Kim, et al. [11] at 1.55 μm.

1.3 An alternative: the gain lever laser

As outlined above, the BCL has been the focus of extensive research in recent years. Another laser design capable of producing RF gain, the gain lever laser, has also been extensively studied [13,14]. In this section a qualitative description of the physics needed to understand the gain lever laser is given. The interested reader is referred to Appendix B where a more quantitative treatment is presented.

A schematic of the gain lever laser is shown in Fig. 1-8a. The gain lever laser makes use of the nonlinear gain versus carrier density for a quantum well as shown in Fig. 1-8b. In the gain lever laser there are two separate gain sections biased to different points on the gain curve as shown in Fig. 1-8. When a modulation is applied to gain section A it briefly increases its optical gain. Since the total gain of the laser structure must be maintained just below the total optical losses, section B must reduce its gain by reducing the carrier density in the quantum well active region. The laser is biased by a constant current source, implying section B must reduce its carrier density by radiative carrier transitions; i.e. the emission of photons. Since section A is biased at a point of higher differential gain ($dg_A/dN > dg_B/dN$) small carrier density modulations of section A lead to relatively large carrier density modulations in section B. The large output modulation resulting from the small input modulation yields small signal gain (increased differential efficiency. For reasons that won't be discussed at length here, the gain lever laser suffers from some problems when used in its intended application. Very short cavity lengths (200-300 μm) must be used in order to limit the photon lifetime and achieve reasonable modulation bandwidths [15]. Furthermore, due to the physics of the carrier lifetime the gain lever effect only occurs for modest output power [15]. Most importantly, the fact that the laser's gain is not clamped leads to appreciable signal distortion and the gain lever has not found acceptance in actual applications [16]. Nevertheless, it is a truly clever idea and well worth mentioning.

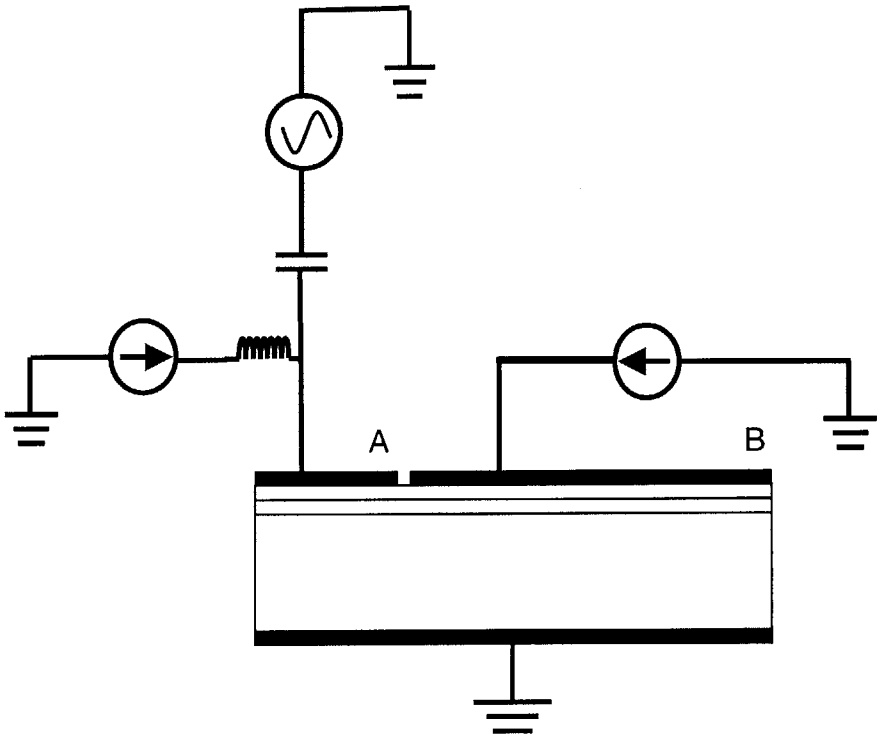

a)

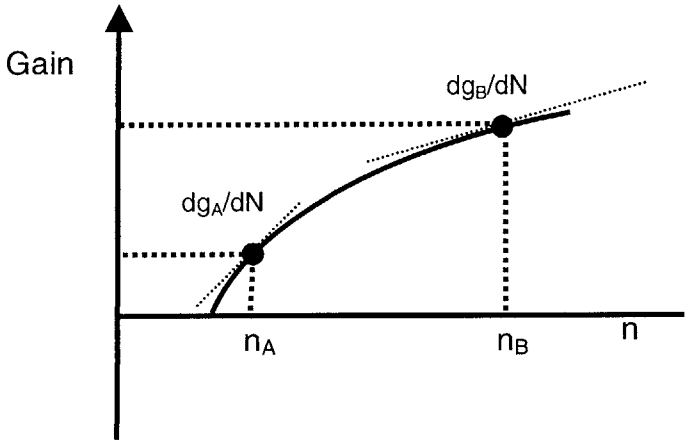

b)

Figure 1-8. a) The gain lever laser. Sections A and B are biased to different points of the gain curve of b). A small signal modulation is applied to section A. The differential gain at bias point A (dg_A/dN) is much larger than at point B (dg_A/dN). Small changes to the bias point at A lead to very large changes at B, and hence small signal gain is achieved.

1.3.1 Achieving RF gain by other means

It is worthwhile to mention that it is possible to achieve RF gain by considering components of the optical link external to the laser itself. While such methods are beyond the interests of this thesis they are briefly presented here for completeness. One such method is known as transformer matching [17]. This method achieves RF gain by using a transformer at the input to match the signal current source to the laser and another transformer to match the detector to the load. While this method can achieve substantial gain, it can do so only over a relatively narrow band of frequencies as set by the Bode-Fano limit [17].

A second such technique uses external modulation to realize gain in the optical link [17]. In external modulation the output of a shot noise limited laser is passed through an electro-optic modulator. A figure 1-of merit for the modulator, V_π, indicates the voltage that must be placed across the modulator to bring the output light power to zero. The achievable link gain goes to the square of the ratio of the laser optical power to V_π, thereby dictating a minimum amount of laser optical power in order to achieve link gain. In many applications the necessary amount of optical power may be unacceptably high. Additionally, the use external modulators may be cost prohibitive for some systems. The bipolar cascade laser then warrants study both as a viable technology in low-power, direct modulation optical links and to gain a greater appreciation of the properties of this new class of semiconductor laser.

1.4 Dissertation Overview

The keystone element of the BCL is the tunnel junction which electrically connects the gain stages. Chapter 2 begins by qualitatively discussing the underlying physics and modeling of the semiconductor tunnel junction. The characteristics of the junctions are then quantitatively modeled. The growth and materials issues associated with making high electrical quality tunnel junctions to include deep state effects are then addressed. Chapter 2 concludes with a discussion of the band structure of the BCL.

Chapter 3 begins with a review of the basic laser physics relevant to the BCL. Determining the conditions compatible with the growth of high quality active regions and tunnel junctions proved to be an early challenge in achieving a room temperature, continuous wave BCL. The details of the materials considerations necessary to grow a BCL structure within the constraints imposed by the available resources are therefore discussed next in Chapter 3. The light power versus current, current versus voltage, modulation and thermal properties of the first generation BCL follow next. The results of these studies of the first BCL led to a redesign of the BCL structure. This design of this device is presented in the final section of Chapter 3.

The intended application for the BCL requires efficient coupling into single mode fiber, an end not readily achievable using the designs discussed in Chapter 3. Chapter 4 begins by discussing the theory associated with a new type of device, the bipolar cascade antiresonant reflecting optical waveguide (ARROW) laser. Calculations of the threshold current, near and far fields patterns, radiation and absorption loss, and the effect of the number of quantum wells are presented.

Chapter 5 summarizes the work of this thesis and highlights its major contributions. Chapter 5 concludes with a discussion of directions for future work in the area of bipolar cascade lasers.

References:

[1] L.A . Coldren, S. W. Scott, "Diode lasers and photonic integrated circuits", John Wiley and Sons, Inc., 1995.

[2] J. Wang, B. Smith, X. Xie, X. Wang, and G. T. Burnham, "High-efficiency diode lasers at high output power", App. Phys. Lett., vol. 74, no. 11, 1525-1527, 1999.

[3] C. Cox III, E. Ackerman, R. Helkey, G. E. Betts, "Techniques and performance of Intensity-Modulation Direct-Detection Analog Optical Links", IEEE Trans. on Micro. Theory and Tech., vol. 45, no. 8, 1375-1383, 1997.

[4] J. Faist, F. Capasso, D. L. Sivco, C. Sirtori, A. L. Hutchinson, A. Y. Cho, "Quantum Cascade Laser", Science, vol. 264, 553-555, 1994.

[5] C. H. Cox III, H. V. Roussell, R. J. Ram, R. J. Helkey, "Broadband, directly modulated analog fiber link with positive intrinsic gain and reduced noise figure", IEEE International Topical Meeting on Microwave Photonics, Technical Digest, Piscataway, NJ, 157-60, 1998.

[6] B. H. Yang, D. Zhang, R. Q. Yang, S. S. Pei, Appl. Phys. Lett., vol. 72, no. 18, 2220-2222,1998.

[7] J. P. van der Ziel, W.T. Tsang, "Integrated multilayer GaAs lasers separated by tunnel junctions," App. Phys. Lett., vol. 41, 499-501, 1982.

[8] Ch. Garcia, E. Rosencher, Ph. Collot, N. Luarent, J. Guyaux, B. Vinter, J. Nagle, "Epitaxially stacked lasers with Esaki junctions: A bipolar cascade laser," App. Phys. Lett., vol. 71, no. 26, 3752-3754, 1997.

[9] J. K. Kim, E. Hall, O. Sjolund, L. A. Coldren, "Epitaxially-stacked multiple-active-region 1.55 μm lasers for increased differential efficiency", App. Phys. Lett., vol. 74, no. 22, 3251-3253, 1999.

[10] W. Schmid, D. Wiedenmann, M. Grabherr, R. Jager, R. Michalzik, K.J. Ebeling, "CW operation of a diode cascade InGaAs quantum well VCSEL," Elec. Lett., vol. 34, no. 34, 553-556, 1998.

[11] S. G. Patterson, G. S. Petrich, R. J. Ram, and L. A. Kolodziejski, "Continuous-wave room temperature operation of bipolar cascade laser", Elec. Lett., vol. 35, no. 5, 395-397, 1999.

[12] T. Knodl, R. Jäger, M. Grabherr, R. King, M. Kicherer, M. Miller, F. Merderer, and K. J. Ebeling, "CW room temperature operation of a diode cascade InGaAs-AlGaAs quantum well VCSEL", 1999 IEEE LEOS Conf. Proceed., Piscataway, NJ, vol.1, 143-1444, 1999.

[13] K. J. Vahala, M. A. Newkirk, and T. R. Chen, "The optical gain lever: A novel gain mechanism in the direct modulation of quantum well semiconductor lasers", Appl. Phys. Lett., vol. 64, no. 25, 2506-2508, 1989.

[14] N. Moore, and K. Y. Lau, "Ultrahigh efficiency microwave signal transmission using tandem-contact single quantum well GaAlAs lasers", Appl. Phys. Lett. Vol. 55, no. 4, 936-938, 1989.

[15] K. Y. Lau, "Dynamics of quantum well lasers", in Quantum well lasers, P. S. Zory, Jr., ed., Academic Press, Inc., 1993.

[16] L. D. Westbrook, C. P. Seltzer, "Reduced intermodulation-free dynamic range in gain-lever lasers", Elec. Lett., vol. 29, no. 5, 488-489, 1993.

[17] C. H. Cox III, E. Ackerman, R. Helkey, G. E. Betts, "Techniques and performance of intensity-modulation direct-detection analog optical links", IEEE Trans. On Microwave Theory and Tech., vol. 45, no. 8, 1375-1383, 1997.

Chapter 2: Semiconductor Tunnel Junctions

2.0 Introduction

The semiconductor tunnel junction was first investigated by Esaki [1]. While studying the internal field emission in a degenerate germanium p-n junction, he discovered that a portion of the forward bias current–voltage characteristic had a region of negative differential resistance. Since its discovery, the tunnel junction has been developed into a mature technology in the field of microwave and millimeter wave electronics. The region of negative differential resistance present in the current versus voltage characteristics of these devices has been exploited in making high frequency oscillators.

The tunnel diode is a majority carrier effect device. It is capable of high modulation speeds because the transport time is not given by the classical value $\tau = W/v$ where τ is the transport time, W the width of the junction, and v the velocity of the particle. It is shown in [2] that the tunneling time is proportional to exp(2k(0)W) where k(0) is the average value of the momentum encountered in the tunneling path corresponding to an incident carrier with zero transverse momentum and energy equal to the Fermi energy. This tunneling time is very short compared with any other transport time in the device and hence allows the tunnel junction to be used in devices out to the millimeter wave regime (~300 GHz).

When employed in the BCL, tunnel junctions are operated in the reverse bias regime. Their use in this mode of operation allows electrons to tunnel from the valence band of one gain section into the conduction band of the next gain section. The tunnel junction is the keystone element in the bipolar cascade laser as it permits the cascading to take place between, what are in practice, ordinary edge emitting lasers. Section 2.1 provides a phenomenological description of the physics of the tunnel junction. In Section 2.2 the numerical modeling of the tunnel junction and some non-idealities of the tunnel junctions are presented. The interested reader is referred to Appendix A where the necessary mathematical and physical background is provided to arrive at the starting point of Section 2.2. While the fundamental physics of the tunnel junction has been well

understood for some time now, its implementation in an epitaxially grown structure does present some interesting materials challenges. These challenges are the topic of Section 2.3. Section 2.4 details the band diagram of a two gain stage BCL at equilibrium and under bias. Section 2.5 concludes by summarizing the major results of the chapter.

2.1 Tunnel Junctions

Fig. 2-1 shows the band diagram of a tunnel junction at zero bias (and zero temperature for demonstrative purposes). Both the n-doped and p-doped sides of the junction are degenerately doped. Typically, doping levels are used such that the depletion width of the p-n junction is on the order of 100-200 Å. Equivalently, the peak of the built-in electric field is of the order of 10^6-10^7 V/cm. Fig. 2-1a shows the locations of the degenerately doped junctions at equilibrium while Fig. 2-1b shows the tunnel diode current versus voltage (I-V) characteristics. As a forward bias is applied, the quasi-Fermi level on the n-doped side raises with respect to the quasi-Fermi level on the p-doped side of the junction. Assuming the barrier width and height are both sufficiently small, an electron from the n-doped side of the junction may now tunnel to an empty state on the p-doped side of the junction. As the forward bias is increased the number of occupied states on the n-doped side of the junction aligned with unoccupied states on the p-doped side of the junction increases yielding a monotonically increasing current. Fig. 2-2a shows the current-voltage characteristics of the tunnel. Fig. 2-2a shows the junction in the forward bias regime at the current maximum.

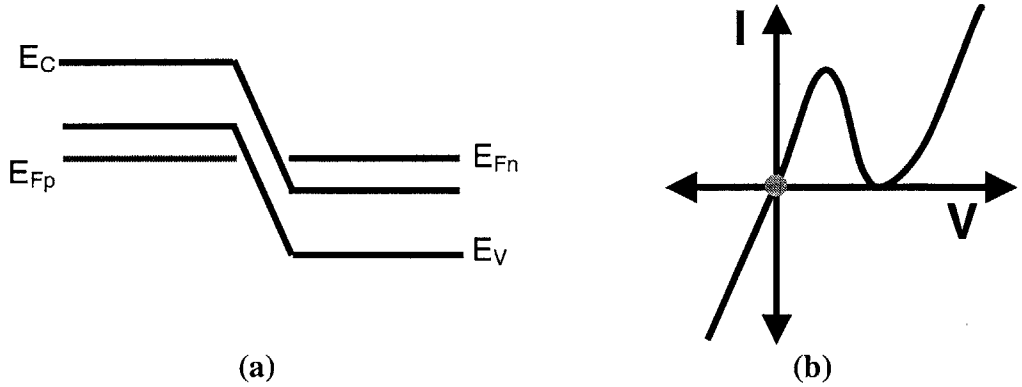

Figure 2-1. a) The unbiased p-n tunnel junction. Both the n- and p-sides are degenrately doped. b) The current versus voltage characterisitcs of the tunnel junction.

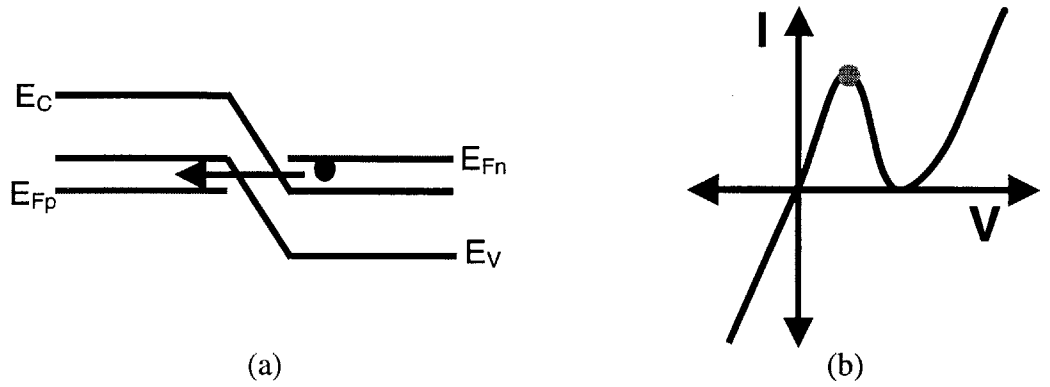

Figure 2-2. a) The tunnel diode under forward bias. At this bias point the maximum number of filled states on the n-side are in alignment with the maximum number of unoccupied states on the p-side. b) The dot indicates the operating point for the bias of part a).

As the forward bias is increased further, the occupied states on the n-doped side of the junction begin to come out of alignment with the unoccupied states on the p-doped side of the junction. As a result, past the tunnel current peak, the forward current diminishes with increasing forward bias, ideally going to zero when there are no longer any occupied states on the n-type side of the junction in alignment with unoccupied states on the p-type side of the junction. This region of decreasing current with increasing forward bias represents the negative differential region of operation of the tunnel junction and is the region of operation exploited in microwave oscillators. When a large enough bias is applied such that there are no longer any occupied states on the n-side aligned with unoccupied states on the p-side, the tunneling current goes to zero (Fig.3). Further increasing the forward bias places the junction in normal forward biased diode behavior.

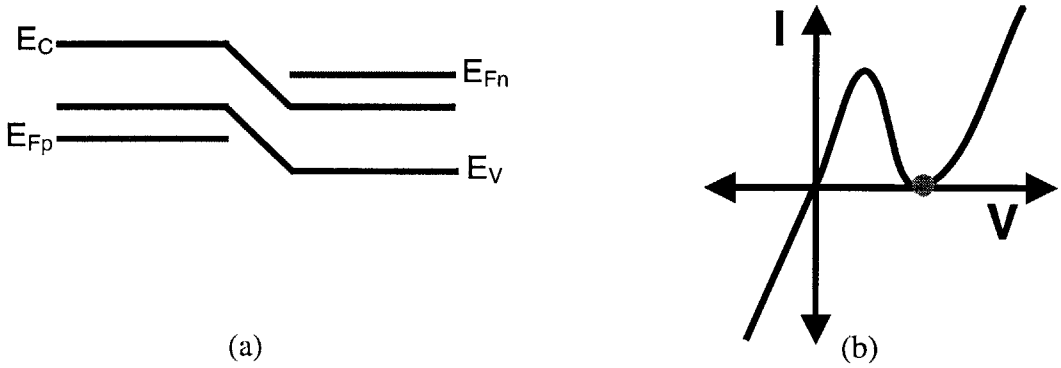

Figure 2-3. a) The tunnel junction bias at which the tunneling current no longer flows. b) The operating point for part a).

When a reverse bias is applied to the tunnel diode, the quasi-Fermi level on the p-doped side of the junction is raised with respect to the quasi-Fermi level on the n-doped side of the tunnel junction (Fig. 2-4). Now electrons on the p-doped side may tunnel to the unoccupied states on the n-doped side of the junction. The greater the reverse bias the larger the electric field in the junction becomes with an associated increase in the tunneling probability. The tunnel junction is employed in the bipolar cascade laser in the reverse bias regime.

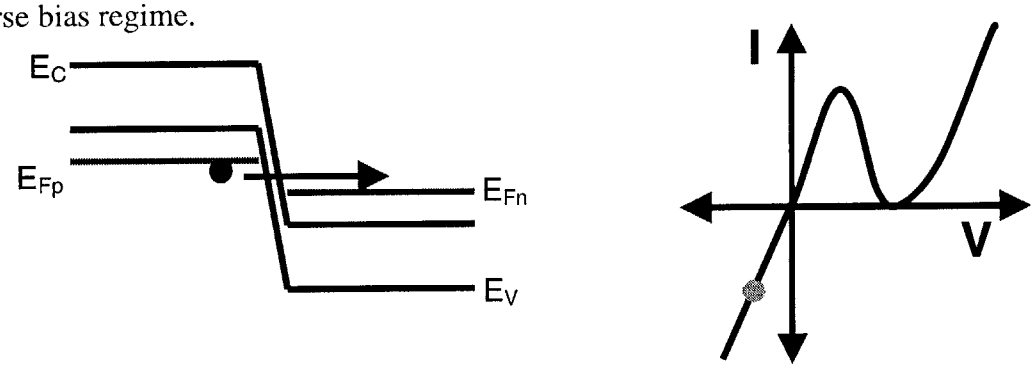

a) b)

Figure 2-4. a) The tunnel junction in reverse bias. b) The operating point for the bias of part a).

2.2 Tunnel junction modeling

The modeling of the junction will proceed along the lines of the work of E. O. Kane [3, 4, 5]. The key results needed for this section will be presented and motivated below, but the details of the derivations are relegated to Appendix A. The current-voltage (I-V) characteristics of the tunnel junction depend critically upon the tunneling probability of the electrons. Kane derived the following equation to describe the probability for the electron tunneling:

$$T = e^{\left(-\frac{\pi m^{*1/2} E_g^{3/2}}{2\sqrt{2} q E_{field} \hbar}\right)} e^{-\frac{E_\perp}{E}} \tag{2.1}$$

where m* is the effective mass, E_g is the energy gap of the material, q is the electron charge, E_{field} is the electric field, $E_\perp$ is the energy associated with the portion of the k-vector which is perpendicular to the junction normal and where:

$$\bar{E} = \frac{\sqrt{2}qE_{field}\hbar}{2\pi m^{*1/2}E_g^{1/2}} \tag{2.2}$$

Kane's result may be motivated by considering the standard form for the Wentzel-Kramers-Brillioun (WKB) tunneling approximation to be found in any text on quantum mechanics:

$$T \cong e^{-2\int_{x_1}^{x_2} dx\sqrt{\frac{2m^*}{\hbar}(E-U)}} \tag{2.3}$$

where T is the tunneling probability, E is the electron energy, U is the potential function through which the electron tunnels, and $x_{1,2}$ are the classical turning points.

The potential is taken to be of the form:

$$E_{\|} - U = -\frac{\left(E_g/2\right) - E_o^2}{E_g} - E_{\perp} \tag{2.4}$$

where $E_{\|}$ is the energy associated with momentum parallel to the junction normal, $E_{\perp}$ is the energy associated with momentum perpendicular to the junction normal, U the potential function in which the electron moves, E_g is the energy bandgap and E_o is given by qE_{field} x for a uniform field. Fig. 2-5 shows the form of this potential, with and without a momentum element perpendicular to the direction of transport. Fig. 2-6 illustrates that the effective bandgap (and effective barrier height) increases when $k_{\|}$ is non-zero. The classical turning points occur at those positions in space where $E_{\|}$ -U goes to zero. The inclusion of the perpendicular component of energy therefore modifies the classical turning points (Fig. 2-5). Substituting Eqn. 2.4 into Eqn. 2.3 and carrying out the integral leads directly to Eqn. 2.1.

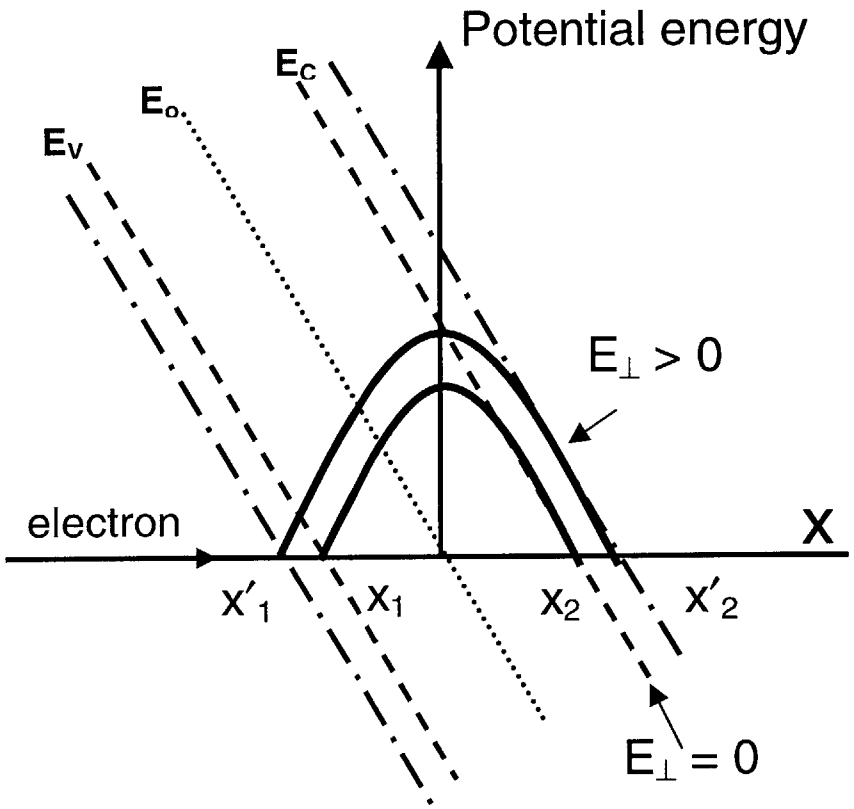

Figure 2-5. The tunneling potential used to calculate the tunneling probability. The tunneling potential is parabolic in shape reaching a maximum of $E_{gap}/4$ at x=0. The electric field is assumed to be uniform across the junction. Two band k·p theory and calculations using a weak periodic potential both yield potentials that are, or are near, parabolic. Two band k·p theory also substantiates the use of the WKB integral in calculating the tunneling probability. When there are components of crystal momentum perpendicular to the direction of tunneling the effective barrier height is increased. The potential width also increases moving the classical turning points from $x_{1,2}$ to $x'_{1,2}$.

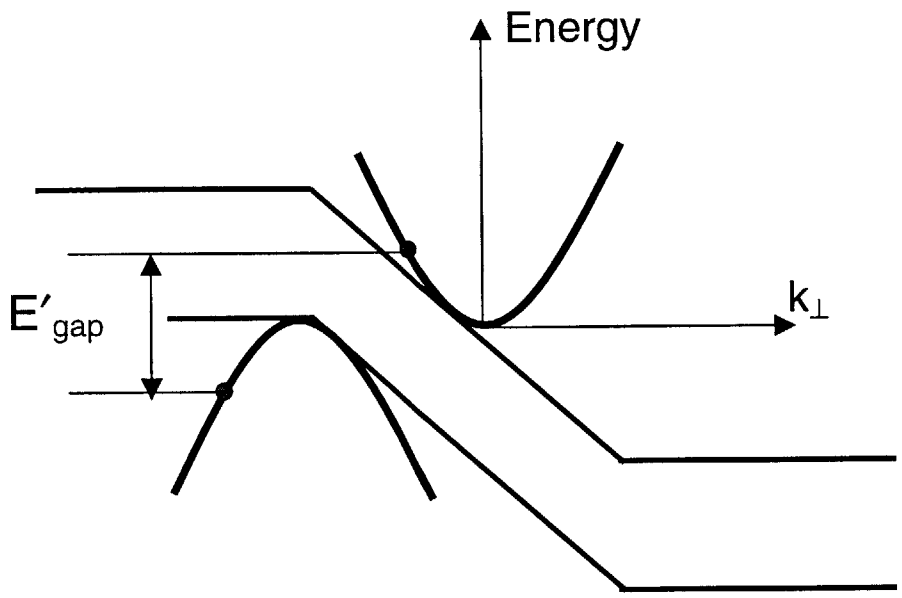

Figure 2-6. Components of momentum perpendicular to the direction of tunneling result in an increase in the effective bandgap energy for interband tunneling. This result is in contrast to intraband tunneling, wherein perpendicular components of momentum have no effect on the height of the tunneling potential.

The second exponential term on the right of Eqn. 2.1 accounts for the decrease in tunneling probability due to momentum components perpendicular to the direction of tunneling. Eqn. 2.2 may then be regarded as describing the meaningful range of allowable energies associated with momentum components perpendicular to the direction of tunneling which still possess a high probability of tunneling. While relatively simple in form, equation 2.1 bears further discussion. Inspection of Eqn. 2.1 reveals tunneling may be enhanced by using a material with a narrow band gap, with a small effective mass, and a large built-in electric field (or equivalently, a high active doping density). In the $In_xGa_{1-x}As$ system both the electron/hole effective masses and bandgap diminish with increasing In mole fraction. By using an x = 0.15 In mole fraction the bandgap energy drops from 1.42 eV in GaAs to 1.21 eV. The electron/hole mass drops from 0.063/0.5 m_o to 0.057/0.35 m_o, where m_o is the electron mass. Of course, if the quantum wells of the gain stages are 20% In mole fraction, then the In mole fraction of the tunnel junctions must be kept below this to prevent interband absorption in the tunnel junctions.

Although incorporating InGaAs as the tunneling material is a relatively straightforward endeavor, the benefits of the reduced bandgap energy and effective mass

won't be realized if suitably high doping densities are unobtainable. The n- and p-type doping densities of, and dopant properties in low mole fraction ($x < 0.20$) $In_xGa_{1-x}As$ have not been extensively studied as they have been in GaAs. InGaAs lattice matched to InP has been doped in excess of 10^{19} cm^{-3} for both n- and p-type dopants, however. It seems unlikely that achieving doping densities of this magnitude would present any great challenges for lower In mole fraction InGaAs. An alternative design possibility lies in using the narrower gap material to reduce the amount of doping necessary to achieve a given tunneling probability. The limitation to this technique occurs when the diminished critical thickness, resulting from the increasing In mole fraction, becomes thinner than the enlarged depletion layer width, resulting from the diminished doping levels.

A number of the assumptions made in deriving the tunneling probability deserve additional attention. In the derivation of Eqn. 2.1 it was assumed the electric field across the junction is uniform. While this is certainly true for p-i-n structures it is not true in general for abrupt junction p-n tunnel diodes. In a constant electric field junction the field is given precisely by $(V_{bi}-V_a)/W$, while in a p-n junction the *peak* field is given by $2\times(V_{bi}-V_a)/W$, where V_{bi} is the built-in junction voltage and V_a is the applied voltage. Hence it is clear that E_{field} may be replaced by one to two times the quantity $(V_{bi}-V_a)/W$ as was argued by Moll [6]. In this work a factor of two was used.

The effective mass to be used in Eqn. 2.1 is difficult to pin point. Since the electron tunnels from the conduction band to the valence band it is far from obvious if the conduction band effective mass should be used, the valence band effective mass, or some weighted average of the two. If the effective mass tensor is not isotropic the situation becomes even more complicated. In reality this question can only be rigorously answered through the use of k·p theory thereby making the effective mass in the forbidden region of the tunneling potential position dependent. This position dependent effective mass would then have to be taken inside the integral of the WKB approximation to determine the tunneling probability. Using two-band k·p theory the correct effective mass to be used is given by:

$$\frac{1}{m^*} = \frac{1}{m_c^*} + \frac{1}{m_v^*} \tag{2.5}$$

where m_c^* is the conduction band effective mass and m_v^* is the weighted (heavy and light hole) valence band heavy hole mass [7, 8].

An even more fundamental difficulty in calculating Eqn. 2.1 results when considering the functional form the tunneling potential should take. While the assumption may be to use a triangular potential, Kane [3, 5] used the equivalent of a parabolic potential of the form given in Eqn. 2.3. This potential is of the simplest form while still having the correct behavior at the band edges [5, 6]. It has been rigorously shown using two band k·p theory that the form of the tunneling potential is indeed near parabolic in form and the tunneling probability reduces to the WKB approximation [7]. The difference in the argument of the exponential in Eqn. 2.1 for a triangular potential versus a parabolic potential is only a matter of the value of the multiplicative constant. In fact, the same can be said of all the aforementioned difficulties. The form of the spatial dependence of the electric field, the effective mass, and the electron potential will only result in changes in the multiplicative factor in the exponential of Eqn. 2.1 and, hence, the constant can be viewed as a fitting parameter.

Using the tunneling probability the tunneling current versus applied voltage can then be calculated using [3,4]:

$$I = \int_{E_\perp} \int_{E_c}^{E_v} (f_c(E) - f_v(E)) \frac{qm^*}{2\pi^2\hbar^3} T dE dE_\perp \tag{2.4}$$

where $f_c(E)$ and $f_v(E)$ are the Fermi functions for the n- and p-type materials respectively. The limits of integration for the integral over E run from the top of the conduction band on the n-side of the junction (E_c is taken to be zero for convenience) to the bottom of the valence band on the p-side of the junction. The limits of integration for the perpendicular energy, $E_\perp$, require a little more consideration. Since $E_\perp$ can never exceed E, it is integrated from 0 to E if $E < E_v/2$, from 0 to $(E_v\text{-}E)$ if $E > E_v/2$. The effect of an applied

voltage is calculated by appropriately modifying the Fermi functions and the tunneling probability.

To ascertain the validity of the model, a calculation of the I-V characteristics using Eqns. 2.1-2.4 was compared to measurements made on a tunnel junction. The structure was grown on an n-type (~1-3×10^{18} cm^{-3}) GaAs wafer. After a 1 μm GaAs:Si buffer layer, 0.375 of GaAs:Si (nominally N_D = 1.6×10^{19} cm^{-3}) was grown followed by 0.25 of GaAs:Be (nominally N_A = 8×10^{18} cm^{-3}). No direct measurement was made of the doping densities in the tunnel junction. The assumed doping values were based upon measurements of Hall samples grown under the same conditions. After lithography and e-beam deposition of Ti (300 Å):Pt (200 Å):Au (3000 Å) an etch of NH_3OH:H_2O_2:H_2O (10:5:240) was done to form 0.75 μm tall posts. Measurements of the tunnel junction were done on an HP8545 semiconductor parameter analyzer. Measured values of the substrate (4.5 Ω) and contact resistance (5×10^{-4} Ω·cm^2) were subtracted from the measured tunnel junction I-V characteristics. Fig. 2-7 shows the measured (dashed line) and calculated (solid line) current density versus voltage. The solid line represents the calculated current using a parabolic tunneling potential (described above) while the dashed line represents the calculated tunneling current using a triangular potential. The tunneling probability through a triangular potential is over three orders of magnitude lower than through the parabolic potential. The agreement between the measurement and calculation is very good and lends validity to the model in predicting the I-V characteristics of tunnel junctions of various doping, bandgap and effective mass parameters. The inset to Fig.7 is a magnified view of the measured and calculated tunneling current in the forward bias regime. The agreement is reasonably good between theory and experiment but the measured current shows excess tunneling current (Section 2.3). The reader is cautioned, however, that a much more thorough study of measured tunneling I-V characteristics over a broader range of doping densities, and their agreement with theory, is in order.

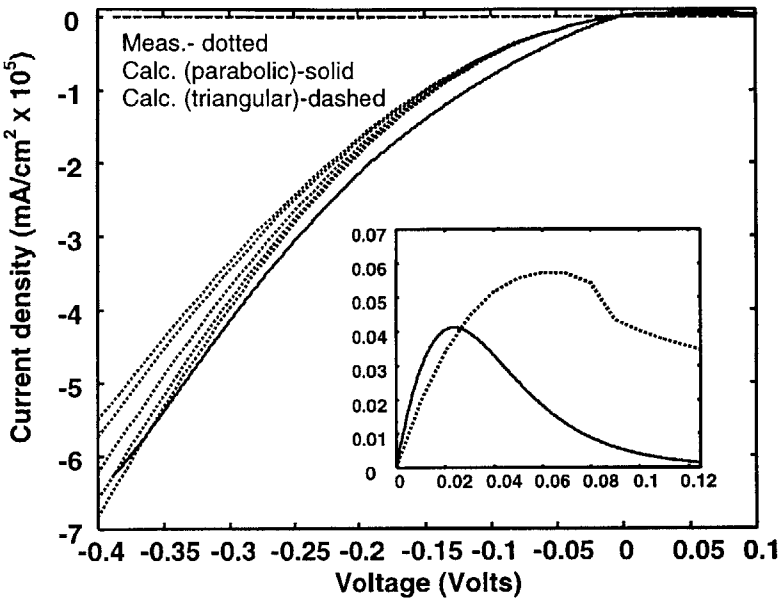

Figure 2-7. Measured (dotted lines), calculated using a parablic potential (solid line) and calculated using a triangular potential (dashed line) tunneling current density versus applied voltage. Note that the calculated tunneling current for the triangular potential is over three orders of magnitude smaller than for the parabolic potential. Inset is the measured and calculated forward bias characteristic of the junction.

Fig. 2-8 shows the tunneling current density versus voltage for a GaAs tunnel junction doped 2×10^{19} cm^{-3} on the n-side (which results in a degeneracy of E_F-E_C ~12kT at room temperature) over a range of acceptor densities on the p-side. An acceptor doping density of 6×10^{18} cm^{-3} is required to achieve degeneracy on the p-side as a result of the large density of states in the valence band of GaAs. If degeneracy is not achieved a reverse bias equal to the voltage difference between the Fermi level and the valence band edge must be applied before any tunneling commences. In the forward bias regime substantial tunneling current density and large negative differential resistance again occur only at high acceptor doping levels. If degeneracy isn't present on the p-type side of the junction then a vanishingly small number of unoccupied states are available for tunneling in forward bias with a resultant absence of forward tunneling current. Such a diode is known as a back diode. Similar but less pronounced trends result, due to the smaller conduction band density of states, from holding the p-doping constant while sweeping the donor concentration. Most importantly, with large doping values very little resistance

need drop across the tunnel junction to get sizeable currents. It can then be expected that the I-V characteristics of the entire BCL structure will be dominated by the voltage drops across the contacts, bulk regions and the laser diodes in the cascade. Fig. 2-9 is an enlargement of the forward I-V characteristics of Fig. 2-8. As stated above, the trend is for increased peak current at an increased voltage with increasing doping concentration. The greater degeneracy permits a greater applied voltage to reach the point where the maximum number of occupied states on the n-side aligns with the maximum number of unoccupied states on the p-side of the junction. The increased numbers of such states with increasing doping (degeneracy) leads to a larger peak current.

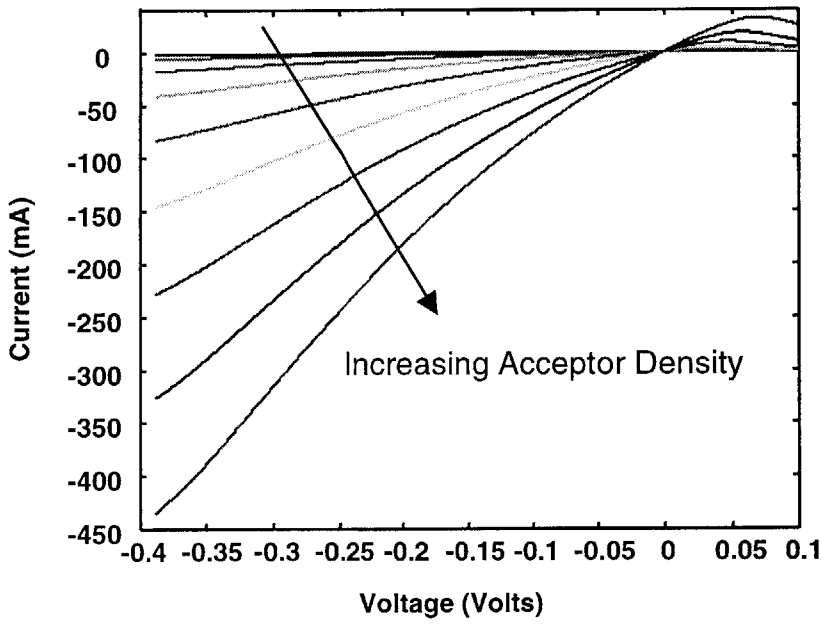

Figure 2-8. Tunneling current versus applied voltage for a 20 μm wide by 500 μm long device doped 2×10^{19} cm^{-3} on the n-side. The p-type doping values are 0.6, 0.8, 1.1, 1.5, 2.1, 2.9, 3.9, 5.4, 7.3, 10×10^{19} cm^{-3}. At high doping levels large currents flow for small applied voltages.

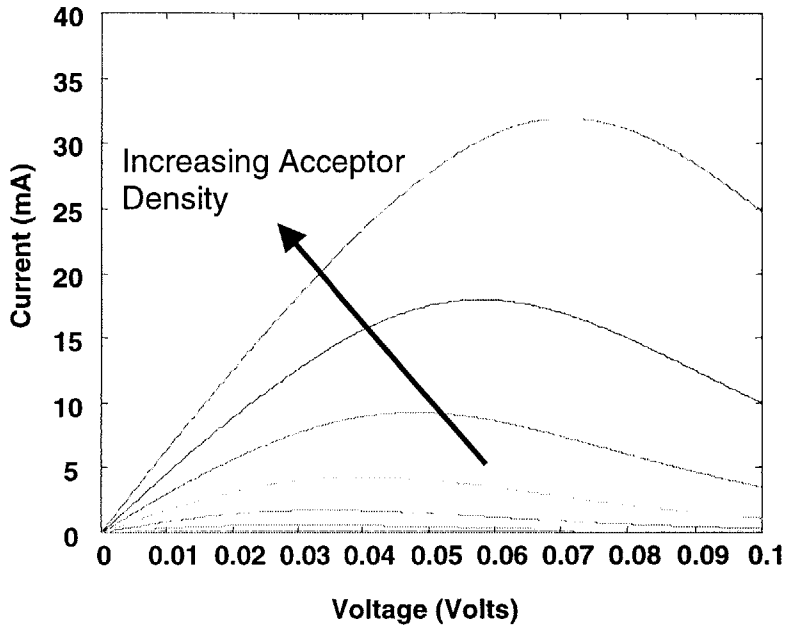

Figure 2-9. The forward tuneling currents of Fig. 2-8. The peak current increases, as does the voltage at which the peak current occurs, with increasing doping densities.

As is evident in Fig. 2-8, doping well in excess of degeneracy is required to achieve any appreciable reverse tunnel current. The substantial bandgap of GaAs (1.42 eV at room temperature) requires a sizable built-in electric field (2×10^6 V/cm) to achieve a high tunneling probability. The exponential nature of the I-V curve in reverse bias is evident. This nonlinearity can result in signal distortion in the output of a modulated BCL. While the nonlinear nature of the reverse bias I-V characteristics cannot be completely eliminated, the deleterious effects can be minimized by reducing the resistance of the tunnel junction below that of any other in the BCL.

The most substantial gains in tunnel junction conductivity are realized by using $In_xGa_{1-x}As$ as the tunneling material. Fig. 2-10 shows the I-V curves of x = 0, 0.05, 0.10, 0.15 InGaAs junctions doped on both sides to 2×10^{19} cm^{-3}. A 15% In mole fraction junction performs comparably to a GaAs junction doped twice as heavily. As expected, at a given doping density the incorporation of any amount of In into the tunnel junction improves the conductivity of the junction over a GaAs junction.

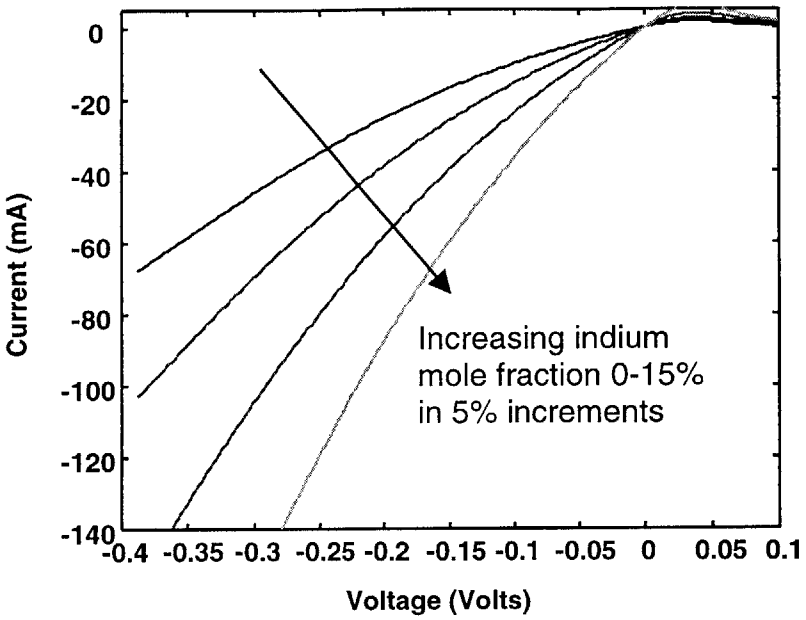

Figure 2-10. The tunneling current versus voltage for 20 μm by 500 μm device with In mole fractions varying from 0-15% in 5% increments. The doping densities are 2×10^{19} cm^{-3} on both the n- and p-sides of the junction. Increasing the In mole fraction reduces the bandgap and effective mass leading to improved tunneling characteristics.

From a circuit theoretical point of view, what is of greatest interest are the large signal and differential resistances of the tunnel diodes. Fig. 2-11 shows the large signal resistance versus doping density over a range of bias points of a tunnel diode. At low doping densities, the resistance shows a rather substantial dependence upon bias point while at higher densities the junction resistance is relatively insensitive to bias. The same holds true for the differential resistance (Fig. 2-12). Holding the doping densities constant at 2×10^{19} cm^{-3} but switching to 15% In mole fraction InGaAs from GaAs yields substantial improvement in both large signal and differential resistance (Fig.'s 12a and 12b). The advantage gained in using narrow bandgap semiconductors is diminished when very high doping densities are used. This is important in BCL structures which may contain many cascades as the accumulated strain of several In containing junctions could exceed the limit for pseudomorphic growth.

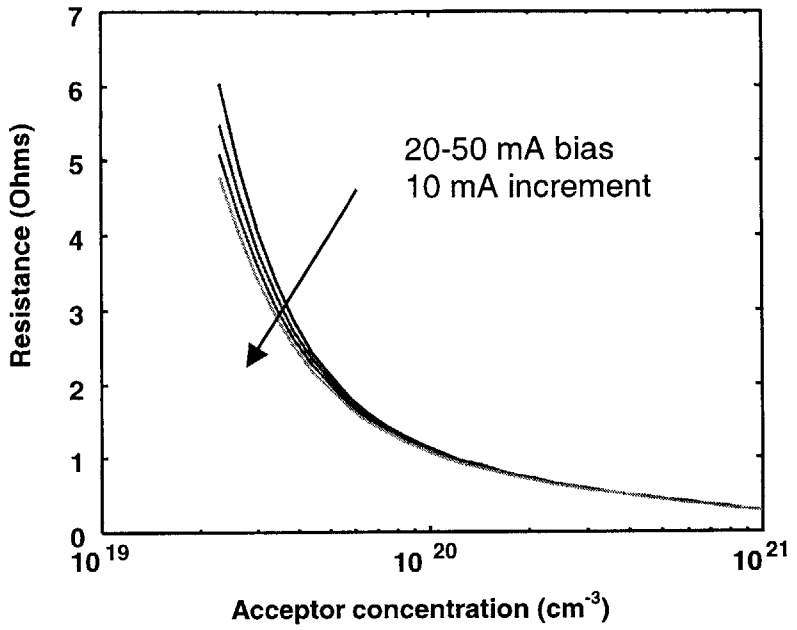

Figure 2-11. The junction resistance versus p-type doping density of a 20 μm by 500 μm tunnel junction doped to 2×10^{19} cm^{-3} on the n-side of the junction over a bias range of 20-50 mA. At lower doping densities the device resistance is sensitive to bias point while at densities in excess of 1×10^{20} cm^{-3} the bias point sensitivity is negligibly small.

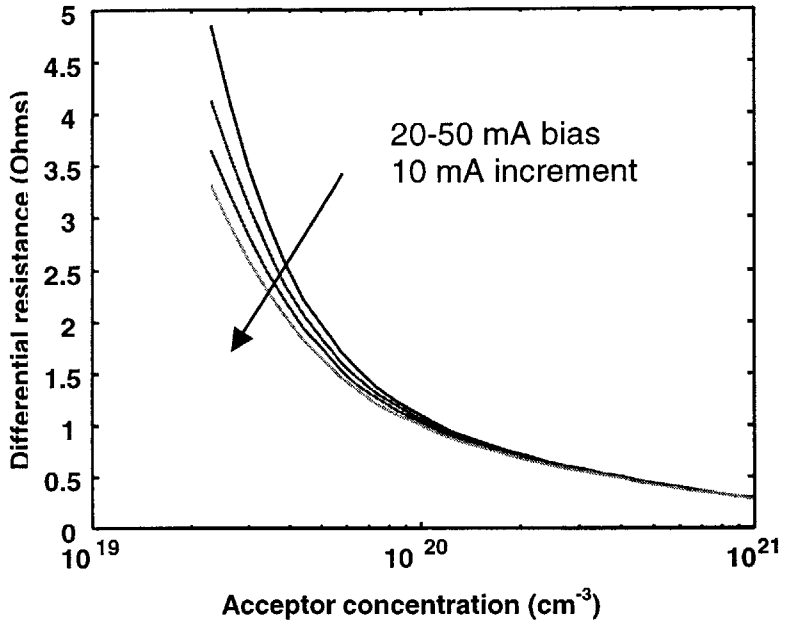

Figure 2-12. The differential resistance for the device of Fig. 2-11. The same trends that were evident in the resistance also appear in the differential resistance.

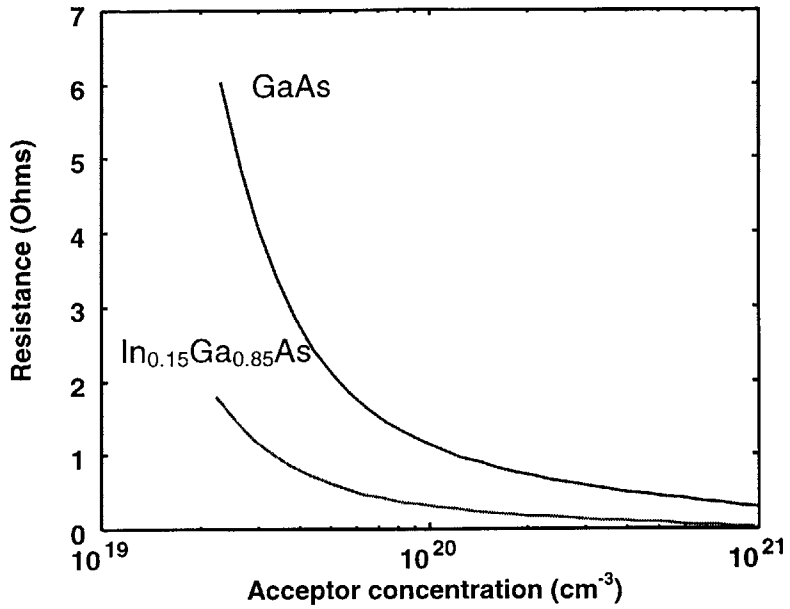

Figure 2-13. The resistance of a 20 μm by 500 μm tunnel junction versus acceptor concentration doped 2×10^{19} on the n-side of the junction for GaAs and $In_{0.15}Ga_{0.85}As$ devices. The device is biased at 20 mA. The $In_{0.15}Ga_{0.85}As$ device is considerably less resistive than the GaAs device at lower doping densities. At higher densities the advantage is less pronounced.

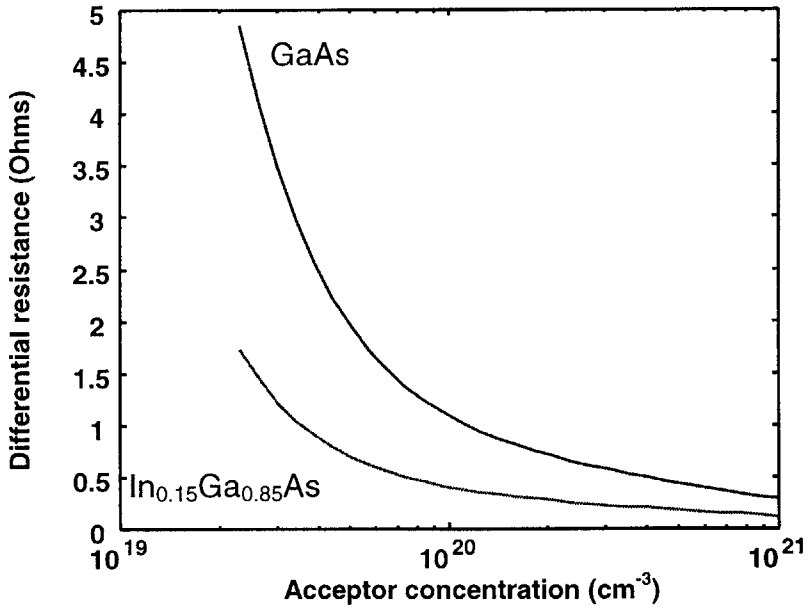

Figure 2-14. The differential resistance versus acceptor concentration for the device of Fig. 2-13. The same trends which were evident for the resistance are also present for the differential resistance.

The bandgap of GaAs and the Fermi functions in the current integral of Eqn. 2.4 are temperature dependent functions. It is then worthwhile to determine the effect temperature fluctuations have on the current-voltage behavior of the tunnel diode. As demonstrated in Fig. 2-15, at least in the temperature range of 300-380 K, the tunnel junction behaves relatively independent of temperature.

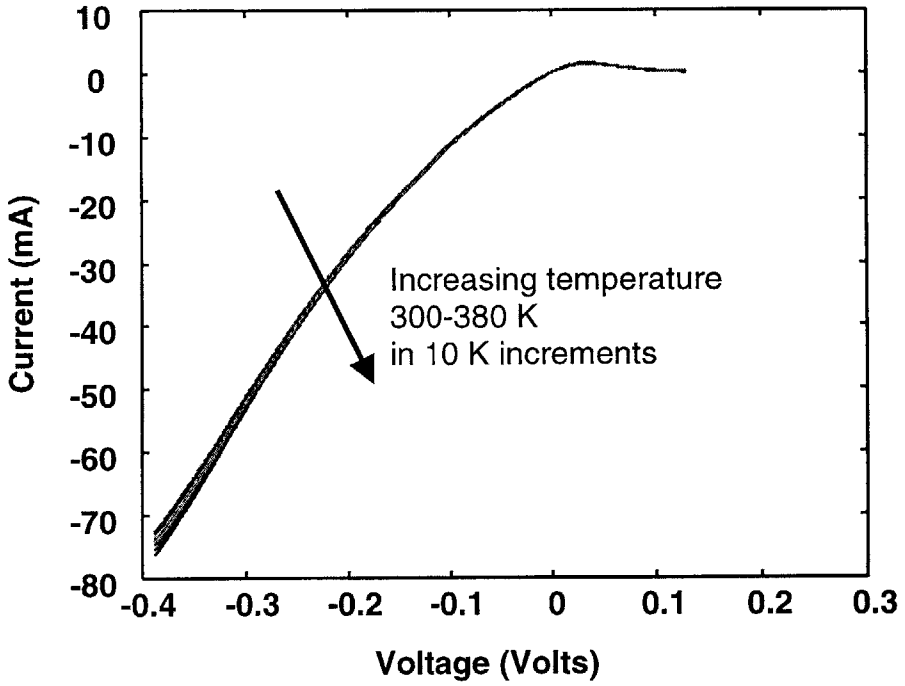

Figure 2-15. The current versus applied voltage for a tunnel junction doped on both sides to 2×10^{19} cm^{-3} for a 20 μm by 500 μm device. The tunneling current characteristics exhibit little sensitivity to temperature over the range 300-380 K.

2.3 Materials Considerations for Semiconductor Tunnel Junctions

As was discussed in Section 2.2, to make a high quality tunnel junction it is desirable to use the most narrow bandgap material consistent with lattice-matching considerations and as large a built-in electric field as possible. The latter requirement is met by heavily doping the junction. It is also necessary to make the junction abrupt as intermixing of the n- and p-type dopants reduces the effective doping. The materials growth demands and limitations in achieving these ends are detailed in this section.

It was decided to make the first BCL designs in the InGaAsP material system on GaAs substrates. This decision was reached based upon the consideration of a variety of

factors. The $In_{0.2}Ga_{0.8}As$/GaAs quantum wells used for the production of 980 nm laser light have large gain, excellent differential quantum efficiency and are robust. Longer wavelength devices also suffer from increased threshold current densities induced by Auger recombination. While the threshold current through a N-gain stage BCL is independent of N, the voltage drop across the device goes as $N \times V_{diode}$ as each gain stage must be biased to "flat band". The multiple voltage drops across a cascade laser make power dissipation a concern and increased bias currents represent an unnecessary complication when studying this new type of device. Finally, the growth facility available was much more thoroughly calibrated in the InGaAsP on GaAs material system than any other system. Therefore, the following discussion concerning materials factors with respect to tunnel junctions will focus upon the InGaAsP material system on GaAs substrates.

The limit for the smallest achievable bandgap on a given host lattice is set by two constraints. Lattice mismatch considerations or, more precisely, the critical thickness achievable for a given amount of strain in a semiconductor epilayer sets an upper bound on the mole fraction of In in an InGaAs layer grown upon a GaAs substrate. Increasing the In content reduces the bandgap but greatly increases the strain. The layers of the tunnel junction must be at least as wide as the depletion layer width of the p-n junction. Under actual growth conditions it is wise to make the tunnel diode much wider. Assuming reasonable doping concentrations (on the order of 10^{19} cm^{-3}), the bandgap of the InGaAs layer will fall below that of the quantum well before the limit set by strain and critical layer thickness is reached.

The material for the tunnel junctions and first generation BCL were grown using gas-source molecular beam epitaxy (GSMBE). Molecular beam epitaxy (MBE) is a method of growing epitaxial layers by making atomic or molecular beams containing the necessary constituent elements incident upon a heated single crystal substrate. The growth is carried out in a high vacuum chamber ($\sim 10^{-10}$ Torr) such that the mean free path of an atom or molecule in the molecular beam is much greater than the distance from the source to the substrate. Most sources in the MBE are elemental and solid in form at room temperature. They are contained in shuttered containers known as Knudsen cells. The source materials are heated via resistive coils wrapped around the Knudsen cells.

The beam from a cell is made incident upon the substrate by opening the shutter over the cell, while the flux is controlled via the Knudsen cell temperature. In GSMBE the arsine and phosphorous sources come from arsine (AsH_3) and phosphine (PH_3). The gas is run over a heated filament at ~900 ^oC, a process is known as "cracking". The cracked form consists of As_2 (P_2) and H_x by-products with some residual As_4 (P_4).

For the initial experiments, GaAs was chosen as the material for the tunnel junction, although $In_{0.1}Ga_{0.9}As$ would have been a more appropriate choice based upon the latter mentioned considerations. The Knudsen cell stability necessary to grow reproducible ternaries needed to properly perform the doping studies was questionable. More importantly, the properties of dopants have not been as extensively studied in $In_{0.1}Ga_{0.9}As$ as they have been in GaAs, an issue that will be shown to be of critical importance in Chapter 3. GaAs makes a suitable, albeit not ideal, candidate for the tunnel junction material.

Studies have been done to determine maximum dopant incorporation in the $Al_xGa_{1-x}As$ system [9-19]. The values arrived at depend critically upon the growth conditions, the particular dopant species, and the growth technology employed. The gas-source molecular beam epitaxy machine in which the heterostructure for the first BCL was grown had beryllium (Be) available as the p-type dopant and silicon (Si) as the n-type dopant. Studies have indicated that carbon (C) produces higher doping densities than does beryllium [19], but carbon was not available for use. Beryllium incorporation has been shown to be limited by the thermally activated diffusivity of Be [14, 17]. In a study by Schubert et al. [17], the thermally dependent diffusion coefficient for Be at a density of 10^{18} cm^{-3} was determined to be:

$$D = D_o e^{-\left(\frac{E_A}{kT}\right)} = 2\times10^{-5}\left(\frac{cm^2}{s}\right)e^{-\frac{1.95(eV)}{kT}} \tag{2.5}$$

where D is the diffusion coefficient, E_A is the activation energy, k is Boltzmann's constant and T is temperature. By way of comparison, carbon, which has been shown to have a maximum active dopant incorporation of 1.5×10^{21} in GaAs has an activation

energy of 1.75 eV but a D_o of only 5×10^{-8} cm^2/s. Be has only shown to have a peak free carrier concentration of 2×10^{20} in GaAs [20].

It can then be expected that, to a point, lower substrate temperatures should lead to increased Be incorporation. While very low temperatures (< 400 °C) may not yield higher dopant incorporation, too low of a temperature leads to non-stoichiometric growth of the GaAs as well as Be precipitation. In the case of Si, the maximum doping density is set by the propensity of Si to become amphoteric above a critical doping density set by growth conditions.

To determine the best substrate temperature to maximize dopant incorporation (and activation) in GaAs for the GSMBE system used in this work, a study was conducted to establish carrier density versus substrate temperature. The results are shown in Fig. 2-16. Aside from the substrate temperature, the Be flux (as controlled by the Be Knudson cell temperature) parameter space was also investigated. The values reported in Figure 2-16 represent the peak values obtainable for the given substrate temperature. Maximum Be incorporation was found at a substrate temperature of 480 °C and a Be cell temperature of 755 °C. Higher Be flux did not produce larger measured values of free carrier density. It is possible this effect results from incorporation saturation or from incorporated dopants that fail to activate. The doping densities were determined through Hall measurement of the samples. There was no indication of the surface roughening that has been seen in highly Be-doped GaAs [10]. Good morphology is of critical importance as surface roughening would compromise the quality of any epitaxial layers grown over the tunnel junction. The peak value of 2×10^{19} is an order of magnitude lower than the value reported in [20]. It is conceivable that an even more thorough examination of the parameter space could yield p-doping densities closer to those realized in [20]. Nevertheless, disparate results are found in the literature for all manner of material parameters. Such is the case not only for material being grown using different growth technologies but also in different machines using the same growth technologies. It is therefore also possible that a Be doping density of 2×10^{19} is the maximum achievable for the GSMBE system used in this study. Regardless, this density produces a built-in electric field large enough to permit tunneling.

The same study was performed for Si doping of GaAs (Fig. 2-16). Again 480 °C was found to be the substrate temperature at which the dopant incorporation was maximum for this study. The Si doping density continued to increase with increasing Si Knudson cell temperature. A density of 1.6×10^{19} was achieved at a cell temperature of 1150 °C. Further increases in the cell temperature were not pursued due to concerns about the survivabilty of the cell at more elevated temperatures. The Si doping density achieved is slightly in excess of the highest reported in the literature using MBE and an As_2 source[20]. While diffusion is the proposed mechanism for limiting the maximum Be incorporation for GaAs, the proposed mechanism for Si is the amphoteric nature of Si in III-V semiconductors [19, 21]. At low doping levels ($\approx10^{18}$ cm^{-3}) Si will typically occupy a group III lattice site in a III-V semiconductor where it serves as a donor. As the doping incorporation continues to increase the Si may begin to occupy group V sites where it acts as an acceptor. At very high doping levels the Si is as likely to occupy a group V site as a group III site. This process is known as self-compensation. A dopant which can serve either as a donor or acceptor in a particular lattice is known as being amphoteric. It is unlikely that even higher densities would be achievable as the Si doping density achieved is around the value at which Si begins to become amphoteric in GaAs [19, 21].

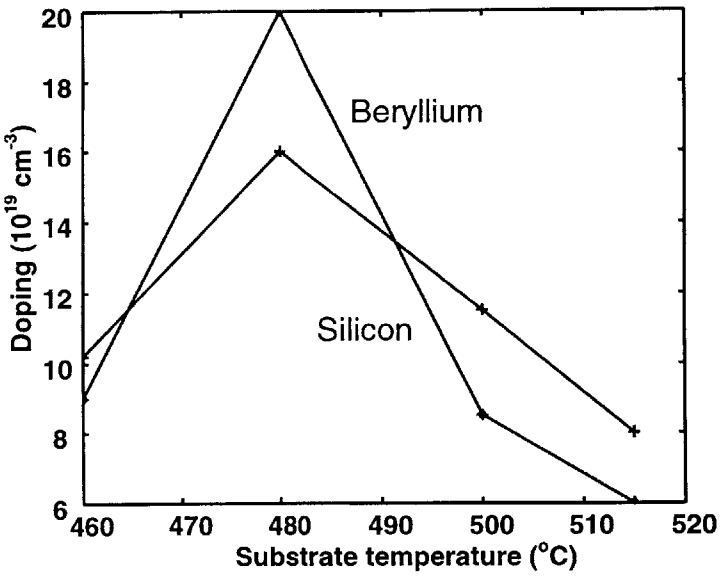

Figure 2-16. Peak achieved doping densities versus substrate temperature for Si and Be in GaAs.

Various growth modes are possible in MBE. When growing a binary system such as GaAs, if one of the constituent groups is in shorter supply than the other group on the growth surface then the growth is said to be limited by the underrepresented group. In all the doping studies conducted for this thesis the arsenic overpressure was sufficiently high to ensure the growth was group III limited. The measured chamber arsenic pressure was $1.6\text{-}1.9\times10^{-5}$ Torr. No discernible difference in material quality was evident over the given range of arsenic overpressures. Previous investigations of the growth of GaAs down to substrate temperatures of 400 °C had indicated this overpressure to produce GaAs of high electrical quality [22]. It has been shown that As_2 produces more highly doped layers with superior morphology than As_4 [11, 20].

The doping and diode studies outlined above and in Section 2.2 lead to the final design and growth parameters that were used in the tunnel junction employed in the first generation BCL. The tunnel junction nominally consists of 25 nm each of GaAs:Si^{++} (1.6×10^{19}) and GaAs:Be^{++} (2×10^{19}). The depletion layer width for these doping levels is ~15 nm, considerably less than either layer in the junction. The junction was made considerably wider than what the depletion layer width would indicate is necessary as some uncertainty concerning the doping densities existed at the time the BCL structure was grown. Prior to the secondary ion mass spectroscopy (SIMS) analysis of the tunnel junction described in the next paragraph the only available determinant of doping densities was Hall measurement. While the SIMS eventually verified the Hall effect measurements after the growth of the BCL, the Hall effect can give substantial errors and the junction was made wide enough to account for any such error in doping. Additionally, some uncertainty exists in growth rate calibration, especially for thin layers, and it is preferable to have a wider junction than expected than one that is too narrow to accommodate the depletion layer. The doping levels are approximately equal for the n- and p-type material and hence the depletion layer is approximately equal on each side of the metallurgical junction.

As will be explained fully in Chapter 3, it became necessary after the tunnel junction was grown to conduct a ~30 minute excursion to a substrate temperature of 515 °C while growing the topmost gain stage of the BCL. Considering the previously detailed thermally activated diffusivity of Be, a secondary ion mass spectroscopy (SIMS)

study was performed to determine any deleterious effect the elevated temperature might have had on the tunnel junction. Fig. 2-17 shows the results of the SIMS measurement. The tunnel junction stayed intact even after the ~30 minutes at 515 °C. The SIMS has a spatial resolution of 5 nm and a target species resolution of ± 10%. Particularly encouraging was the excellent agreement between the SIMS study and the Hall measurements.

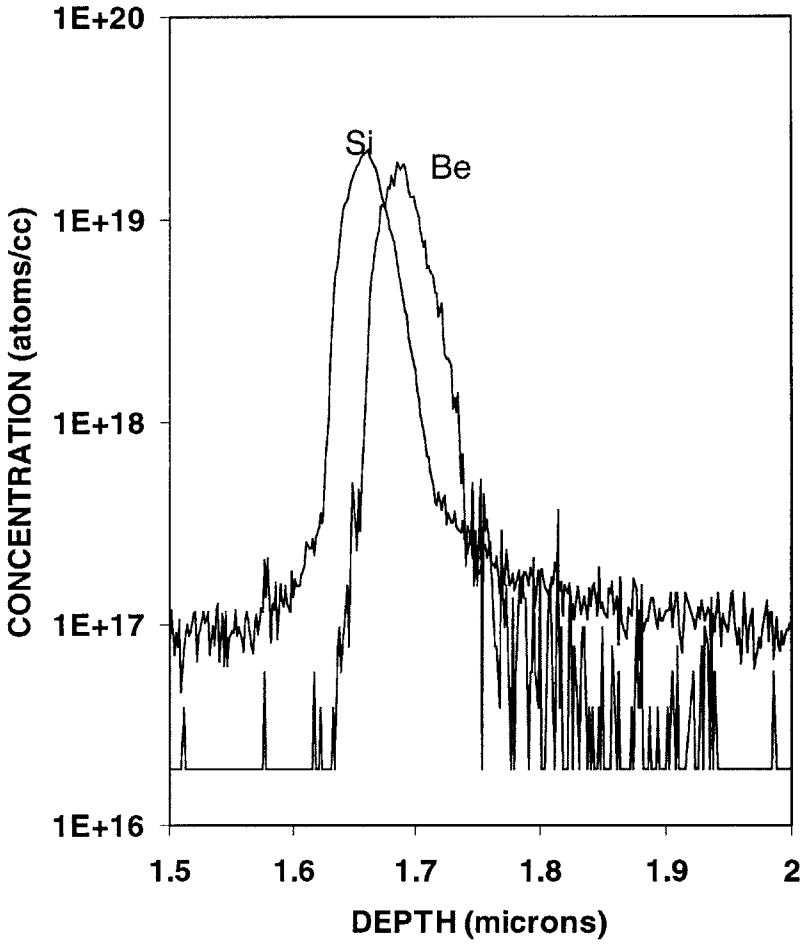

Figure 2-17. Secondary ion mass spectroscopy measurement of a GaAs tunnel junction embedded in a two stage bipolar cascade laser. The tunnel junction underwent a 30 minute excursion to a substrate temperature of 480 °C. The junction remained intact with doping densities remaining on the order of 2×10^{19} cm^{-3} on both sides of the junction.

The SIMS analysis also revealed the intermediate temperature growth of the GaAs tunnel junction resulted in oxygen incorporation on the order of ~10^{18} cm^{-3}. Oxygen serves as a deep state in GaAs and it is known to readily incorporate at lower

growth temperatures. GaAs is normally grown at substrate temperatures of 600-640 °C as deep level impurity incorporation diminishes the conductivity of the epitaxy. Additionally, in undoped GaAs and at $Al_xGa_{1-x}As$/GaAs interfaces, such as those used in the waveguides of quantum well lasers, these deep states act as nonradiative traps and have a catastrophic effect on optical device performance.

In the case of the tunnel junction, the presence of intermediate states in the bandgap most likely leads to deep state assisted tunneling [23, 24]. The calculated value of the tunnel junction contact resistance was $1\text{-}3\times10^{-4}$ $\Omega\cdot cm^2$. The measured value was found to be $6\text{-}8\times10^{-5}$ $\Omega\cdot cm^2$. This dramatic improvement is attributed to the presence of deep states and yields a tunnel junction whose performance is far superior to that which might be expected from the measured incorporated dopant densities. Deep states assist tunneling by providing intermediate states into which the electron may tunnel as it progresses from one side of the junction to the other (Fig. 2-18). In the forward bis regime, one possible path for an electron is to drop into a deep state in the forbidden region then tunnel into the valence band on the p-side of the junction. The tunneling current then never goes to zero in forward bias as shown in Fig. 2-19. Rather there is an "excess" tunneling current before the diode moves into the normal forward biased p-n junction range of operation (Fig. 2-19). In reverse bias the deep levels provide an intermediate state into which the electron can tunnel before tunneling through the remainder of the barrier. The intermediate states increase the probability that tunneling will occur by effectively reducing the barrier width through which the tunneling occurs and therefore reduce the "resistance" of the junction. Some modeling of this effect has been performed in [23, 24] but it is of a very ad hoc nature with multiple fitting parameters. While qualitative trends may be highlighted using such methods the quantitative agreement can be quite poor.

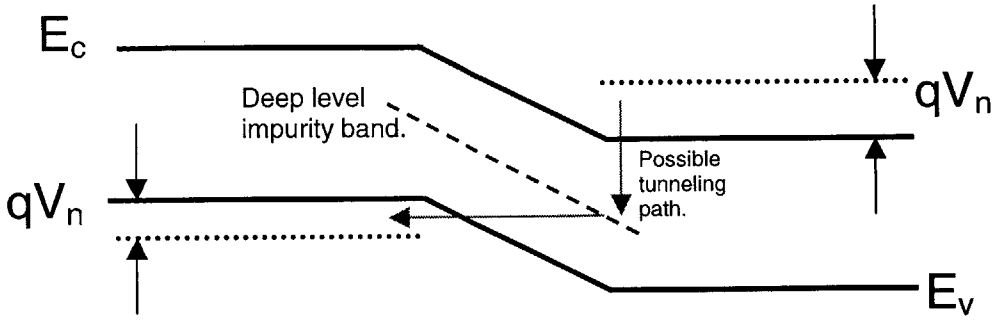

Figure 2-18. A tunnel junction containing a large density of deep level impurities. Shown is one of many possible paths for an electron. The electron is captured by the deep state, then tunnels through the resultant potential barrier. As a result of the deep states, the tunneling current never goes to zero as would be expected in an ideal tunnel junction.

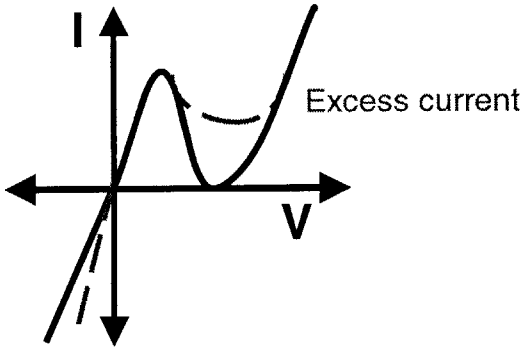

Figure 2-19. The effect of the deep level states upon the current versus voltage characteristics of the ideal tunnel junction. Dashed lines show the effect of the deep states on the I_V characteristics of the tunnel junction.

2.4 Band structure of the bipolar cascade laser

It is illustrative to consider the form of the band structure for a bipolar cascade laser at equilibrium and under bias. Fig. 2-20a shows the equilibrium band diagram for a two gain stage BCL with $Al_{0.4}Ga_{0.6}As$ cladding regions, doped to 5×10^{17} on both the n- and p-sides with a 0.22 μm wide GaAs separate confinement heterostructure (waveguide)

region. The cladding regions as shown are an unrealistically narrow 0.2 μm to allow a clearer view of the tunnel junction. The n-side of the GaAs tunnel junction is doped to 1.5×10^{19} cm^{-3} and the p-side is doped to 4.3×10^{19} cm^{-3}. The quantum wells are not shown in the figure.

The depletion approximation was used at the doped-$Al_{0.4}Ga_{0.6}As$ cladding to intrinsic GaAs heterojunctions. The voltage drop across the intrinsic region and the width of the depletion regions were calculated by requiring displacement field continuity across the cladding to intrinsic heterojunction. The doped-cladding to highly doped GaAs hetero-interface was treated as a metal-semiconductor junction due to the high degree of degeneracy in the GaAs. In the case of the doping values used for this example, no built-in potential existed at the highly doped GaAs-cladding heterojunction. The conduction band discontinuity between the $Al_{0.4}Ga_{0.6}As$ cladding and the GaAs regions was taken as 67% of the bandgap energy difference between the two materials.

From basic energy conservation considerations, a voltage equal to at least the n=1 transition voltage in the active region must be applied to a laser to achieve threshold. The BCL's minimum threshold voltage can then be estimated by multiplying the number of gain stages times the single stage threshold voltage and then adding the voltage drop across the tunnel junction(s) at the threshold current. If the tunnel junction has a very small resistance then its contribution to the BCL's threshold voltage is small with respect to the active region threshold voltages. In practice, there are also parasitic resistances from the contacts and bulk regions of the device. Fig. 2-20b shows the BCL of Fig. 2-20a biased to the edge of lasing, assuming no parasitic resistances. Note the tunnel junction width barely changes as the built-in voltage is approximately 1.8 V while the voltage drop across the junction near threshold is less than 0.1 V.

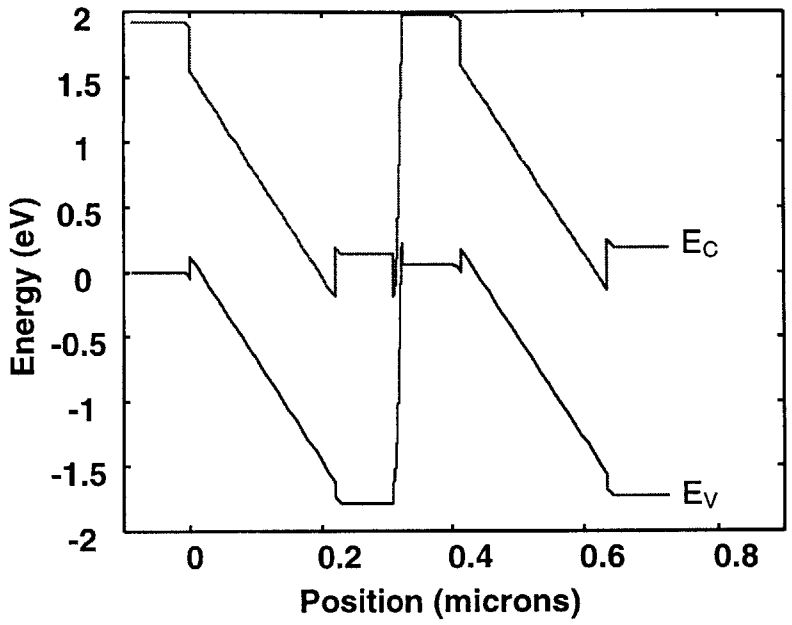

(a)

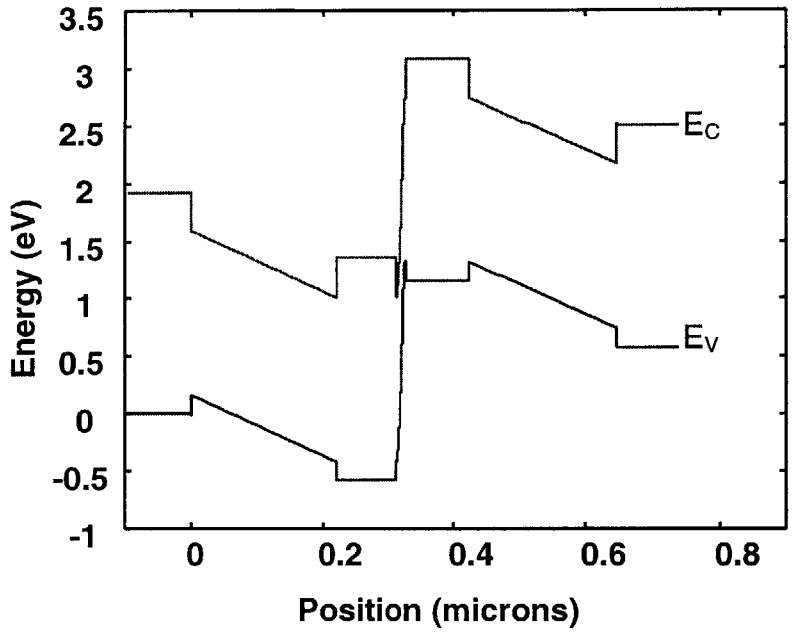

(b)

Figure 2-20. a) Bipolar cascade laser at equilibrium. The cladding layers are $Al_{0.4}Ga_{0.6}As$ doped 5×10^{17} on both sides with an intrinsic 0.22 μm GaAs waveguide (the QWS are not shown). The cladding layers are only 0.2 μm for clarity. b) The bipolar cascade laser biased nearly to threshold, $V_{applied}$=2.5 V.

2.5 Summary and conclusions

The theoretical study of the tunnel process illuminated several key features in obtaining low resistance tunnel diodes. The use of small bandgap and effective mass materials was indicated and the need for obtaining and maintaining large doping concentrations was highlighted. An experimental study of a tunnel diode structure in GaAs indicated good agreement with experiment. Large silicon (1.6×10^{19} cm^{-3}) and beryllium (2.0×10^{19} cm^{-3}) incorporation was found in GaAs at a substrate temperature of 480 °C using gas-source molecular beam epitaxy. A secondary ion mass study verified free carrier values determined by Hall effect measurements even after a thirty minute excursion of the substrate temperature to 515 °C.

The use of beryllium as the p-type dopant, known to exhibit a high degree of thermally activated diffusivity, places limitations on the substrate temperatures that may be used for any epitaxial layers grown subsequently to the tunnel diode. The gain stages and waveguides must stay within these thermal bounds while retaining excellent optical and electrical qualities. The materials and design challenges that must be met to achieve this end are the topic of Chapter 3.

References:

[1] L. Esaki, "Long journey into tunneling", Proc. of the IEEE, vol. 62, no. 6, 825-831, 1974.

[2] K. K. Thornber, T. C. McGill and C.A. Mead, "The tunneling time of an electron", Journ. Appl. Phys., vol. 38, no. 5. 2384-2385, 1967.

[3] E.O. Kane, "Theory of tunneling", J. Appl. Phys., vol. 32, no. 1, 83-91, 1960.

[4] E.O. Kane, "Zener tunneling in semiconductors", J. Phys. Chem. Solids, vol. 12, 181-188, 1959.

[5] S. M. Sze, "Physics of semiconductor devices", John Wiley and Sons, Inc. New York, 1981.

[6] J. L. Moll, "Physics of semiconductors", McGraw-Hill, New York, 1964.

[7] F. Rana, "Electron tunneling processes in Si/SiO_2 systems", Master's Thesis, MIT, 1997.

[8] J. N. Schulman, "Extension of Tsu-Esaki model for effective mass effect in resonant tunneling", Appl. Phys. Lett., vol, 72, no. 22, 2829-2831, 1998.

[9] S. Fujita, S. M. Bedair, M. A. Littlejohn, and J. R. Hauser, "Doping characteristics and electrical properties of Be-doped p-type $Al_xGa_{1-x}As$ by liquid phase epitaxy", J. Appl. Phys., vol. 51, no. 10, 5438-5444, 1980.

[10] Y. Iimura and M. Kawabe, "Be doping effect on growth kinetics of GaAs grown by MBE", vol. 25, no. 1, L81-L84, 1986.

[11] Y. C. Pao and J. Franklin, "Influence of As_4/Ga flux ratio on Be incorporation in heavily doped GaAs grown by molecular beam epitaxy", vol. 95, 301-304, 1989.

[12] A. Gaymann, M. Maier, W. Bronner, N. Grün, and K. Kohler, "Beryllium diffusion in short-period $Al_xGa_{1-x}As$/AlAs-superlattices and vertically compact laser structures grown by molecular beam epitaxy", Mat. Sci. and Eng. B, vol. B44, 12-15, 1997.

[13] R. L. S. Devine, C. T. Foxon, B. A. Joyce, J. B. Clegg, and J. P. Gowers, "Beryllium diffusion across GaAs/(Al, Ga)As heterojunctions and GaAs/AlAs superlattices during MBE growth", Appl. Phys. A, vol. 44, 195-200, 1987.

[14] E. F. Schubert, G. H. Gilmer, R. F. Kopf, and H. S. Luftman, "Maximum incorporation of impurities in semiconductors", Phys. Rev. B, vol. 46, no. 23, 78-84, 1992.

[15] R. F. Kopf, E. F. Schubert, S. W. Downey, and A. B. Emerson, "N- and p-type dopant profiles in distributed Bragg reflector structures and their effect on resistance", Appl. Phys. Lett., vol. 61, no. 15, 1820-1822, 1992.

[16] M. Kongai, T. Yamada, T. Akatsuka, K. Saito, E. Tokumitsu, K. Takahashi, "Metallic p-type GaAs and GaAlAs grown by metalorganic molecular beam epitaxy", Journ. of Crys. Growth, vol. 98, no. 1-2, 167-173, 1989.

[17] E. F. Schubert, J. M. Kuo, R. F. Kopf, H. S. Luftman, L. C. Hopkins, and N. J. Sauer, "Beryllium δ doping of GaAs grown by molecular beam epitaxy", Journ. of Appl. Phys., vol. 67, no. 4, 1969-1979, 1990.

[18] J. L. Lievin, F. Alexandre, C. Dubon-Chevallier, in "Properties of impurity states in superlattice semiconductors", C. Y. Fong, I. P. Batra, and S. Ciraci, eds., Plenum, New York, 1988.

[19] E. F. Schubert, "Doping in III-V semiconductors", University Press, Cambridge, 1993.
[20] R. J. Malik, J. Nagle, M. Micovic, T. Harris, R. W. Ryan, and L. C. Hopkins, "Doping limits of C, Be, and Si in GaAs grown by solid source molecular-beam epitaxy with a thermally cracked As_2 source", J. Vac. Sci. Technol. B, vol. 10, no. 2, 850-853, 1992.
[21] M. Ogawa, T. Baba, "Heavily Si-doped GaAs and AlAs-GaAs superlattice grown by molecular beam epitaxy", Japan. Journ. of Appl. Phys. Part 2, vol. 24, no. 8, L572-574, 1985.
[22] J. F. Ahadian, P. T. Vaidyanathan, S. G. Patterson, Y. Royter, D. Mull, G. S. Petrich. W. D. Goodhue, S. Prasad, L. A. Kolodziejski, C. G. Fonstad Jr.' "Practical OEICs based on the monolithic integration of GaAs-InGaP LEDs with commercial GaAs VLSI electronics", IEEE J. Quantum Electron., vol. 34, no. 7, 1117-1123, 1998.
[23] A. G. Chynoweth, W. L. Feldman, and R. A. Logan, "Excess tunnel current in silicon Esaki junctions", Phys. Rev., vol. 121, no. 3, 684-694, 1961.
[24] A. E. Youtz, B. Nabet, "Role of intermediate temperature molecular beam epitaxy grown GaAs defects in tunneling and diffusion", Journ of Appl. Phys., vol. 64, no. 5, 2697-2703, 1998.

Chapter 3: Bipolar cascade lasers

3.0 Overview

This chapter covers the details of the realization of bipolar cascade lasers (BCLs). Section 3.1 describes a phenomenological treatment of BCLs, from the rate equation point of view. The reader is assumed to have a basic understanding of lasers and the rate equations. The interested reader lacking this background is referred to Appendix B or references [1, 2, 3] where a review of the rate equations and the derivation of important results therein are given. Section 3.2 explains the materials and growth research that was necessary to grow high optical quality active regions which were also compatible with the growth of high electrical quality tunnel junctions. The knowledge gained from the materials and growth studies lead to the demonstration of the first room temperature (RT), continuous wave (CW) BCL. The results of the characterization of this device are given in Section 3.3. The extensive thermal modeling of the BCL is detailed in section 3.4. Non-idealities in the performance of the BCL are described addressed in Section 3.5. Section 3.7 considers the modulation response of the laser. The characterization process of the first generation BCL lead to an improved design of a second generation BCL. The details of this device are presented in Section 3.7. Section 3.8 summarizes the major results to conclude the chapter.

3.1 Cascade laser theory

This section covers the modeling of the BCL using rate equations. The purpose of the modeling is to derive light output power versus bias current, and device voltage versus bias current relationships. To achieve these ends the device carrier densities or, equivalently, the device quasi-Fermi levels must be known or calculated. All other quantities of interest may then be derived to include current density, voltage, gain, photon density, and output power.

The physical structure of the BCL consists of two separate waveguiding/gain sections, electrically coupled by a tunnel junction in reverse bias. To first order, the gain

sections may be viewed as being electrically independent, with the exception that the current in both the upper and lower gain sections (and the tunnel junction) must be equal. In order to model the device, the threshold carrier density must first be calculated. To begin, a logarithmic fit to the gain per unit length of a quantum well versus carrier density [1] is assumed:

$$g = g_o \ln\left(\frac{N}{N_{tr}}\right) \tag{3.1}$$

where N_{tr} is the carrier density at which the quantum well transitions from being lossy (i.e. negative gain) to having positive gain and g_o is a fitting parameter. The functional form of Eqn. 3.1 results from band filling, leading to a roll off in the rate at which the gain improves with increasing carrier density.

For the laser to reach threshold the gain must nearly equal the total optical loss of the device through absorption and from output coupling through the end facets of the laser. The *modal gain* is defined as Eqn. 3.1 times the overlap of the optical field with the gain region. The overlap of the optical field with the gain region is termed the confinement factor. Mathematically the threshold requirement is written as:

$$\Gamma g_{th} = \alpha_i + \alpha_m \tag{3.2}$$

where Γ is the confinement factor, α_i is the optical loss per unit length due to absorption and scattering and α_m is the mirror loss per unit length. Combining Eqns. 3.1 and 3.2 gives the following for the threshold carrier density:

$$N_{th} = N_{tr} e^{\left(\frac{\alpha_i + \alpha_m}{\Gamma g_o}\right)} \tag{3.3}$$

Given Eqn. 3.3 the quasi-Fermi level may be calculated through the Fermi integral given by:

$$N = \int \rho_c(E) f(E) dE$$

(3.4)

where N is the electron carrier density, ρ_c is the density of states in the conduction band and f(E) is the Fermi distribution. The integral should rigorously be carried out from the bottom of the conduction band to the top of the conduction band. In practice, the upper limit of integration is normally taken to infinity, as the Fermi distribution drops off rapidly a few thermal voltages above the quasi-Fermi level. When calculating the integral numerically, the upper limit of integration need only be so large as is necessary for the Fermi function to become negligibly small. This depends upon the location of the quasi-Fermi level. In a quantum well (a two dimensional system) the density of states is given by:

$$\rho(E) = \sum_n \frac{m^* L_z^2}{2\pi\hbar^2} u(E - E_n)$$

(3.5)

where m* is the electron effective mass, L_z is the quantum well width, E_n are the quantized energy levels in the quantum well (which vary with effective mass, barrier height, and barrier width), u(E) is the unit step function, and ħ is Planck's constant over 2π. Note that for two-dimensional systems the density of states is independent of energy between quantized levels. The Fermi distribution is given as:

$$f(E) = \frac{1}{e^{(E-E_{fn})/kT} + 1}$$

(3.6)

where E_{fn} is the electron quasi-Fermi level, k is Boltzmann's constant and T is the temperature. Given an electron carrier density Eqn. 3.4 may be solved to find the associated quasi-Fermi level. The equation may either be solved numerically using an iterative approach or semi-analytically using any one of a number of approximations to the Fermi integral [1]. One must be careful in using approximations to the Fermi integral to ensure that the limits of validity aren't compromised. Another approach is to

assume values for the quasi-Fermi levels over some range less than the threshold quasi-Fermi level (which must still be calculated) and then calculate the corresponding carrier density. The latter is the method used in the calculations presented in this section. In using this method it is necessary to use a very fine mesh between quasi-Fermi level values as threshold is approached.

Quasi-neutrality is assumed to hold through out the active region. This is to say that N~P in the active region, where N and P are the number of carriers per unit volume for the electrons and holes, respectively. If this were not the case then large electric fields would build, bending the bands to allow carrier redistribution until quasi-neutrality would again be established. Therefore, once a set of carrier density values has been obtained for the electrons, the same set of carrier density values is assumed for the holes. Then using equations similar to Eqns. 3.4-3.6 for the holes, the hole quasi-Fermi levels are calculated versus carrier density. Knowing the carrier density versus quasi-Fermi level affords easy calculation, from Eqn. 3.1, of the gain versus carrier density.

It is a straightforward matter now to derive the current versus carrier density relationship. Setting the time derivatives in the rate equations (Eqns. 7 in Appendix B) equal to zero (in the steady state) and after some manipulation:

$$I = \frac{qV_{act}BN^2}{\eta_i}\left(1+\frac{\Gamma\beta v_{gr}g}{\frac{1}{\tau_p}-\Gamma v_{gr}g}\right) \tag{3.7}$$

where q is the electron charge, V_{act} the active area volume, B the bimolecular recombination coefficient, η_i the injection efficiency, β the spontaneous emission factor, v_{gr} the group velocity, and τ_p the photon lifetime.

The output optical power can then be calculated from Eqn. 15 in Appendix B:

$$P_o = v_g \alpha_m N_p h\nu V_p \tag{3.8}$$

where N_p is the photon density (per unit volume), V_p is the volume occupied by the photons and $h\nu$ is the photon energy.

The same sets of values may now be calculated for the bottom gain section subject to the constraint that the current is continuous through out the BCL. The continuity of the current through the device does not imply, however, that the carrier density is also the same everywhere. Assuming the material in the bottom and top active regions are comparable in quality then all the parameters previously defined for the top gain section should have the same values for the bottom gain section, with the exception of one. In a stripe geometry laser, such as those used in the first BCLs as described below, the current spreads laterally as it moves through the device. Therefore the active region volume is larger in the bottom gain section than in the top. One would therefore expect different values for the threshold current, quasi-Fermi levels, carrier densities, and optical power at a given current bias from the bottom gain stage than for the top gain stage.

As is shown in Fig. 3-1, the carrier density of the top gain stage clamps before that of the bottom gain stage. The simulation assumes a stripe width of 20 μm for the top gain section and a 30 μm stripe width for the bottom gain section. Normally when a laser reaches threshold all additional carriers injected into the active area are transduced into photons. As such, the voltage across the device clamps, save for a small additional contribution due to the non-zero resistances of the contacts and bulk regions. By examining Fig. 3-1 it can be observed that the carrier density of the top gain stage clamps at 15 mA while the bottom gain stage does so at approximately 23 mA. Clearly then, in the BCL, when multiple thresholds are present, the top device clamps, but the voltage continues to increase across the bottom gain stage until it also clamps at threshold. While the device voltage versus current curve remains smooth, Fig. 3-2a, the light power versus current exhibits a clear double kink behavior (Fig. 3-2b). Of course, enough of the applied voltage must appear across the tunnel junction to ensure current continuity in the device. This double threshold behavior, while interesting, is problematic. Sections 3.3 and 3.4 below cover in detail the difficulties introduced by the double threshold. Fig. 3-3 shows the dependence of the normalized threshold voltage, differential efficiency and threshold current on the number of gain stages. In the cases of the normalized threshold

voltage and differential efficiency the scaling is in direct proportion to the number of stages. Ideally, the threshold current is independent of the number of gain stages but in the presence of lateral diffusion the threshold current (defined as the current at which all gain stages are lasing) does increase with the number of gain stages, Fig. 3-3. The concentration dependent diffusivity is assumed to be the same as assumed for Fig. 3-1 through 3-3. While the quantitative agreement between the simulations and the device light power versus bias current is questionable, the qualitative agreement provides important insight into the BCL's behavior.

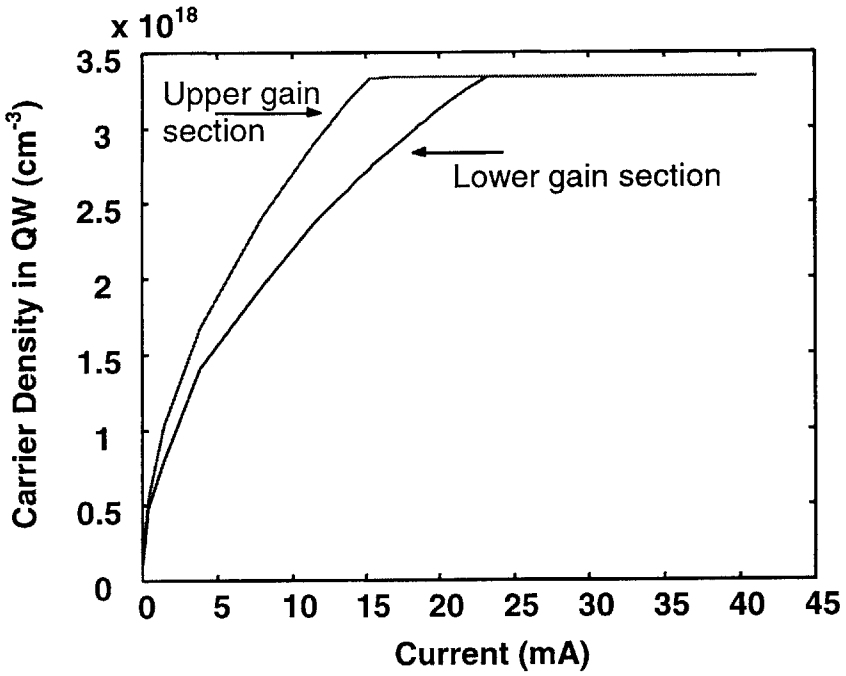

Figure 3-1. The carrier density versus bias current in a 20 μm by 500 μm two-stage bipolar cascade laser. Due to current spreading, the carrier density in the upper gain section saturates at a lower bias current than the lower section.

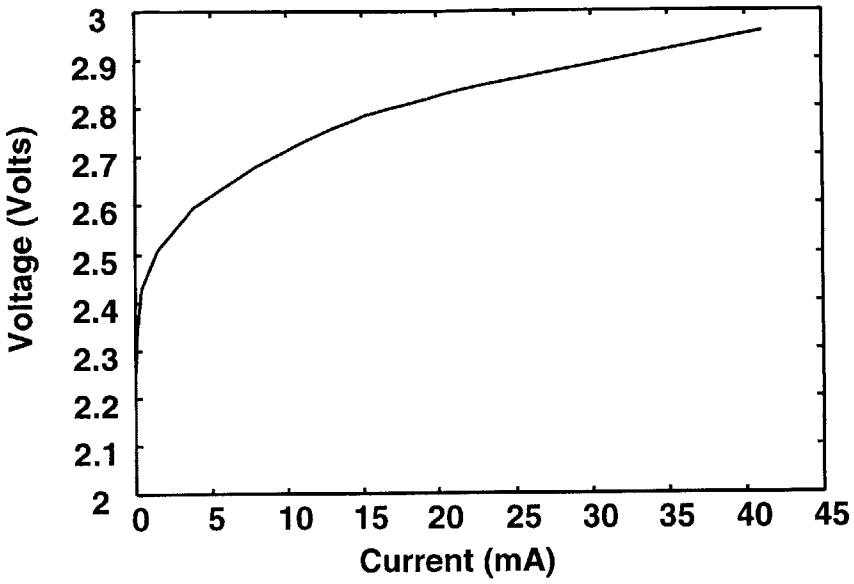

(a)

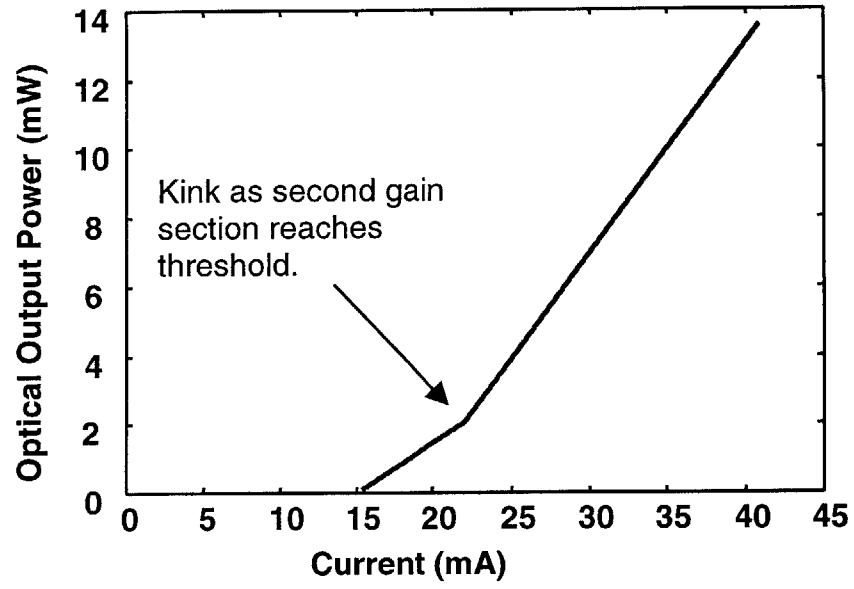

(b)

Figure 3-2 a) The voltage versus bias current of the device of Fig. 3-1. The curve is smooth despite current spreading and exhibits a voltage drop of two diodes plus ohmic losses (taken as 6 Ω). b) The light power versus bias current characteristics for the BCL of Fig. 3-1. Current spreading results in a kink in the output power when the bottom gain stage reaches threshold.

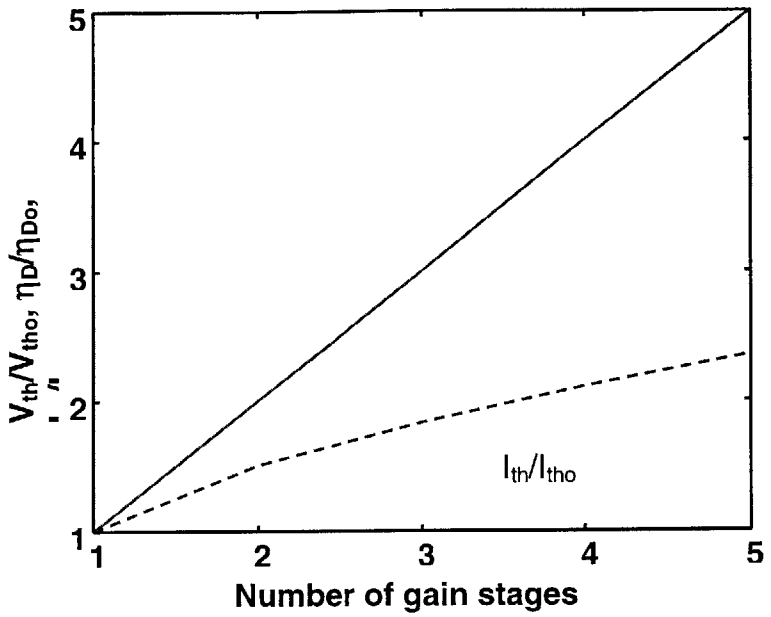

Figure 3-3. The normalized increase in V_{th}/V_{tho}, η_D/η_{Do}, I_{th}/I_{tho} versus the number of gain stages. As the number of stages is increased the threshold voltage and peak quantum efficiency increase linearly. Ideally the threshold current is unaffected by the number of gain stages. When current spreading is present, the threshold current (defined as the current at which all gain stages are lasing) also increases with the number of gain stages.

3.2 Materials growth of semiconductor lasers

3.2.1 Single stage lasers

The realization of bipolar cascade lasers first necessitated the growth and processing of single stage, conventional quantum well lasers that could operate at room temperature and continuous wave. This endeavor was further complicated by the requirement that, as outlined in Chapter 2, the lasers that were to serve as the gain stages in the BCL had to be compatible with the growth and maintenance of high quality tunnel junctions. Since Be, the p-type dopant, diffuses very rapidly as a function of temperature [4-8], even a high quality junction could be rendered unusable if the overgrowth of the upper gain stage required substrate temperatures elevated above the point where rapid Be diffusion begins. As detailed in Chapter 2, the first BCL was implemented at an

emission wavelength of 980 nm. The material typically used in the cladding of edge emitting lasers operating at 980 nm wavelength is 30–40% aluminum mole fraction AlGaAs. Aluminum containing materials are typically grown at substrate temperatures of ~ 640 °C. This temperature prevents substantial oxygen incorporation during growth. Oxygen exists as a deep level trap in AlGaAs, capturing carriers before they can participate in radiative recombination events. The first laser growth experiments, directed toward meeting the growth requirements for a BCL, had the aim of determining whether AlGaAs clad lasers, if grown at temperatures commensurate with high electrical quality tunnel junctions, would be of suitably high optical quality.

The initial test structures were standard edge emitting configurations (Fig. 3-4). A single 80 Å wide $In_{0.2}Ga_{0.8}As$ quantum well was placed inside a 0.22 μm wide GaAs waveguide. The waveguide width was chosen to maximize Γ as defined in Section 3.1. The structure was grown on a Si doped (n-type $1\text{-}3\cdot10^{18}$) GaAs substrate. The cladding layers were 0.5 μm thick n- and p-type $Al_{0.4}Ga_{0.6}As$. The entire structure, with the exception of the 1 μm thick buffer layer (grown at substrate temperature of 600 °C), was grown at a substrate temperature of 480 °C. A highly p-doped (~ $1\cdot10^{19}$) 0.1 μm cap layer, for making an Ohmic contact, completed the structure.

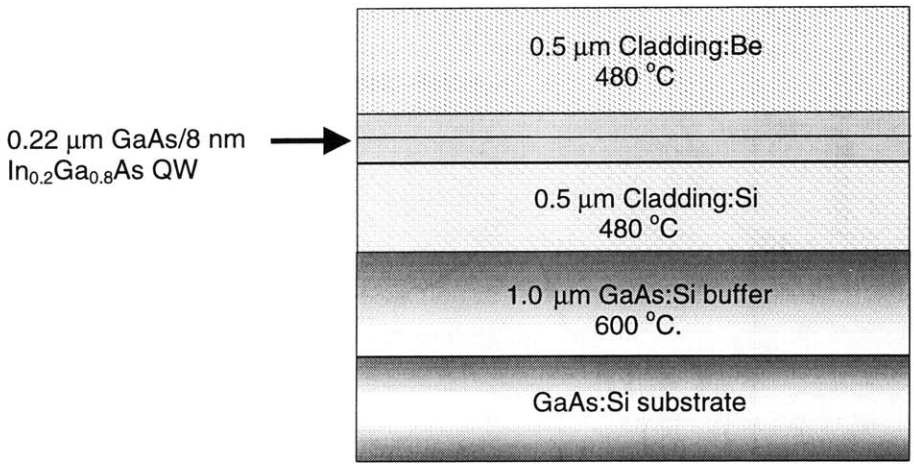

Figure 3-4. The test structure used to study the effect of substrate temperature upon the optical qualities of a single stage edge-emitting laser. The buffer was grown at 600 °C and the cladding layers at 480 °C. The growth temperature of the active region varied by structure.

To determine the optical quality of the material a photoluminescence study was performed. Photoluminescence consists of making a laser beam, of photon energy greater than the bandgap energy of the waveguide material, incident upon the sample. Since the electron thermalization rate is faster than the spontaneous recombination rate, photons absorbed either in the active region, or within a diffusion length of the active region, generate electron-hole pairs that typically emit radiation from the n=1 state of the quantum well. The light re-radiated from the sample is collected and made incident upon a monochromator. The output of the monochromator is detected by a photodiode or photomultiplier. The monochromator is scanned so the light intensity versus wavelength may be recorded. The bottom-most trace of Fig. 3-5 shows the photoluminescence intensity versus wavelength for the AlGaAs-clad structure described above. The performance is very poor, with the signal intensity barely above the noise floor. Furthermore, and perhaps most importantly, laser structures processed from the AlGaAs-clad material failed to lase.

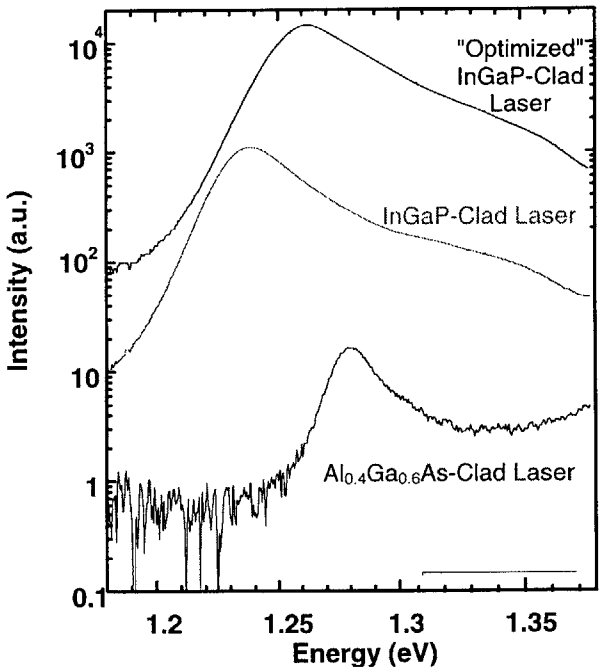

Figure 3-5. The photoluminescence intensity versus energy of the three test structures used to determine acceptable substrate temperatures for growth of the bipolar cascade laser.

Two alternative approaches can be considered in addressing the problem of the suitability of AlGaAs as the cladding material. Studies could be done to determine to the temperature, and length of time, the substrate could be raised before the tunnel junction degraded. The above process for an AlGaAs-clad laser could then be repeated to ascertain if such a substrate temperature and growth rate would yield a laser of acceptable optical quality. In a similar vane, the mole fraction of Al in the AlGaAs could be reduced in the hopes that a higher optical quality laser would result. This approach would again require a fairly extensive set of growth experiments. Additionally, given the vicissitudes of MBE growth, particularly in a research environment, it is difficult to draw broad conclusions based upon such studies until they prove repeatable.

The second possibility for solution exists in switching to a different cladding material entirely. Cladding material based upon indium-gallium-phosphide (InGaP), lattice matched to GaAs, has gained some favor over AlGaAs in recent years in high power laser applications [9-11]. It is well known that oxidation of AlGaAs can lead to catastrophic optical mirror damage in AlGaAs-clad lasers [9, 12]. InGaP does not suffer from the problem of oxidation making it a good choice for the cladding material in high power lasers. While such a consideration is only of secondary importance for the BCL the successful replacement of AlGaAs with InGaP in edge emitting lasers offers another advantage. For the purposes of the BCL work, InGaP is a favorable material because it is typically grown in the temperature range of 480-510 °C [12]. This author had previously established that in the GSMBE used for this work, InGaP is optimally grown at 480 °C [13]. To compare the optical quality of lasers grown with InGaP versus AlGaAs cladding, the growth and photoluminescence experiments outlined above for the AlGaAs-clad lasers were repeated for InGaP-clad lasers. The structure and growth procedures were exactly as those described above for the AlGaAs-clad lasers; the substrate temperature throughout the device growth was kept constant at 480 °C.

The centermost trace in Fig. 3-5 indicates that the photoluminescence intensity for the InGaP-clad laser was a full two orders of magnitude greater than the intensity of the AlGaAs-clad laser. A laser fabricated from this material structure did lase (Fig. 3-6) and it represents the first continuous wave, room temperature operation of a semiconductor laser grown and fabricated at MIT. The devices were gain guided, oxide-stripe defined,

Fabry-Perot cavity lasers. Longevity tests also provide a measure of the quality of the laser material. At an output power of 19 mW per facet, a 500 μm long, 10 μm wide device showed no degradation in over 72 hours of continuous wave, room temperature operation, without the benefit of heat sinking, further indicating laser material of very high quality.

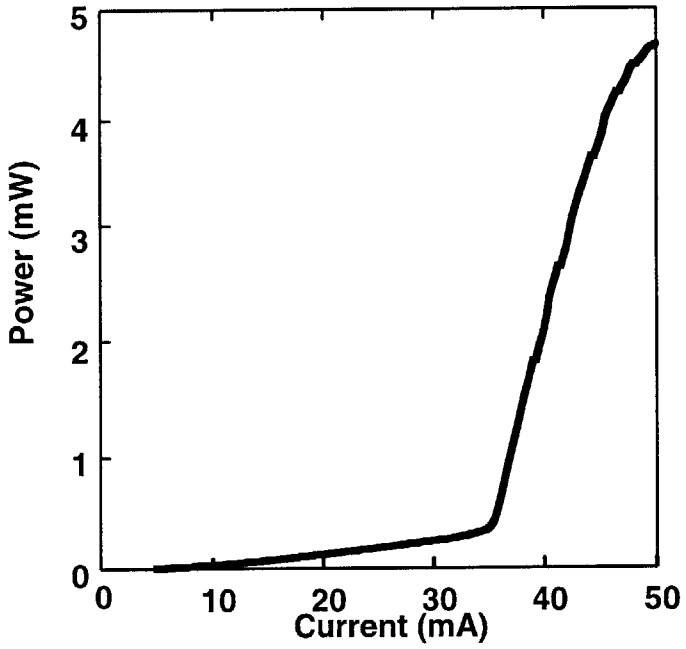

Figure 3-6. The light power versus bias current for a an aluminum free single stage edge emitting lasers. The continuous wave threshold current density is 330 A/cm^2. The device is of a gain-guided, oxide-stripe defined Fabry-Perot cavity design. The stripe width is 25 μm and the device is 400 μm long.

While the InGaP structure outperformed the AlGaAs by two orders of magnitude in photoluminescence efficiency and demonstrated excellent lasing properties, it does not indicate that the InGaP structure grown entirely at 480 °C was in any way optimal. To evaluate the limit of performance of the material in an InGaP-clad structure another device structure, of precisely the same design as that detailed above for the structures grown at 480 °C, was grown with each layer grown at its "optimal" growth temperature. The result of this procedure was another order of magnitude improvement in photoluminescence efficiency as shown by the topmost trace in Fig. 3-2. How much of this improvement could be attributed to the "optimization" of the growth process and

how much is due to the vagaries of MBE growth remains uncertain. While good, an order of magnitude is actually not spectacular and a variation of this order can be expected across the wafer itself. In all cases, with each subsequent photoluminescence measurement, previously measured samples were re-measured to ensure that direct comparisons were being made between samples and the results were not tainted by systematic errors.

3.2.2 Active region growth

While the best substrate temperatures for high electrical and optical quality lattice-matched InGaP ($In_{0.49}Ga_{0.51}P$) and GaAs were known from previous work by this author, optimal growth temperatures for the quantum well remained undetermined. A series of experiments were done of single $In_{0.2}Ga_{0.8}As$ quantum wells clad on either side by 0.5 μm of unintentionally doped GaAs (background doping of ~10^{15} p-type), again measuring the photoluminescence intensity versus growth temperature. From this study, a growth temperature of 515 °C was established to produce the highest optical quality quantum wells. The literature suggests that post growth, ex-situ anneals of 10 seconds at 900 °C further enhance the luminosity of the quantum wells [14], but this was deemed to be deleterious to the maintenance of abrupt tunnel junctions. Another study indicated that the growth of the quantum wells at a substrate temperature of 555 °C obviated the anneal step, producing quantum wells of comparable optical quality to those grown at lower substrate temperatures and subsequent annealing [15]. Time and equipment availability prevented this technique from being tried. Furthermore, even a brief stint at 555 °C could cause an unacceptably high amount of diffusion in the tunnel junction. It is highly likely that an adjustment of arsenic overpressure would be in order to preserve good In adsorption and incorporation on to the surface. Addressing such concerns and determining the full parameter space of growth conditions versus quantum well optical performance are worthy of further study.

3.2.3 Growth considerations at interfaces

Careful consideration had to be given to the InGaP/GaAs and GaAs/InGaAs interfaces of the "optimally" grown structure. If the substrate is raised to 600 °C at an InGaP terminated interface, phosphorous desorption will occur. To prevent the desorption from occurring, 25 nm of GaAs was grown at the InGaP to GaAs interface while the substrate temperature was being ramped from 480 °C to 515 °C. From that point, with a steady arsenic overpressure, the growth was interrupted and the substrate was ramped to 600 °C before the growth was reestablished. The GaAs waveguide was then grown to within 25 nm of the quantum well and then interrupted. The substrate temperature was lowered to 515 °C and allowed three minutes to stabilize before the final 25 nm of GaAs was grown. Upon completion of the 25 nm of GaAs the quantum well was immediately grown. At the completion of the quantum well, the GaAs waveguide growth was reinitiated without delay and a 25 nm cap was placed over the quantum well. The substrate was ramped to the target GaAs temperature and the growth was reinitiated without waiting for cell temperature stabilization. Such measures were necessary as it was established during the quantum well growth temperature study that extended growth interruption at the GaAs/InGaAs QW interface had a dramatic deleterious effect upon the QW's photoluminescence efficiency.

The growth of the GaAs waveguide continued uninterrupted until the growth was within 25 nm of the GaAs/InGaP interface. The growth was interrupted at this point and the substrate temperature was lowered to 515 °C. The final 25 nm of GaAs waveguide was grown while the substrate temperature ramped down to 480 °C. The InGaP growth was immediately initiated upon the completion of the waveguide without waiting for the substrate to reach equilibrium. This is justified as small temperature fluctuations don't greatly effect material quality. It is unknown how uniform the temperature distribution was across the wafer and this can effect material quality as a function of radial position on the wafer. The temperature gradient over the wafer was of less concern than the poor distribution of constituents over the wafer, a problem resulting from the emission patterns of the Knudsen cells. The nonuniform molecular beam typically rendered the material in

a circle of about 1/2-3/4 inch diameter in the center of the wafer far superior to that at the edges.

A word on the group V switch over at InGaP/GaAs and GaAs/InGaP interfaces is in order. The phosphorous source in GSMBE is cracked phosphine (HP_3). This author determined that the best gas change over results occurred, with respect to interface quality, when the outgoing group V was shut off and then 10 to 20 seconds were permitted to pass before switching in the new group V. The group III flux(es) were shuttered in 10 seconds later. The issue of optimal gas change over is far from resolved, with different studies utilizing various changeover procedures appearing in the literature [17, 18]. While optimizing this portion of the growth is to some degree important, it does not appear absolutely pivotal. It does remain another growth issue worthy of study should the BCL move from the research stage to the developmental stage.

3.2.4 BCL design and growth

The gain sections used in the BCL are very similar to the optimized single stage InGaP-clad lasers detailed in Section 3.2.1. The primary change involves the use of 0.75 μm of InGaP as the cladding layers rather than only 0.5 μm (Fig. 3-7). Doing so reduces optical losses by decreasing the optical field overlap with the tunnel junction and the topside contact. Radiation loss resulting from the low to high index transition at the lower InGaP to GaAs substrate interface is also diminished. While these losses are small, it would be desirable to even further diminish these losses by having even thicker cladding layers. There was concern about the stability of the In/Ga flux ratio over the course of the three hours needed to grow the four layers of 0.75 μm of InGaP, however. No in-situ technique for monitoring the material composition in real time was available. The use of the Ga cell while the In cell remained shuttered off during the growth of the waveguiding/active sections and the numerous In and Ga cell temperature changes over the course of the growth were also cause for concern regarding In and Ga flux rate stability. Lattice mismatches between the epitaxial InGaP and the GaAs is tolerable but if the composition of the InGaP wandered too far from lattice match then the InGaP could relax and destroy the electrical properties of the structure [19]. The 0.75 μm layers

represented a reasonable compromise between acceptable loss and the believed limit of reliable lattice-matched InGaP growth.

The same growth procedure was used for the gain stages as for the "optimized" InGaP laser, with the exception of the GaAs waveguides. While the InGaP structure grown entirely at 480 °C proved to have very good lasing properties, the results of the "optimized" structure promised even better results. It was decided to attempt an improvement of the 480 °C structure by growing the entire waveguide/QW region at 515 °C. The effect of the ~30 minute excursion to 515 °C while growing the uppermost gain stage on the underlying tunnel junction was undetermined prior to its attempt in a BCL structure. Nevertheless, the BCL was initially grown with the entire waveguiding/QW region being grown at 515 °C. A secondary ion mass spectroscopy (SIMS) study of the as-grown structure was performed. As detailed in Chapter 2, the SIMS indicated the dopant location and density were as predicted by the earlier growth and Hall studies, with no indication of temperature dependent diffusion of the Be away from the junction.

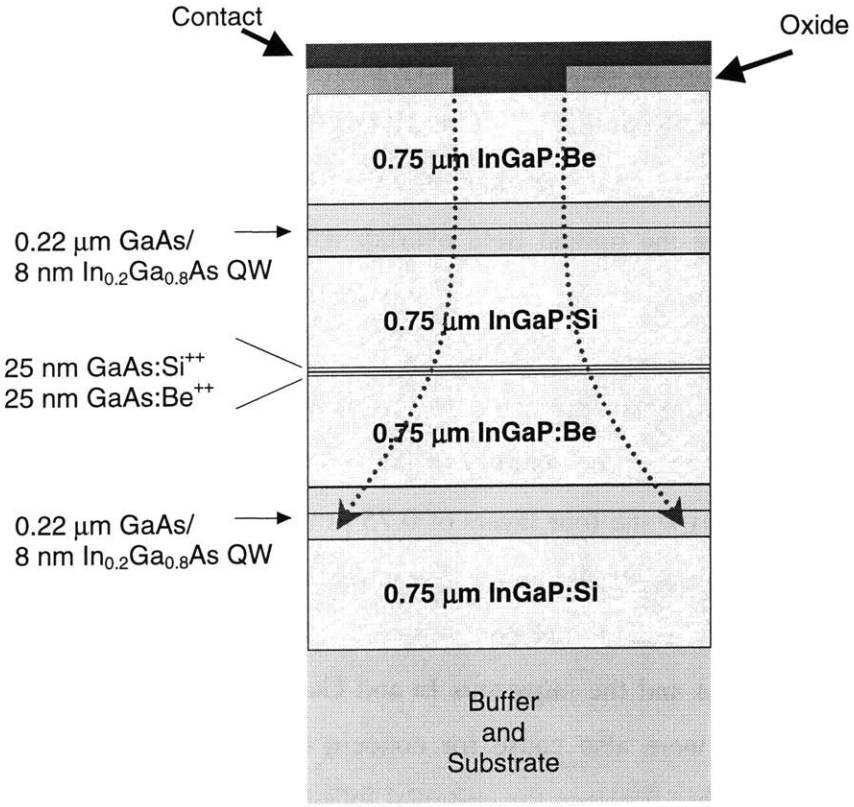

Figure 3-7. The device structure for the first bipolar cascade laser. Two nominally equivalent edge emitting lasers are connected electrically in series by a narrow tunnel junction. Dotted arrows indicate current spreading.

3.3 BCL Characterization

Shown in Fig. 3-8 are the light power versus current (L-I) characteristics of the first room temperature, continuous wave BCL. The device was a 450 μm long, 5 μm wide, oxide-stripe defined, gain guided Fabry-Perot laser. There is some interesting structure to the L-I characteristics. At the point of the onset of lasing there is an abrupt jump in output power. This is attributed to a saturable absorption effect. It is well known that lateral carrier diffusion away from the electrically pumped region directly below the contact stripe results in a region of absorption for the optical field in narrow stripe, gain guided lasers [20, 21]. When the optical field absorption reaches the point that the diffusively pumped region reaches transparency (i.e. the absorption saturates) the effective optical loss diminishes sharply. Self-pulsations may be seen in the time domain for narrow stripe, gain-guided lasers and they are often used commercially in compact disc players. Time domain measurements of the narrow stripe BCLs revealed self-pulsating behavior. The wider stripe devices (> 10 μm) exhibited neither self-pulsating behavior nor the saturable absorption effect seen in the L-I characteristics of Fig. 3-8.

There is an abrupt switch over from a slope efficiency of 0.32 Watts/Amp (W/A) per facet to 0.63 W/A visible in Fig. 3-8 at about 56 mA of drive current. This equates to a differential quantum efficiency of 99.3%, the highest ever reported in an interband laser operating continuously at room temperature. A differential quantum efficiency of over 93% is maintained out to 60 mA when the device begins to thermally roll over. The sudden increase in slope efficiency indicates that initially only one active region is lasing and then it is followed by the other gain stage at a higher input current value. In this case the separate values of threshold are current are due to lateral current spreading as explained in Section 3.1. As described in the previous paragraph the current spreads laterally as it moves through the device. The *current density* is lower in the bottom gain stage than the top even though the *current* is continuous through the device [22]. The pumped area of the lower gain stage is greater than the top gain stage, hence the lower gain stage reaches threshold at a higher terminal current than the top device.

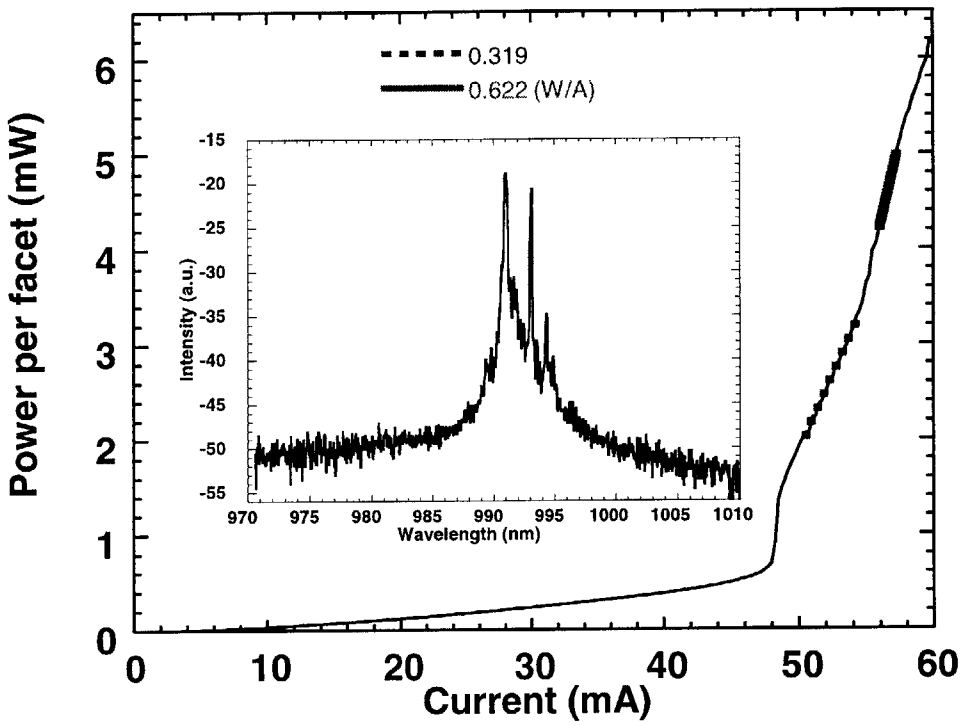

Figure 3-8. The light power versus bias current of the first room temperature, continuous wave bipolar cascade laser. Inset is the ouput spectrum at 56 mA bias current. Upon onset of lasing in the bottom gain stage the output slope efficiency abruptly switches from 0.32 W/A to 0.62 W/A for a quantum efficiency of 99.3%. The BCL is a 5 μm wide, 450 μm long, gain-guided, Fabry-Perot, oxide-stripe defined device. A saturable absorption effect is visible near the onset of lasing of the top gain stage.

The inset shows the spectrum of the BCL immediately past the onset of lasing of the second junction. The quantum wells in the two different gain stages are nearly degenerate with one lasing at 991 nm and the other at 993 nm. Although the intent was to make the two wells degenerate in emission wavelength, it is still surprising that they are so similar given the time that elapsed between the growth of each one. This is a good indication that the MBE was very stable through the growth and the material in the two gain stages is of comparable quality. There is some indication of device heating as the room temperature photoluminescence emission wavelength for the BCL was at 978 nm.

The heat sinking of the device of Fig. 3-8 consisted only of make press contact between the n-side metalization and the measurement stage. The temperature of the stage was not stabilized during the measurement. The L-I characteristics of the device indicate that it was thermally rolling over at a rather low level of bias (60 mA). It was clear that a more adequate method of heat sinking the device was necessary. Since no in-house procedure was available at this early stage of the work, several of the most promising laser bars were sent out of house to be heat sunk. The heat sinking proved to be catastrophic as all the bars were rendered inoperable through end facet damage.

Fig. 3-9 shows the current-voltage characteristics of the BCL device of Fig. 3-8. The figure 3-shows that the voltage drop across the device is somewhat greater than twice the voltage drop of two diodes (two times the n=1 band-to-band voltage in the QW), providing further evidence that the cascading process is taking place. Most interestingly, the differential resistance of the entire device is only 5 Ω. Such a small value is obtained because the contact resistance of the tunnel junction is believed to have been dramatically reduced by deep state assisted tunneling in the junction (see Chapter 2). Therefore, the differential resistance of the BCL structure is dominated by the contact resistance at the p-type contact layer.

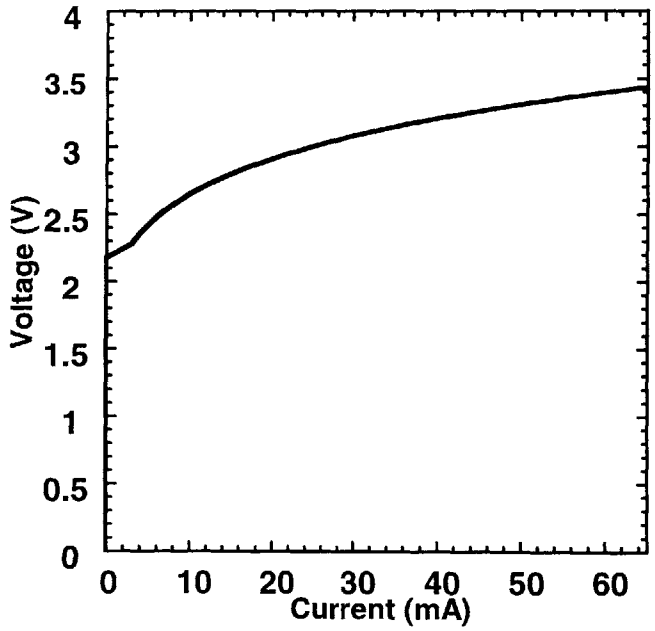

Figure 3-9. The voltage versus current of the device of Fig 8. The differential resistance of the device is only 5 Ω. There are clearly two diode drops across the device.

Another BCL structure was grown, nominally the same in every way as to the BCL described above, except in this case the top quantum well was designed for emission at 950 nm while the bottom well remained at 980 nm. This non-degenerate (or two-tone) structure served a two-fold purpose. It allowed the spectra versus current of the two gain stages to be investigated separately and, in so doing, it could be determined if any injection locking was taking place between the two gain stages. Fig. 3-10 shows the input current versus spectral density of the non-degenerate BCL. The dark images indicate both the spectral location and intensity of the non-degenerate BCL output. The spectra versus bias plot of Fig. 3-10 also substantiates the previous assumption that it is the top gain stage which is the first to lase. The top gain stage begins to lase at ~ 52 mA. The bottom gain stage does not begin to lase until ~ 130 mA. By the time the bottom gain stage reaches threshold the performance of the top gain stage has been compromised. This is evidenced in Fig. 3-10 by the broadening of the spectral linewidth of the top gain stage prior to the onset of lasing in the bottom gain stage. Also worthy of note is the increase in lasing wavelength versus bias of both quantum wells. Wavelength shifting is normally indicative of active region heating. Thermal effects and the thermal modeling of the BCL are the subjects of the next section.

Before moving on to the discussion of BCL thermal issues, a quick word is in order with respect to the study of the two-tone device and the injection locking of the two gain stages. Luarent, et al. [23] performed a study of a two-stage bipolar cascade laser, with the gain stages physically separated by 1 μm, and observed injection locking of the devices at 1530 nm indicating the possibility of coherent output from a BCL using separate waveguides for the separate gain stages. The close proximity of the gain stages required for coherent locking resulted in a rather hefty loss of 40 cm^{-1} due to tunnel junction induced optical absorption loss and the device was operated only pulsed. The two-tone BCL of this thesis described in the latter two paragraphs showed no evidence of injection locking over any range of biasing. The energy difference between the two QWs of 40 meV requires a large amount of coupled power to effect injection locking. The physical distance which separates the two gain stages was > 1.5 μm at a wavelength of only ~ 980 nm allowed an insufficiently small amount of energy coupling between the two waveguides.

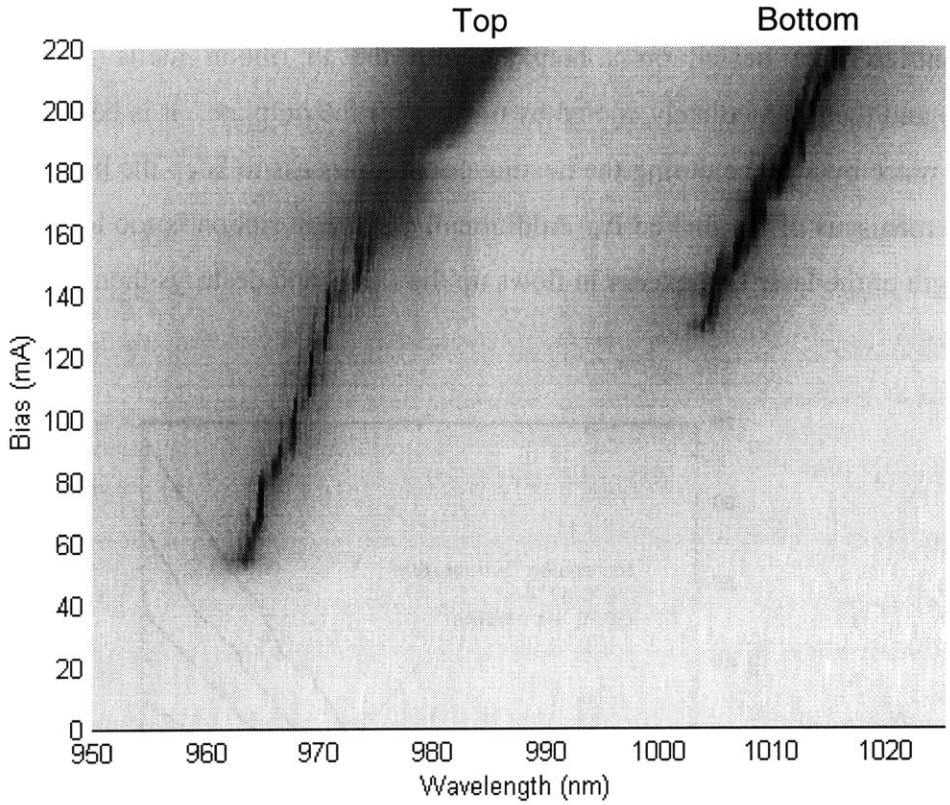

Figure 3-10. The bias current versus emission wavelength for a two-tone BCL. The darker the image, the more intense the output. The top gain stage turns on first. By the time the second gain stage reaches threshold the top stage has begun to thermally roll-over. The heating of the device is evident in the blue shift with increasing bias.

3.4 Thermal modeling of the bipolar cascade laser

Several of the results of Section 3.3 point toward thermally related problems with the BCL. As alluded to in the previous section the measurements were done without any particular attention being paid to the heat sinking process. Before proceeding with the thermal studies of the BCL it was necessary to improve the heat sinking of the device to thoroughly explore the thermal effects that were hinted at by the study of the two-tone device described in Section 3.3.

Adequate heat sinking was achieved by laying a section of one mil thick indium ribbon, of length and width approximately equal to that of the laser bar to be heat sunk, atop a Au-plated rectangular mount made of copper/brass. The In ribbon was lightly brushed with liquid solder flux and the laser bar was positioned over the In ribbon with

the leading edge of the laser bar flush with, or slightly beyond, the edge of the mount. The mount/laser are heated on a hotplate until the In ribbon melts (~165-170 °C indicated) and then immediately cooled by turning off the hotplate. It is best that the bar is held in place by a probe during the heating/cooling process to keep the bar from riding up on the meniscus of the melted In. Additionally, if the In ribbon is too long compared to the length of the laser bar, excess In flows up the facets and destroys them.

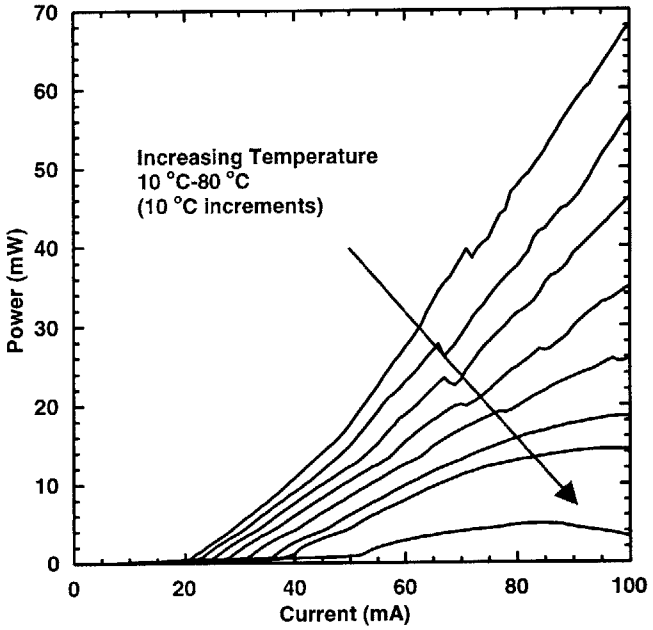

Figure 3-11. The light power versus bias current for a 20 μm wide, 300 μm long device. One facet has been high-reflection coated to 95%. The BCL continues to lase to a substrate temperature of 80 °C, but the bottom gain stage only lases to a substrate temperature of 40 °C. The peak room temperature slope efficiency is 93%.

The devices used in the thermal study for this section were processed and cleaved from the same wafer as the first RT, CW degenerate wavelength BCL of the last section. They were then heat sunk in accordance with the latter described process. The devices are 300 μm long devices with a single high-reflectivity (HR) coated facet (R = 95%). All devices were of the same oxide-stripe defined, Fabry-Perot, gain-guided design used for the devices of the previous section. The lasing wavelength of both QWs is again ~ 990 nm. Shown in Fig. 3-11 is the temperature dependence of the light power vs. injected

current for a representative 20 μm wide HR-coated device. The RT, CW peak slope of the output is 1.12 W/A (a differential slope efficiency of 93%). This device continues to lase at heat sink temperatures up to 80 °C. Below the heatsink temperature of 50 °C, an abrupt change in slope efficiency can be observed at ~ 50 mA, indicating the second junction has achieved threshold. Above heatsink temperatures of 50 °C the second junction does not exhibit a clear lasing threshold.

An important figure of merit of a laser is the characteristic temperature, T_o, which describes the sensitivity of the devices threshold current to changes in temperature (Fig. 3-12). The temperature dependent behavior of the threshold current is given by:

$$I_{th} = I_{thO} e^{\left(\frac{T}{T_o}\right)} \tag{3.9}$$

The functional form of this expression is motivated by considering Eqn. 19 of Appendix B. It can be shown from more fundamental analysis than given in Section 3.1 and Appendix B that the differential gain goes approximately proportionally to $1/T^2$ while the internal loss goes proportionally to T. Therefore the threshold current is expected to go exponentially with temperature.

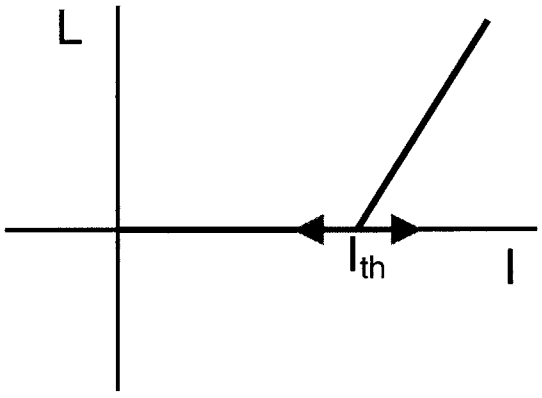

Figure 3-12. The definition of T_o. T_o characterizes the sensitivity if the threshold current to temperature.

Fig. 3-13 clearly indicates that, for the BCL devices being studied here, the continuous-wave T_o is 102.5 K over the heatsink temperature range of 10-40 °C, but drops off dramatically to 55.7 K for heatsink temperatures in the range of 50-80 °C. Over the entire temperature range of operation T_o = 76 K. The qualitative temperature performance of the BCL is similar to that of conventional lasers. A detailed study of the performance of conventional, two QW designs using InGaP cladding, InGaAs active regions, and GaAs waveguide regions, was reported in [12]. The devices of [12] exhibit dramatic degradation in performance (T_o and internal loss) for temperatures greater than 40 °C, and for devices less than 600 μm in length. In [12, 24], internal optical loss was found to increase dramatically (doubling to tripling) for heat sink temperatures greater than ~ 40-50 °C. Other studies of conventional broad area InGaP/InGaAsP/InGaAs lasers, operated *pulsed*, have reported T_o values of 194 K (in the temperature range 10-50 °C) [25], and 223 K [27] for devices operated in the heatsink temperature range of 10-40 °C. The increase in quasi-Fermi level separation required to reach threshold with increasing temperature, and the associated smearing of the Fermi distributions, was proposed in [24] as the mechanism responsible for the temperature dependent optical losses.

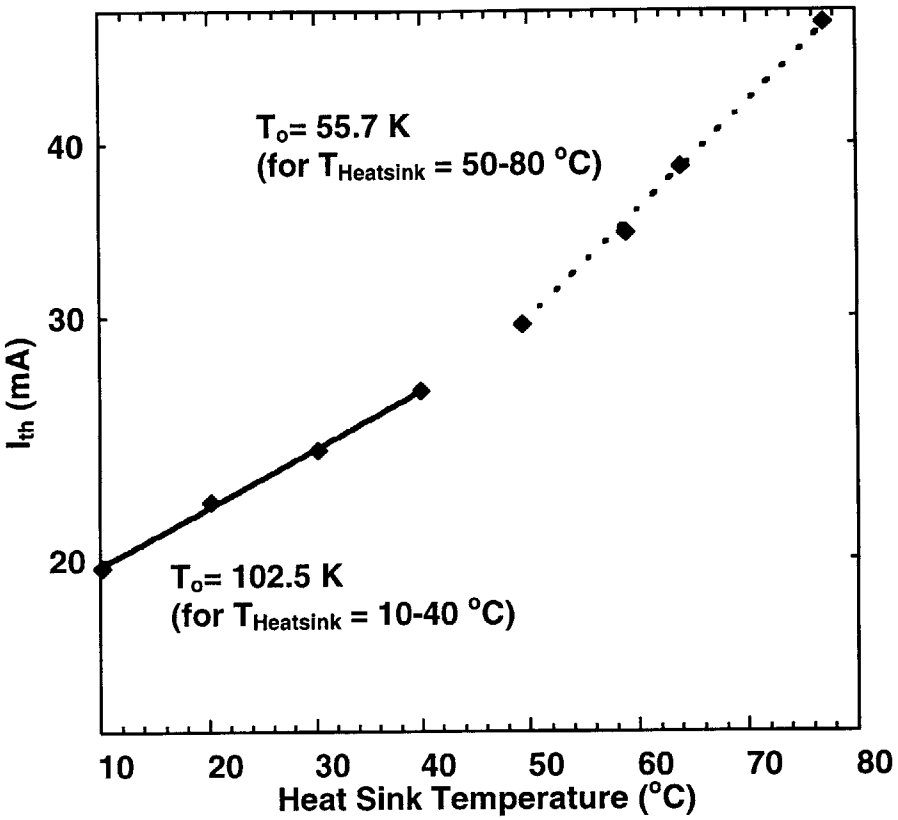

Figure 3-13. The differential slope efficiency versus heat sink temperature for the device of Fig. 3-11. The characteristic temperature, T_o, drops drastically above heat sink temperatures of 40 °C.

The signal-to-noise ratio in optical links employing directly modulated lasers goes to the square of the differential slope efficiency of the lasers [26]. Therefore, the temperature dependence of the differential slope efficiency, characterized by the temperature T_1, merits study (Fig. 3-14). Using arguments similar to those used to motivate Eqn. 3.9, the temperature dependence of the differential slope efficiency may be modeled as:

$$\eta_D = \eta_{Do} e^{\left(\frac{T}{T_1}\right)} \tag{3.10}$$

Two values for T_1 can be extracted for the BCL, corresponding to the temperature dependence of the differential slope efficiency both below and above the onset of lasing

in the bottom gain stage in the L-I slope. For the 20 μm wide HR coated device, the values of T_1 are 104.5 K (below the bottom gain stage's threshold) and 46.7 K (above the bottom gain stage's threshold) (Fig. 3-15). Here again, consistent with the reported increase of optical loss with temperature, it is seen that T_1 drops most dramatically above heatsink temperatures of 40-50 °C (from 104.5 K to 47.6 K). Note that in the heat sink temperature range of 50-80 °C only the bottom gain stage lases.

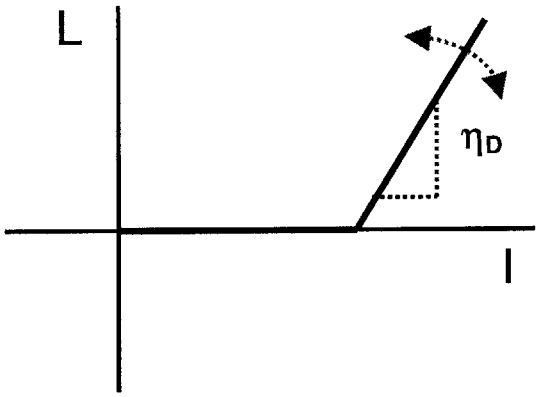

Figure 3-14. The definition of T_1. T_1 characterizes the sensitivity of the device's slope efficiency to temperature.

While the electrical series coupling of the two QWs of the BCL accounts for the device's high slope efficiencies, the series thermal coupling of the two QWs in the BCL was expected to be problematic. The two QWs of a conventional multiple quantum well laser are also thermally connected in series, but in the conventional laser each QW has an associated DC power dissipation of $I_{th} \cdot V_{diode}/2$, while for the BCL each active region dissipates $I_{th} \cdot V_{diode}$ of DC power. To quantify this hypothesis, the top surface temperatures of the BCL and a conventional single QW InGaP/GaAs/InGaAs laser were measured as a function of bias current density.

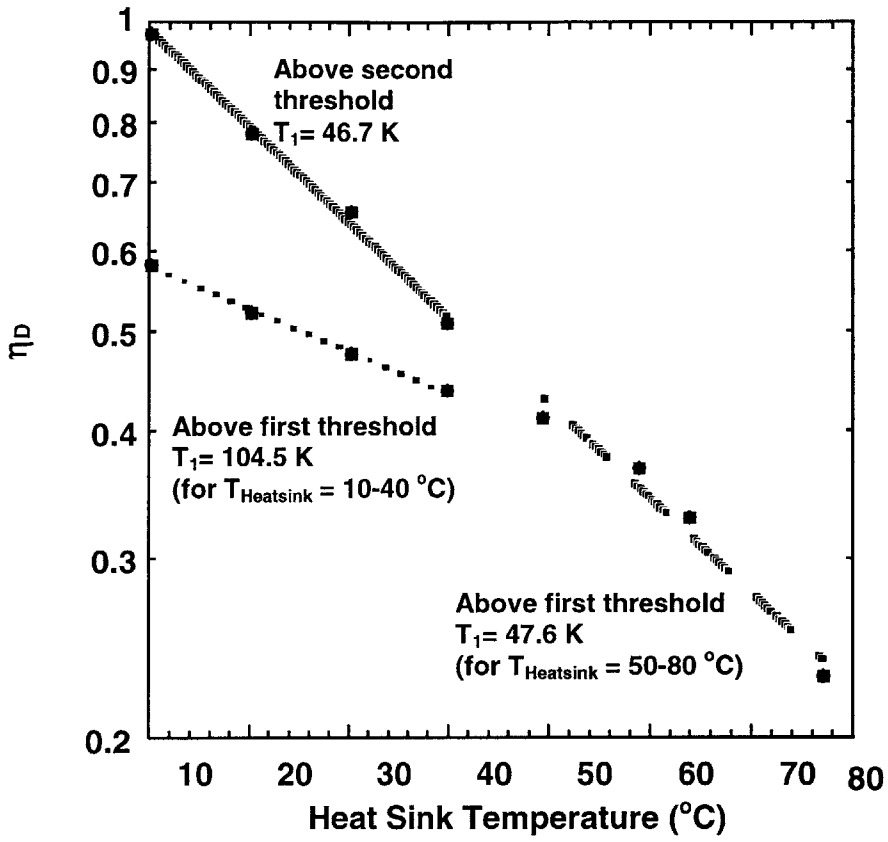

Figure 3-15. The differential slope efficiency versus heat sink temperature for the device of Fig. 3-11. The upper gain stage demonstrates a sharp decrease in T_1 above heat sink temperatures of 40 °C. The lower gain stage only lases up to a heat sink temperature of 40 °C and has a T_1 similar to the upper gain stage above 40 °C.

The data points in Fig. 3-16 show the surface temperature of a 20 μm wide and 300 μm long BCL (with different L-I characteristics than those of the above described device) and an uncoated conventional 20 μm wide, 500 μm long InGaP/GaAs/InGaAs laser vs. current density. The BCL's threshold current is 40 mA and the conventional laser's is 80 mA. The length of the conventional laser was chosen so as to have similar mirror losses as the BCL. Measurements were made by directly touching a calibrated micro-thermocouple to the metal biasing contacts. The micro-thermocouple was calibrated against a NIST-traceable thermistor known to be precise to +/- 10 mK and accurate to 2 K. The Cu/constantan metal leads of the thermocouple are approximately 25 μm in diameter and hence have a thermal mass too small to effect the surface

temperature of the lasers during the measurement. The bottom-side heatsink temperature was maintained at 20 °C with the laser submount thermally connected to the heatsink via thermally conductive silicone paste. The BCL heats over twice as quickly as the conventional single QW device. Secondary evidence of the increased temperature of the QW is found by comparing the slope efficiency of the single QW conventional laser with the slope efficiency of the BCL. The conventional device has a slope efficiency of 60%, while the BCL's 93% efficiency is well below the expected 120% efficiency.

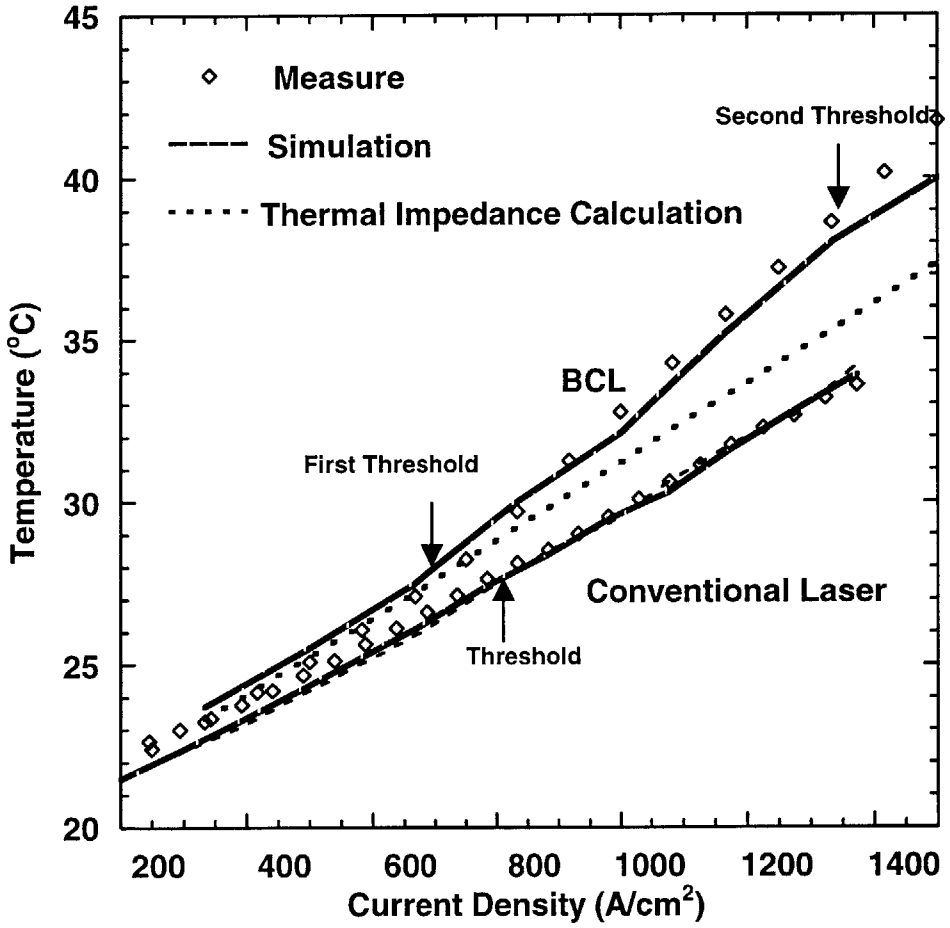

Figure 3-16. The surface temperature versus current density of a device similar to the device of Fig. 3-11. Finite element simulations agree quite well with measured surface temperature values. An analytical model agrees with measurement and simulation for the conventional laser underestimates the surface temperature in the BCL above the top gain stage's threshold.

To put these observations on firmer quantitative footing, finite element modeling of both the BCL and the conventional, single stage InGaP/InGaAs/GaAs laser was performed. In the simulations, non-radiative recombination in the QW/waveguiding regions acted as the primary heat sources, with a small contribution from Joule heating-as estimated from the measured differential resistance. In the case of the BCL, below the threshold of either gain stage, the power dissipation for each gain stage was set equal to one half of the product of the measured current and voltage bias across the device, minus emitted radiation and differential resistance losses ($I \cdot V - P_{out} - I^2 R_{differential}$). The $I^2 R_{differential}$ loss was taken to occur at the topside contact since $R_{differential}$ is dominated by the p-type contact resistance. Above the threshold of the top active region, all further increases in voltage across the device were taken to occur across the bottom, non-lasing junction (nearfield imaging has confirmed the top active region is the first to reach threshold). Above threshold, the emitted light power was subtracted from the I·V power product. The bottom boundary condition of the simulations was set equal to the heatsink temperature of 20 °C, while the lateral boundaries were set equal to the measured values 150 μm to either side of the device under test. The metal contact-air interface boundary was modeled using a Neumann boundary condition ($dT/dx = 1.2 \times 10^{-7}$ K/cm). Fig. 3-17a shows the results of a typical simulation. Fig. 3-17b indicates the locations of the thermal sources in the simulations.

The most striking and important result illuminated by the simulation, however, is that even when the voltage of the lasing (top) gain stage is clamped, the unclamped (non-lasing) bottom gain stage continues to act as a significant source of heating for the top active region. While current spreading through the device results in a threshold current which is larger for the bottom gain stage than the top, the top gain stage also acts as a heat source for the bottom gain stage, further delaying onset of lasing for the bottom gain stage. The poor thermal properties of the ternary semiconductor alloys, such as InGaP, and the low aspect ratio of the GaAs waveguide prevent good lateral heat conduction while little heat dissipates through the poorly conducting metal contact-air interface. By the time the bottom gain stage reaches threshold, the thermally increased optical losses have compromised the differential slope efficiency of the BCL.

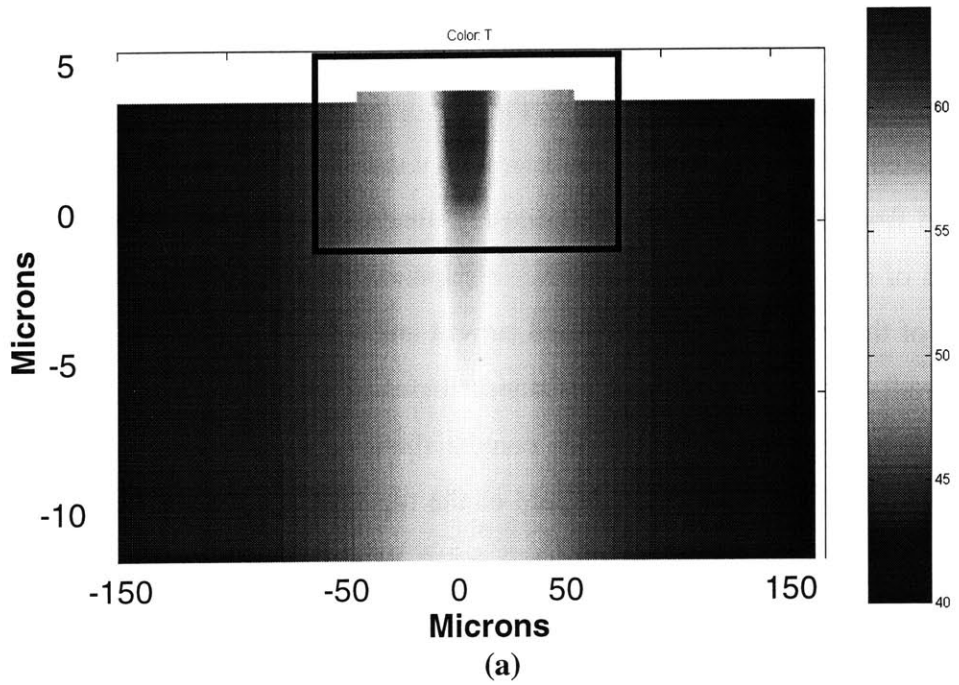

(a)

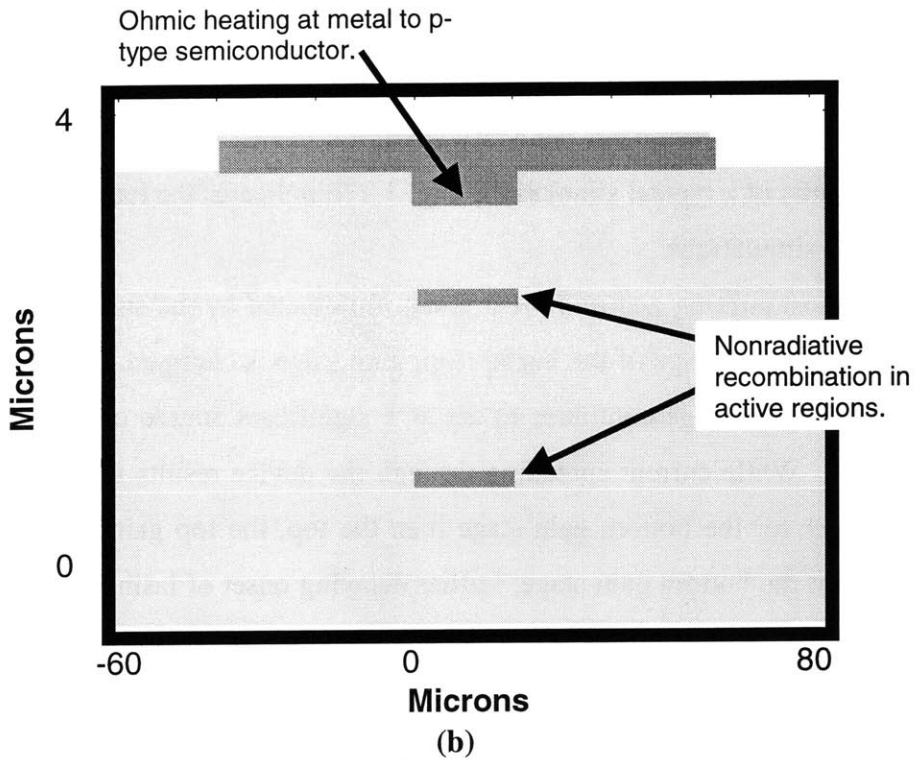

(b)

Figure 3-17. a) A finite element simulation of the BCL. The simulation extends to -150 μm in the vertical direction (not shown). Most heat conduction occurs laterally. b) An enlargement of the region in the black square of a). Ohmic losses were modeled at the top contact-semiconductor interface while non-radiative losses were modeled in the active regions.

The solid lines in Fig. 3-16 show the surface temperature values as determined by simulation. Very good agreement between simulation and measurement is shown, indicating the simulations can provide valuable insight into the temperature distribution within the devices. The temperature of both active regions was found to be nearly equal to that of the surface. Ideally, it is expected that upon reaching threshold all additional power input into a laser is transduced into laser light, save for a small amount consumed by Joule heating, with a resultant sharp decrease in the rate of device heating. The dashed lines in Fig. 3-16 are the active region temperatures calculated using the thermal impedance given by:

$$Z_T \cong \frac{\ln\left(\frac{4h}{w}\right)}{(\pi\zeta l)} \tag{3.11}$$

where h is the height of the device, w is the stripe width, l the length of the device and ζ the thermal impedance of the material. There is excellent agreement between the calculation based upon Z_T and the measurements of the surface temperature for the conventional device. For the BCL, agreement is good for bias current densities less than 800 A/cm^2, but divergent behavior is exhibited beyond the onset of lasing in the top active region. This result is anomalous and may be indicative of a thermally activated source of non-radiative recombination outside of the active region. Such a supposition is purely speculative and warrants additional study.

Epilayer-side heat sinking has proven effective for unipolar cascade lasers, raising the CW operating temperature by 20 K [28]. Improvements in threshold current, output power and slope efficiency were also realized. Considering the very poor thermal dissipation through the topside contact highlighted in the finite element modeling, it is perfectly reasonable to expect that epilayer-side heat sinking would yield similar improvements for the BCL. In a sense though, topside heat sinking is a brute force approach to obtaining better performance from the BCL, particularly when considerable improvement can be expected from design changes. The measurements and modeling done thus far point the way toward a superior BCL design, and this will be the subject of

Section 3.7. First, Section 3.5 addresses non-idealities in the gain guided devices used in the first generation BCLs while Section 3.6 briefly discusses the modulation properties of the BCL.

3.5 Antiguiding and other non-ideal behavior in BCLs

While stripe geometry lasers enjoy the advantage of relatively simple processing and fabrication, they do suffer from certain disadvantages. One such difficulty lies in the characteristic of semiconductors to exhibit a strong optical index dependence on carrier density [29]. The index of GaAs decreases with increasing carrier density. The index depression created by the carrier injection into the active area rejects, or antiguides, the light. For narrow stripe devices (4-12 μm in width), the antiguiding phenomena can lead to rather bizarre behavior in the light power versus current characteristics of a stripe geometry laser, particularly in InGaAs-GaAs devices [29]. Shown in Fig. 3-18 are the L-I characteristics of a BCL exhibiting antiguiding behavior.

The behavior exhibited in Fig. 3-18 can be explained as follows. The device begins to lase in the fundamental transition of the quantum well, but the gain saturates before the carrier induced index change [30]. The decrease in the index increases the anitguiding and, hence, the amount of diffraction loss. The increase in diffraction loss dictates an increase in gain, leading to larger carrier densities and more antiguiding. When the losses eventually override the gain increases, lasing ceases. As the current density is increased even further, the higher lying quantum well states begin to become more heavily populated and lasing is reestablished, but at a different wavelength. This phenomenon was established by observing the spectral content of a BCL. In short devices (< 500 μm), the increased carrier density needed to overcome the increased mirror losses may prevent lasing from ever occuring at the lowest order quantum well transition. In some cases, the quantum well laser has been reported to act as a bulk double heterostructure laser with the observed lasing energy to be that of the GaAs waveguide [29, 30].

It is not completely clear why some devices exhibit the antiguiding behavior shown in Fig.18 while others exhibit reasonably well behaved properties such as those

described in Section 3.3. It is known that the material quality diminishes rapidly as one moves further from the center of the wafer. Material of poorer quality can be expected to have a higher threshold current value, leading to enhanced antiguiding effects. Even variations in the quality of the heat sinking or cleaving in superior material could result in the same increased-threshold induced antiguiding effects.

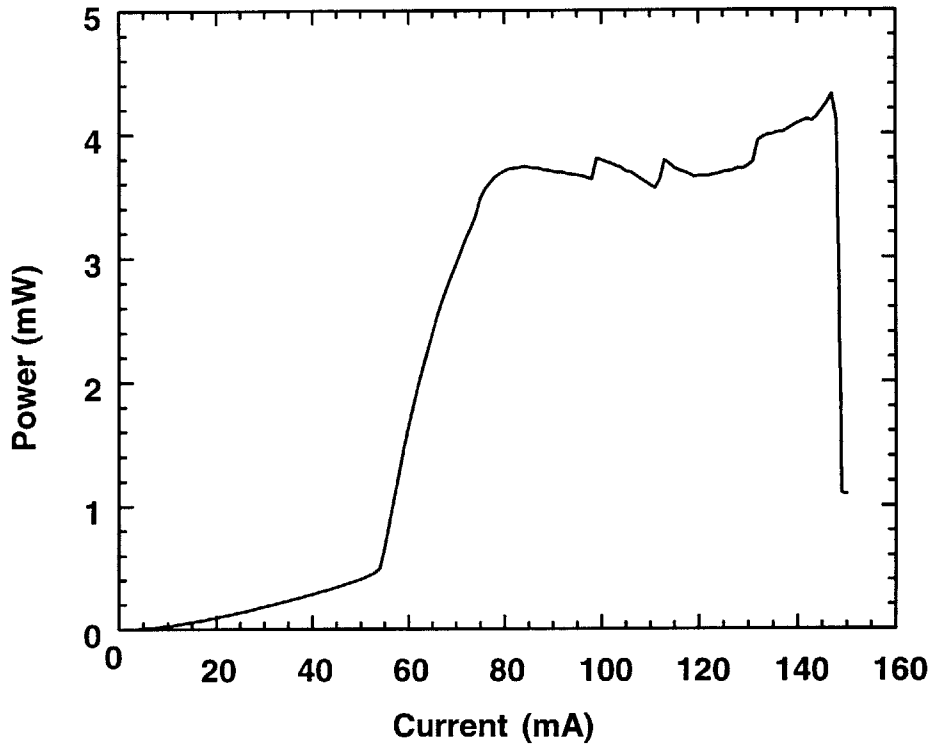

Figure 3-18. Antiguiding behavior in an oxide-stripe defined, gain guided, Fabry-Perot BCL. The index depression created by the carrier density in the active region rejects the optical mode leading to bias dependent losses.

While devices in excess of ~10 μm stripe width did not display saturable absorption, self-pulsations, or antiguiding effects, very wide devices (30-40 μm) did not show superior slope efficiency performance. In the wider devices, the double threshold current behavior so evident in the narrow stripe devices is expected to be less severe or almost none existent. The degree of lateral diffusion between the top and bottom gain sections is a constant (presuming a reasonable carrier lifetime) for a given carrier density with a given diffusion length, regardless of the stripe width. Hence a 10 μm wide stripe

and a 40 μm stripe will have, just for argument sake, 5 μm of lateral diffusion. However, the percentage change for the 40 μm wide device (12.5% change) is considerably smaller than for the 10 μm wide device (50% change). Fig. 3-19 displays the L-I curve for a 40 μm wide, 500 μm long BCL. The peak slope efficiency of this device is only 73%. While this is clearly more than the 55-60% of a single stage laser, it is significantly less than the 90-100% seen in narrower stripe lasers. It is far from clear as to the reason for this result, as the threshold currents for these wide stripe devices are not much greater than for the narrower stripe devices. A possible explanation, but one without firm empirical footing, is the wider stripe devices are more likely to have a defect within the strip region. The material used for the first generation BCLs had what appeared to be an abnormally high particulate count on the surface of the wafer. The nature or cause of these defects is not presently known.

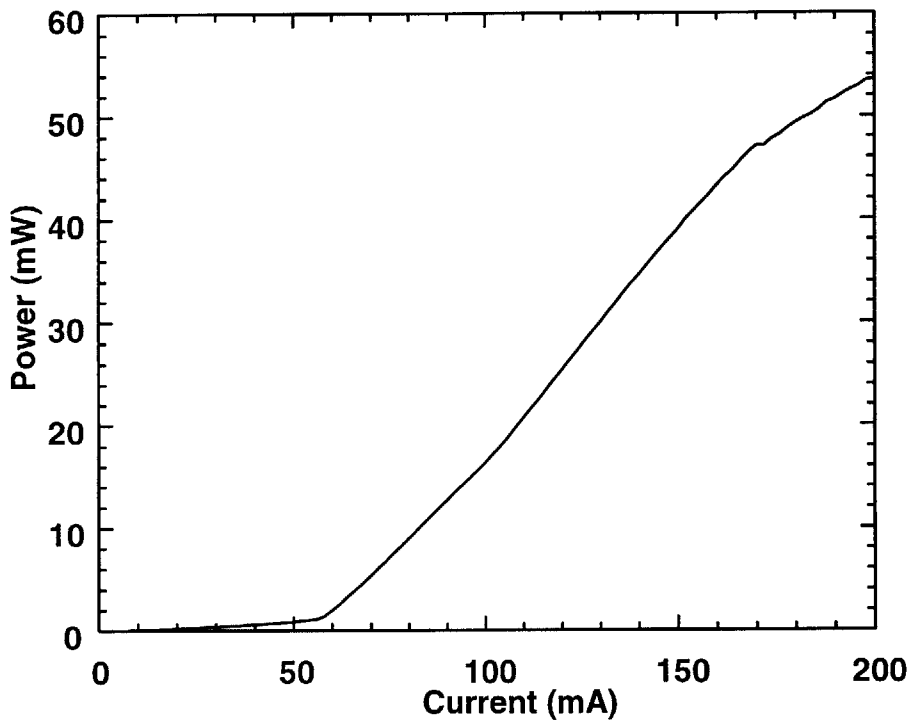

Figure 3-19. The light power versus bias current characteristics of a gain guided, oxide-stripe, Fabry-Perot laser 40 μm wide by 500 μm long BCL. The kink in the L-I characteristic is less pronounced than in narrower stripe devices. The device only achieves a peak slope of efficiency 77%.

3.6 Modulation properties of the bipolar cascade laser

The study of bipolar cascade lasers is interesting in its own right but the intended application for the BCL is in directly modulated optical links. Therefore the modulation properties of the device are of interest and are the subject of this section. Fig. 3-20 shows the relative intensity noise (RIN) spectrum of the BCL. RIN is defined as the ratio of the mean square power fluctuations divided by the square of the steady state optical power. Studying of the RIN properties of a laser is an excellent method of investigating the devices parasitic-free dynamic behavior. Of note is the large peaks that rise before the frequency response of the device rolls over. The peaks result from the natural resonance frequency of the laser, also known as the relaxation oscillation frequency (see below). As expected, the relaxation oscillation frequency of the BCL increases with bias current but the maximum frequency of ~1.6 GHz at 70 mA bias (at 35 mW of output power) is considerably less than the transport limited of nearly 10 GHz that would be expected for this laser [31]. Beyond 70 mA bias the relaxation oscillation frequency begins to diminish. The poor result is due to the *differential* gain being compromised to heating.

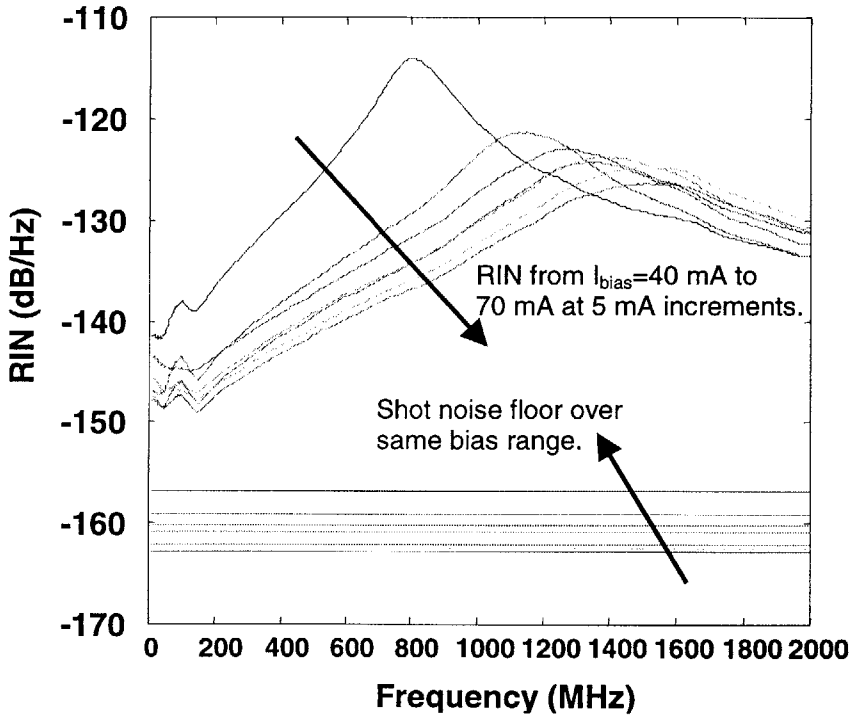

Figure 3-20. The relative intensity noise versus frequency for a 7 μm wide, 300 μm long BCL with a single facet high reflection coated at 95% reflectivity.

In Section 3.4 it was determined that the performance of the BCL was compromised due to thermal effects. As the active region heats the Fermi distribution begins to smear, requiring a higher total carrier density to achieve a population inversion at the intended lasing wavelength. The differential gain, which can be easily derived by taking the derivative with respect to N of Eqn. 3.1, is given by:

$$\frac{\partial g}{\partial N} = \frac{g_o}{N} \tag{3.26}$$

Eqn. 3.26 clearly indicates that an increase in carrier density results in a decrease in the differential gain of the device. Hence, the relaxation oscillation frequency:

$$\omega_R = \sqrt{\frac{v_g \frac{\partial g}{\partial N} N_p}{\tau_p}} \tag{3.27}$$

suffers degradation. The relaxation oscillation frequency sets an upper bound on the maximum modulation frequency of the device. Increasing the photon density, N_p, requires increased current and leads to the associated increase in heating. Therefore an increase in the photon density via increased biasing does not lead to the marked improvement in the relaxation oscillation frequency that Eqn. 3.27 would suggest.

Another figure 3-of merit for directly modulated lasers is the spur free dynamic range (SFDR). The SFDR is defined, with two tone input modulation, as the input power range over which the fundamental tones are detectable above the noise floor while the distortion products of interest are below the noise floor. For narrow band applications, such as would be the case for the BCL, the largest odd order distortion products are most important because these fall within the detection bandwidth. Fig. 3-21 shows the third order intermod SFDR for the BCL. The set-up used to perform the measurement is described in [32]. The output of the laser was coupled directly into the photodetector. The SFDR was measured to be 104 dB-$Hz^{2/3}$. This is a mediocre and values in excess of

110 dB-$Hz^{2/3}$ are desirable in links. Again, the SFDR performance of the device is believed to be due to the reduction in differential gain resulting from thermal effects.

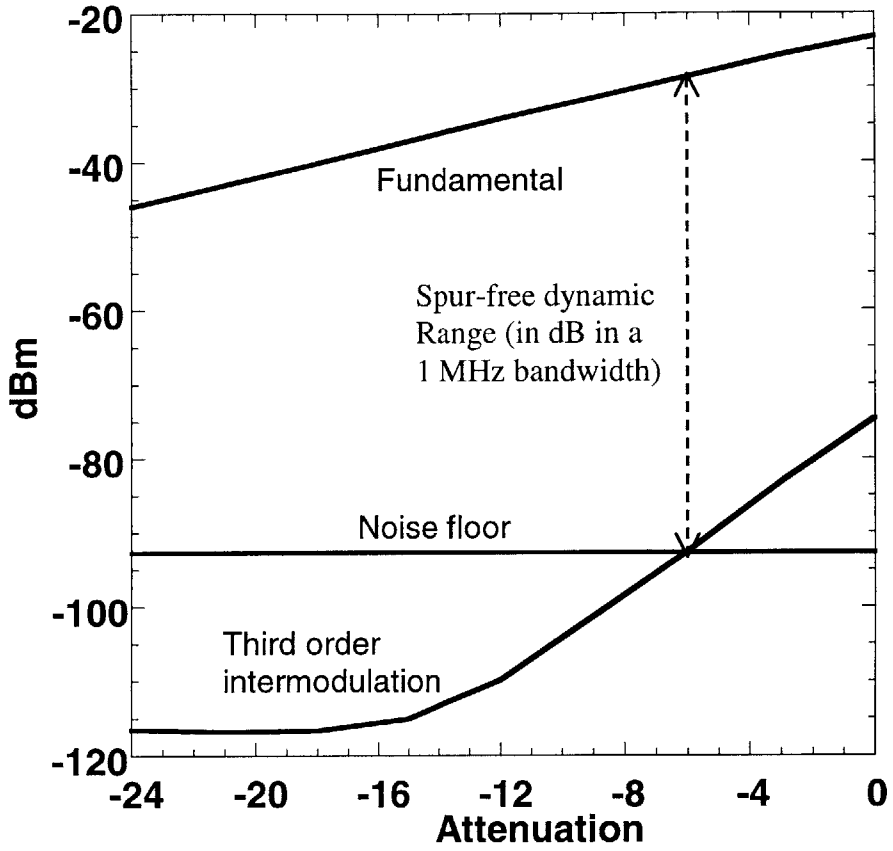

Figure 3-21. The spurious free dynamic range of a 7 μm wide, 500 μm long HR-coated (R=95%) BCL. The measurement was taken at 74 mA of bias at center frequency of 100 MHz and Δf=2 MHz. The dynamic range is 104 dB-$Hz^{2/3}$.

3.7 The second generation bipolar cascade laser

The measurement and modeling of the bipolar cascade laser as described in the past two sections point the way toward improvement of the design. The key issues highlighted were ones of thermal power dissipation, lateral current diffusion resulting in different threshold currents for the top and bottom gain sections, and perhaps the gain guided nature of the devices. While the very nature of the principles of operation of the BCL dictate that the voltage drop across the device must be equal to the number of gain stages times the voltage associated with the wavelength of emission, it is possible to reduce the operating current of the BCL. Reducing the threshold current of a laser results

in reduced operating power for a given output power. The device has hence become more efficient in converting electrical power to optical power, thereby reducing the negative thermal effects associated with the direct current power dissipation in the device. Further examination of Eqn. 3.7 also indicates that decreasing α_i would also increase the power conversion efficiency of the device, as well as the differential slope efficiency (Eqn. 17 Appendix B).

While the differential slope efficiency also benefits from increasing in α_m, Eqn. B.20 reveals it would be unwise to do so, as the threshold current is exponentially dependent upon the mirror loss. The injection efficiency is primarily a function of device geometry. All things considered, reducing the optical loss is the best method to decrease the threshold current and increase the differential slope efficiency of the BCL.

The primary source of optical loss in the first generation BCL was free carrier absorption in the cladding. Free carrier loss can be reduced by lowering the doping density in the cladding. Doing so increases the series resistance of the BCL and, concomitantly, the thermal power dissipation in the BCL. Another approach is to broaden the waveguide section. Broadening the waveguide reduces the overlap of the optical field with the doped cladding region (Fig. 3-22a). The reduction in the field overlap with the cladding region is also accompanied by a reduction in Γ (where Γ is defined as the overlap of the optical field with the active region). Fig. 3-22b shows the reduction in Γ with an increase in the waveguide width. Apparent from Fig. 3-22 is that while both the optical field overlap with the cladding and Γ both diminish with increasing waveguide width, the Γ diminishes much less slowly than the cladding overlap. In going from a waveguide of 0.22 μm in width (the waveguide width in the first generation BCL) to one of 0.6 μm in width, the overlap with the cladding decreases by a factor of four, while Γ only by a factor of two. Beyond a waveguide width of 0.72 μm the second order mode begins to propagate, placing a natural limit on the width of the guide.

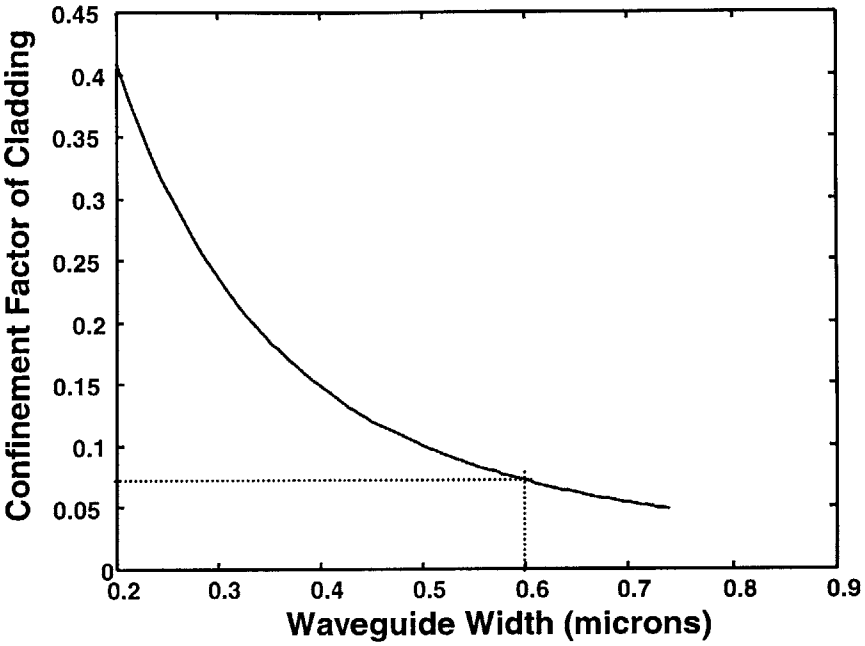

a)

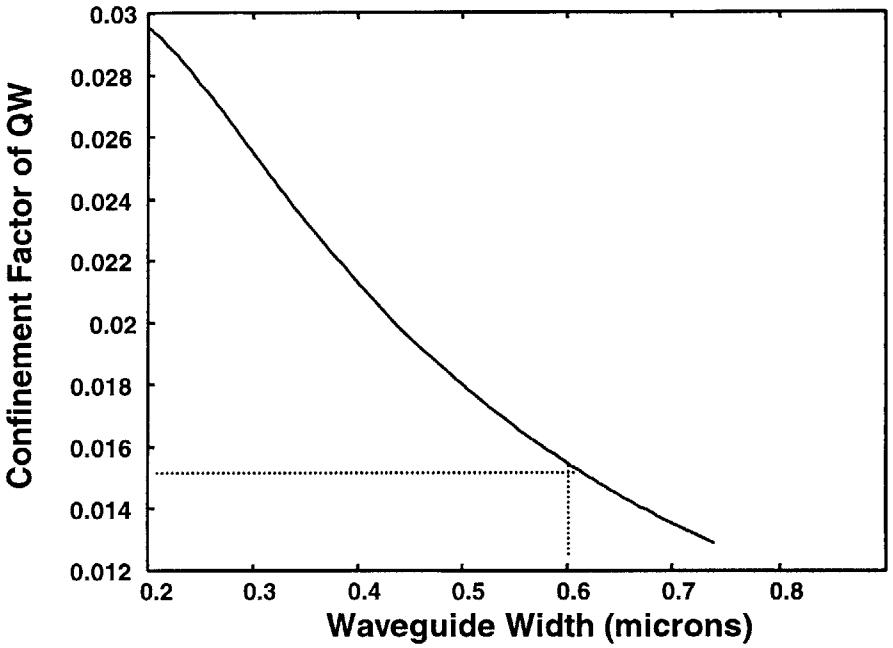

b)

Figure 3-22. The cladding confinement factor (a) and the quantum well confinement factor (b) versus waveguide width. Widening the waveguide from 0.22 μm to 0.6 μm reduces the overlap with the cladding by over a factor of four, while only reducing the overlap with the quantum well by less than a factor of 2.

All BCLs discussed so far have been gain guided devices. Gain guided devices suffer the disadvantage of being somewhat lossy for narrow stripes and, due to the index depression created by the injected carrier density, are slightly anti-guiding. Both of these effects lead to an increase in the threshold current. An alternative to the gain guided laser is the index guided laser. Index guided lasers are realized by implementing a lateral index contrast into the laser structure. This may be accomplished by etching a ridge, using a buried heterostructure geometry, or by using oxidation [35, 36]. Ridge etching, however, represents a poor choice in a BCL operating at a wavelength of 980 nm. The surface recombination velocity at an etched interface for InGaAs/GaAs is on the order of 10^5 cm/s. In narrow stripe devices this results in an appreciable increase in the threshold current. Single stage ridge waveguide lasers can be fabricated without etching through the active region but in the BCL the presence of the bottom gain stage necessitates etching through at least the top QW.

Buried heterostructures represent a viable method of achieving two dimensional waveguiding. Aside from representing a somewhat difficult technological challenge, they also fail to solve the problem of the lateral carrier diffusion-induced double threshold of the BCL. The oxidation of 90% Al mole fraction AlGaAs has been used in metalized AlGaAs-GaAs-InGaAs edge emitting layers to form current blocking apertures [33]. Oxide apertures not only confine current flow but they also provide a degree of index guiding as the index of refraction of the Al_xO_y is ~1.5-1.55. Even a thin layer of oxide provides some degree of lateral index confinement. Considering that both problems-the need for current confinement and index guiding-could be addressed simultaneously with oxidized current apertures it appears to be the method of choice. Furthermore, the oxidation procedure is believed to be compatible with the existing laser fabrication process.

The reduction in differential gain resulting from device heating has a pronounced effect on the relaxation oscillation frequency of the BCL as shown in Section 3.6. The use of broadened transverse optical waveguides and current apertures can be expected to reduce the optical loss and operating current for a given output power of the BCL. Reducing the optical loss and operating current obviously reduce the threshold carrier density, as less gain is needed to achieve lasing threshold. The logarithmic gain

approximation of Eqn. 3.1 yields a value of g_o/N for the differential gain. Clearly, reducing the threshold carrier density also then results in an increase in differential gain. Similary, as the relaxation oscillation is dependent upon the photon density in the cavity, less DC power must be used to achieve a given photon density; less DC power, less device heating.

Increasing the number of quantum wells is another method of improving differential gain. In a multiple quantum well device, the modal gain necessary to achieve threshold remains unchanged, being only a function of the optical and mirror losses, but the gain *per* quantum well is reduced, hence the differential gain is higher for *each* quantum well. The above described design improvements have been implemented in the second generation BCL shown in Fig. 3-23.

The second generation device structure was grown out of house. The lowermost and uppermost cladding layers were increased to a total thickness of 1 μm each, reducing radiation loss and ohmic loss respectively. The topmost cladding layer is divided into three sections with 0.6 μm of $Al_{0.4}Ga_{0.6}As$ residing above 0.2 μm of $Al_{0.94}Ga_{0.06}As$ below which lies another 0.2 μm of $Al_{0.4}Ga_{0.6}As$. The $Al_{0.94}Ga_{0.06}As$ serves as the oxidation layer. AlGaAs was chosen as the cladding material due to the inclusion of the oxidation layers. The aluminum oxide/InGaP interface has not been studied and it was considered too risky to attempt for the first time in a new device. The GaAs waveguides were extended to 0.3 μm on either side of a two quantum well active region. The QWs have a nominal composition of $In_{0.2}Ga_{0.8}As$ and are 80 Å wide with a single 80 Å GaAs barrier. The p-type cladding for the bottom gain stage has three separate sections consisting of 0.2 μm of $Al_{0.4}Ga_{0.6}As$ beneath 0.2 μm of $Al_{0.94}Ga_{0.06}As$ topped with 0.35 μm of $Al_{0.4}Ga_{0.6}As$. The 94% mole fraction AlGaAs again serves as the oxidation layer. The n-type cladding of the top gain section is 0.75 μm of $Al_{0.4}Ga_{0.6}As$. The doping for both n- and p-type cladding layers is 5×10^{17} cm^{-3} regardless of aluminum mole fraction. The tunnel junction is still doped in excess of 10^{19} cm^{-3} on both sides but it is now made of 10% In mole fraction InGaAs, thereby reducing the bandgap energy and increasing the tunneling probability.

The second generation BCL addresses all major shortcomings discovered in the first generation device. The expected result of the design improvements is improved

slope efficiency at reduced operation powers. The reduction in operating power will allow the cascading of more sections in any further design iterations. The ultimate goal of achieving link gain in a direct modulation (multimode) optical link will then be within grasp.

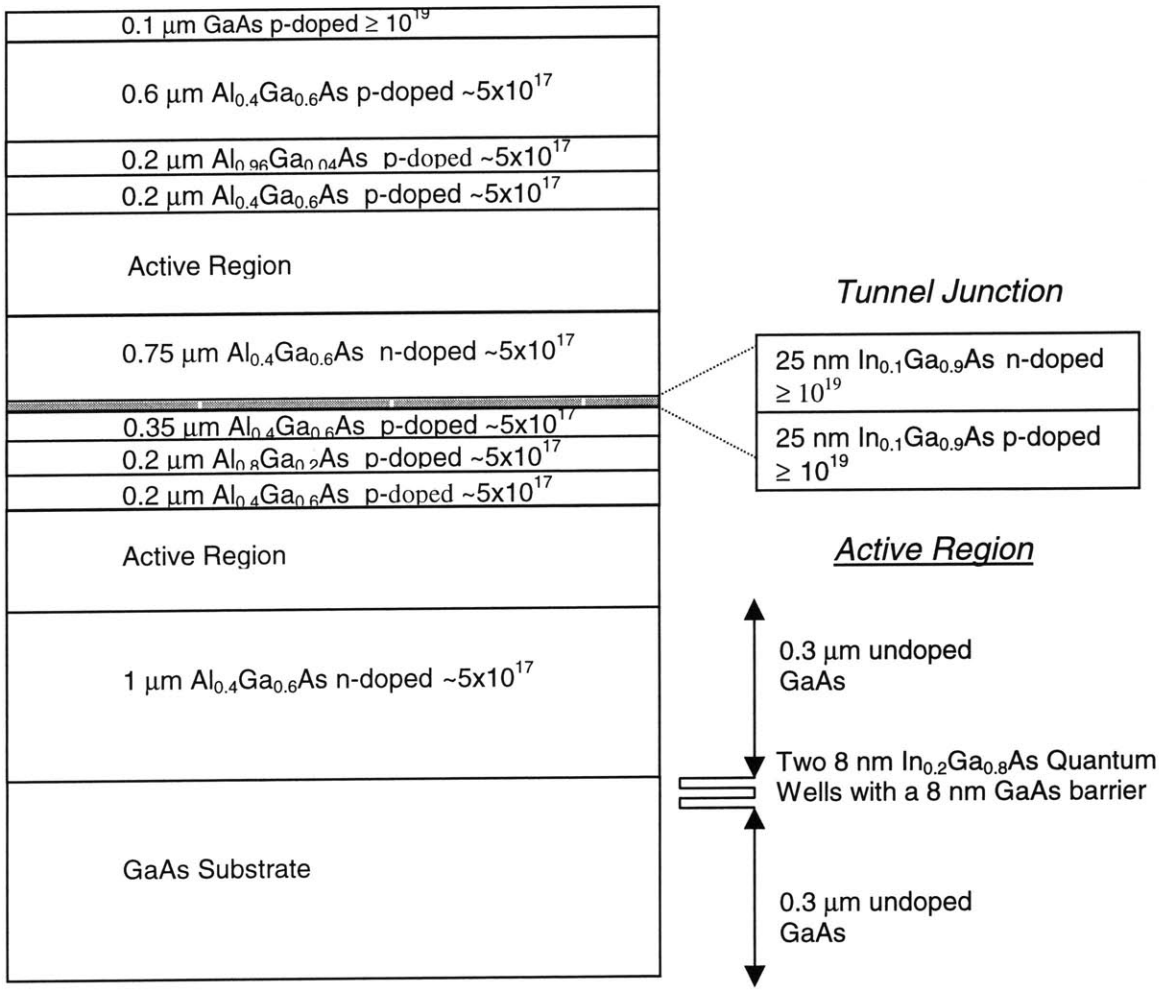

Figure 3-23. The second generation BCL design. The tunnel junction material is $In_{0.10}Ga_{0.9}As$ to reduce the bandgap and effective mass and decrease the junction resistance. The active regions use broadened waveguides to reduce optical loss and the threshold current. Two quantum wells are used in each gain stage to assuage temperature sensitivity. The upper cladding layers in each gain stage have a 0.2 μm thick $Al_{0.96}Ga_{0.04}As$ layer 0.2 μm above the edge of the waveguide. These layers may be laterally oxidized after doing a vertical etch through the device stack. The oxide layers serve a two-fold purpose. They provide current confinement so the top and bottom gain stages have equivalent injection areas and hence threshold currents. The oxide also provides index guiding for the optical mode.

3.8 Summary and conclusions

The first room temperature, continuous wave operation of a bipolar cascade laser was demonstrated. A record differential efficiency of 99.3% was shown. Modeling of the device showed good qualitative agreement with measurements of the light power and voltage versus bias current. Thermal modeling was performed and excellent agreement was found between finite element simulations of the device and direct measurements of the lasers surface temperature using a micro-thermocouple probe. The bias dependent relative intensity noise and spurious free dynamic range were measured. The reduction in the peak measured relaxation oscillation frequency of 1.5 GHz from the expected ~10 GHz is consistent with the thermal characteristics of the BCL. Non-ideal behavior was observed in some devices during the characterization process. A second generation device was designed to reduce the effects of the device's problems with thermal sensitivity, current spreading and gain-guiding.

The first and second generation devices use separate waveguides for each of the gain stages. The relative simplicity of this design allowed easier characterization and realization of fully functioning devices than would be possible with coupled waveguide or single waveguide devices. Coupling of the optical modes of the separate waveguide BCL into multimode fiber is a rather straightforward endeavor. In order to realize a device suitable for application in single-mode fiber links, a BCL with a coherent single fundamental mode optical field must be designed. The design of such a BCL is the topic of the next chapter.

References

[1] L. A. Coldren, S. W. Scott, "Diode Lasers and Photonic Integrated Circuits", John Wiley and Sons, Inc., 1995.

[2] S. L. Chuang, "Physics of Optoelectronic Devices", John Wiley and Sons, Inc., 1995.

[3] W. W. Chow, S. W. Koch, M, Sargent III, "Semiconductor-Laser Physics", Springer-Verlag Berlin Heidelberg, 1994.

[4] R. F. Kopf, E. F. Schubert, S. W. Downey, and A. B. Emerson, "N- and P-type, dopant profiles in distributed Bragg reflector structures and their effect on resistance", Appl. Phys. Lett., vol. 61, no. 15, 1820-1822, 1992.

[5] E. F. Schubert, G. H. Gilmer, R. F. Kopf, and H. S. Luftman, "Maximum concentration of impurities in semiconductors", Phys. Rev. B, vol. 46, no. 23, 78-84, 1992.

[6] R. L. S. Devine, C. T. Foxon, B. A. Joyce, J. B. Clegg, and J. P. Gowers, "Beryllium Diffusion Across GaAs/(Al,Ga)As Heterojunctions and GaAs/AlAs Superlattices During MBE Growth", Appl. Phys. A, vol. 44, 195-200, 1987.

[7] A. Gaymann, M Maier, W. Bronner, N. Grüen, and K. Khöler, "Beryllium diffusion in short-period $Al_xGa_{1-x}As$/AlAs-superlattices and vertically compact laser structures grown by molecular beam epitaxy", Mat. Sci. and Eng. B, vol. 44, 12-15, 1997.

[8] R. J. Malik, J. Nagle, M. Micovic, T. Harris, R. W. Ryan, and L. C. Hopkins, "Doping limits of C, Be, and Si in GaAs grown by solid source molecular-beam epitaxy with a thermally cracked As_2 source", J. Vac. Sci. Technol. B, vol. 10, no. 2, 850-853, 1992.

[9] T. Ijichi, M. Ohkubo, N. Matsumoto, and H. Okamato, "High power CW operation of aluminum-free InGaAs/GaAs/GaInP strained layer single quantum well ridge waveguide lasers", 12th IEEE Int. Semiconductor Laser Conf., 44-45, 1990.

[10] D. Z. Garbuzov, N. Y. Antonishkis, A. D. Bondarev, A. B. Gulakov, S. N. Zhigulin, N. I. Katsavets, A. V. Kocherin, and E. V. Rafaailov, "High-power 0.8 μm InGaAsP-GaAs SCH SQW lasers", IEEE J. Quantum Electron., vol. 27, no. 6, 1531-1536, 1991.

[11] D. Z. Garbuzov, N. Y. Antonishkis, S. N. Zhigulin, N. D. Il'inskaya, A. V. Kochergin, D. A. Lifshitz, E. U. Rafailov, and M. V. Fuksman, "High-power buried InGaAsP/GaAs (λ = 0.8 μm) laser diodes", Appl. Phys. Lett., vol. 62, no. 10, 1062-1064, 1993.

[12] M. R. Gokhale, J. C. Dries, P. V. Studenkov, S. R. Forrest, and D. Z. Garbuzov, "High-Power High-Efficiency 0.98-μm Wavelength InGaAs-(In)GaAs(P)-InGaP Broadened Waveguide Lasers Grown by Gas-Source Molecular Beam Epitaxy", IEEE J. Quantum Electron., vol. 33, no. 12, 2266-2276, 1997.

[13] J. F. Ahadian, P. T. Vaidyanathan, S. G. Patterson, Y. Royter, D. Mull, G. S. Petrich. W. D. Goodhue, S. Prasad, L. A. Kolodziejski, C. G. Fonstad Jr.' "Practical OEICs based on the monolithic integration of GaAs-InGaP LEDs with commercial GaAs VLSI electronics", IEEE J. Quantum Electron., vol. 34, no. 7, 1117-1123, 1998.

[14] N. Yamada, G. Ross, J. S. Harris Jr., "Threshold reduction in strained InGaAs single quantum well lasers by rapid thermal annealing", Appl. Phys. Lett., vol. 59, no. 9, 1040-1042, 1991.

[15] G. Zhang, J. Näppi, K. Vänttinen, H. Asonen, and M. Pessa, "Low threshold current InGaAs/GaAs/GaInP lasers grown by gas-source molecular beam epitaxy", Appl. Phys. Lett., vol. 61, no. 1, 96-98, 1992.

[16] J. M. Kuo, Y. K. Chen, M. C. Wu, and M. A. Chin, "InGaAs/GaAs/InGaP multiple-quantum-well lasers prepared by gas-source molecular beam epitaxy", Appl. Phys. Lett., vol. 59, no. 22, 2781-2783, 1991.

[17] M. Usami, Y. Matsushima, Y. Takahashi, "Gas source molecular beam epitaxy growth of GaAs/InGaP superlattice as optical confinement layers in 0.98 μm InGaAs/InGaP strained layer quantum well lasers", J. of Crystal Growth, vol. 150, 1344-1349, 1995.

[18] Y. K. Fukai, F. Hyuga, T. Nittono, K. Watanabe, H. Sugahara, "Improvement of InGaP/GaAs heterointerface quality by controilling AsH_3 flow conditions", Mat. Res. Soc. Symp., vol. 448, 21-24, 1997.

[19] O. Schuler, X. Wallert, and F. Mollot, "An experimental study of the relaxation behavior of strained $Ga_xIn_{1-x}P$ layers grown on GaAs", 10th Intern. Conf. On Indium Phosphide and Related Materials, 615-618, Tsukuba Japan, 1998.

[20] M. Yamada, "A theoretical analysis of self-sustained pulsation phenomena in narrow-stripe semiconductor lasers", IEEE J. Quantum Electron.,, vol. 29, no. 5, 1330-1336, 1993.

[21] C. R. Mirasso, G. H. M. van Tartwijk, E. Hernández-García, D. Lenstra, S. Lynch, P. Landais, P. Phelan, J. O'Gorman, M. San Miguel, and W. Elsäßer, "Self-Pulsating semiconductor lasers: Theory and experiment", IEEE J. Quantum Electron., vol. 35, no. 5, 764-770, 1999.

[22] J. Ch. Garcia, E. Rosencher, Ph. Collot, N. Laurent, J. L. Guyaux, B. Vinter, and J. Nagle, "Epitaxially stacked lasers with Esaki junctions: A bipolar cascade lasers", Appl. Phys. Lett., vol. 71, no. 26, 3752-3754, 1997.

[23] N. Laurent, D. Rondi, S. Leger, E. Rosencher, "Injection locking between laser layers in an InP-InGaAsP bipolar cascade laser", OSA Conf. on Lasers and Electro-Optics, Washington DC, vol. 6, 468-469, 1998.

[24] E. C. Vail, R. F. Nabiev, and C. J. Chang-Hasnain, "Temperature Dependence of Light-Current Characteristics of 0.98 μm Al-Free Strained-Quantum-Well Lasers", IEEE Photonics Tech. Lett., vol. 6, no. 11, 1303-1305 (1994).

[25] C. J. Chang-Hasnain, R. Bhat, H. Leblanc, and M. A. Koza, "Low threshold 0.98 μm aluminum-free strained-quantum-well InGaAs-InGaAsP-InGaP lasers", Elec. Lett., vol. 29, no. 1, 1-2 (1993).

[26] C. H. Cox III, H. V. Roussell, R. J. Ram, R. J. Helkey, "Broadband, directly modulated analog fiber link with positive intrinsic gain and reduced noise figure", International Topical Meeting on Microwave Photonics. Technical Digest, pp. 157-60. Piscataway, NJ, (1998).

[27] G. Zhang, J. Nappi, A. Ovtchinnikov, P. Savolainen, and H. Asonen, "0.98 μm strained layer GaInAs/GaInAsP/GaInP", Elec. Lett., vol. 28, no. 23, 2171-2172 (1992).

[28] C. Gmachl, A. M. Sargent, A. Tedicucci, F. Capasso, A. L. Hutchinson, D. L. Sivco, J. N. Baillargeon, S. N. G. Chu, and A. Y. Cho, "Improved CW operation of quantum cascade lasers with epitaxial-side heat-sinking", IEEE Phot. Tech. Lett., vol. 11, no. 11, 1369-1371, 1999.

[29] K. J. Beernink, J. J. Alwan, and J. J. Coleman, "Antiguiding in narrow stripe gain-guided InGaAs-GaAs strained-layer lasers", J. Appl. Phys., vol. 69, no. 1, 56-60, 1991.

[30] W. W. Chow, G. C. Dente, and D. Depatie, "Saturation effects in semiconductor lasers", IEEE J. Quantum Electron., vol. 23, no. 8, 1314-1320, 1987.

[31] R. Nagarajan, M. Ishikawa, T. Fukushima, R. S. Geels, and J. E. Bowers, "High speed quantum-well lasers and carrier transport effects", IEEE J. of Quantum Electron., vol. 28, no. 10, 1990-2008, 1992.

[32] H. L. T. Lee, R. V. Dalal, R. J. Ram, K. D. Choquette, "Dynamic range of vertical cavity surface emitting lasers in multimode links", IEEE Photon. Tech. Lett., vol. 11, no. 11, 1473-1475, 1999.

[33] S. A. Maranowski, E. I. Chen, N. Holonyak, Jr. and T. A. Richard, "$Al_xGa_{1-x}As$-GaAs-$In_yGa_{1-y}As$ quantum well heterostructure lasers with native oxide current-blocking windows formed on metallized devices", Appl. Phys. Lett., vol. 64, no. 16, 2151-2153, 1994.

[34] S. A. Maranowski, A. R. Sugg, E. I. Chen, and H. Holonyak, Jr., "Native oxide top- and bottom-confined narrow stripe p-n $Al_yGa_{1-y}As$-$In_xGa_{1-x}As$ quantum well heterostructure laser", Appl. Phys. Lett., vol. 63, no. 12, 1660-1662, 1993.

[35] S. J. Carraci, M. R. Krames, M. J. Ludowise, A. Fischer-Colbrie, and N. Holonyak, Jr., "Long wavelength (l~1.5 mm) native-oxide-defined InAlAs-InP-InGaAsP quantum well heterostructure laser diodes", J. Appl. Phys., vol. 75, no. 5, 2706-2708, 1994.

[36] T. A. Richard, F. A. Kish, N. Holonyak, Jr., J. M. Dallesasse, K. C. Hseih, M. J. Ries, P. Gavrilovic, K. Meehan, and J. E. Williams, "Native-oxide coupled-stripe $Al_yGa_{1-y}As$-$In_xGa_{1-x}As$ quantum well heterostructure lasers", Appl. Phys. Lett., vol. 58, no. 21, 2390-2392, 1991.

Chapter 4: Antiresonant reflecting optical waveguide bipolar cascade lasers

4.0 Introduction

The second generation BCL, which was the subject of the final section of the last chapter, addressed many of the shortcomings of the first RT, CW BCL. The reduction in optical loss and the inclusion of current confinement and an index guiding structure are expected to substantially improve the slope efficiency and the relaxation oscillation frequency of the device. The multiple waveguide device designs of the first and second generation BCLs represent one possible implementation of the bipolar cascade concept. The multiple waveguide design sidesteps the issue of optical absorption loss in the tunnel junctions by well separating the optical fields. This configuration works well for most purposes to include multimode optical fiber links. The optical output of the separate waveguide structure of the BCL, while coupling efficiently into multimode fiber, cannot be efficiently coupled into single mode fiber. Multimode fiber has a large numerical aperture and a core diameter of 50-60 μm. Singlemode fiber has a core diameter of only 5-6 μm and the farfield generated by the separate waveguides of the BCL is not the fundamental (or any other) eigenmode of the fiber. In order to obtain efficient coupling into single mode fiber it is necessary to phase lock the optical fields generated by the separate gain stages together to produce a coherent output beam.

This chapter addresses the issues associated with realizing a BCL which efficiently couples into single mode fiber. Section 4.1 details the problems of achieving the necessary near field characteristics needed to achieve a farfield with a narrow angle, coherent output beam. Several design alternatives are considered qualitatively and the associated problems and advantages are highlighted. Section 4.2 quantitatively describes and models the antiresonant reflecting optical waveguide (ARROW) BCL. The device calculations of this chapter are for lasers emitting at 1.55 μm. This represents the wavelength at which optical fiber has minimum dispersion and is, hence, of great technological importance.

4.1 The optical fiber coupling problem

The seemingly most straightforward approach to the problem of generating a single coherent output beam for efficient single mode fiber coupling is to place all the gain stages and tunnel junctions inside of a single waveguide as shown in Fig. 4-1. If the fundamental mode propagates in such a structure the overlap of the optical field with the highly doped tunnel regions is quite large, however. While leading to large absorption loss in any laser, this is a matter of considerable concern in InP based systems where intravalence band absorption of p-doped material is approximately 35 cm^{-1} per 10^{18} cm^{-3} of doping. The mode which preferentially propagates is the one that maximizes Γ (defined as the overlap of the optical field with the quantum wells) and/or minimizes loss. The second order mode shown in Fig. 4-1 is the lowest order field profile both maximizing Γ and minimizing optical absorption loss due to the tunnel junctions. While this is a coherent optical field shared by all the gain stages, the farfield pattern would not efficiently couple into single mode fiber, as an on-axis null exists (Fig. 4-2). This design was tried by Kim et al. [1], but only achieved pulsed operation.

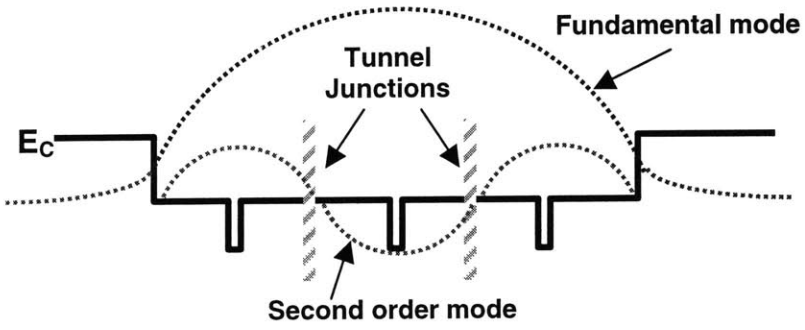

Figure 4-1. The near field profile of a single waveguide BCL. The large overlap of the fundamental mode optical field with the highly doped tunnel junctions forces the device to lase in the 2nd order mode so that the optical field has nulls at the tunnel junctions.

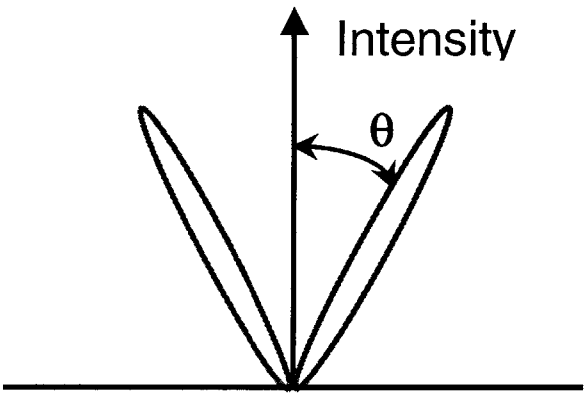

Figure 4-2. The farfield pattern generated by the 2nd order mode. The on-axis null results from the anti-phase center peak.

Returning to the design of the original BCLs, another possible solution involves moving the separate waveguides closer together so the gain stages may injection lock. This has been demonstrated by Laurent, et al. [2], but the loss introduced by the tunnel junction resulting from the increased field overlap with the tunnel junctions was calculated to be 40 cm^{-1}. This device was also operated only pulsed. A further complication of this geometry is that symmetry of the preferential *lasing* mode is odd. The fundamental guided mode of the evanescently coupled waveguides is even, but Γ is maximized (and optical absorption loss minimized) for the odd mode of Fig. 4-3. Once again, coherent optical field coupling can be achieved but with the same problem of an on-axis null in the farfield.

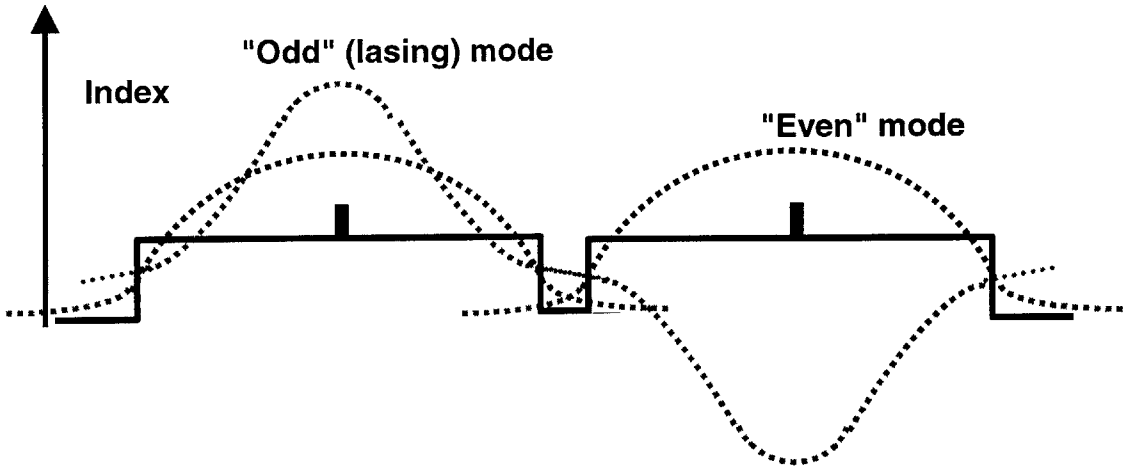

Figure 4-3. Moving two guided mode lasers closer together such that they evanescently couple forces the odd mode to lase. The far field of this profile would have an on-axis null as in Fig. 4-2.

Now consider the following. Fig. 4-4 shows a waveguide/device with the gain regions (QWs) placed within the *low* index regions and clad with high index material. There is no angle of incidence for a wave going from a low index material to a high index material for which the field is totally internally reflected. Obviously such a configuration cannot carry a truly guided mode. In the design of Fig. 4-4 any of the light incident upon the low to high index interface is rejected rather than guided, leading to the nomenclature of an "antiguiding" structure. Of course, if the index contrast is large, or the angle of incidence high, then very little of the mode radiates in the adjacent region.

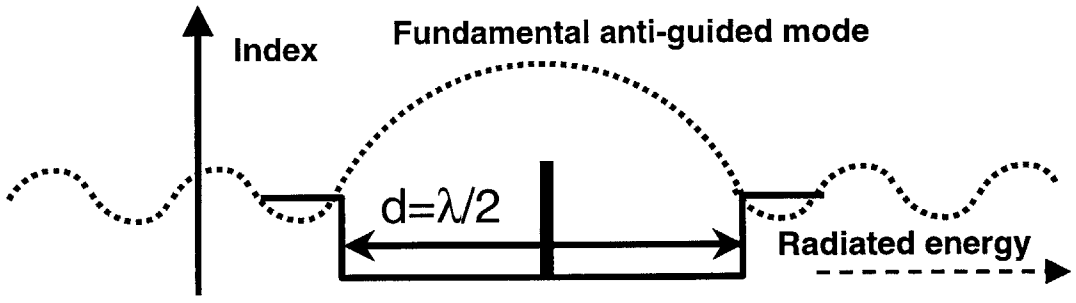

Figure 4-4. The near field optical mode of an anti-guiding structure. Energy leaks from either side as total internal reflection is not possible for a wave incident upon a higher index material.

There are two conditions for achieving resonance in a passive guided wave structure. First, the wave must be equal to its starting magnitude upon making a round trip between the two interfaces of the waveguide. Second, the phase must remain unchanged, modulo 2π. While the loss at the two interfaces in an antiguided structure precludes having the wave retain its magnitude upon making a full round trip, the round trip phase condition can be met. The antiguide can be made to resonate in some sense by making its width $\lambda/2$ of a transverse wavelength, as shown in Fig. 4-4. A mode that is antiguided but meets the round trip phase condition is said to be a "quasi-mode" or a "leaky mode".

It is also possible to couple quasi-modes together. Fig. 4-5 shows two antiguiding structures separated by a high index spacer region. If the transverse dimension of the spacer region is also chosen such that it is a half wavelength wide in the high index material then the optical field in the spacer is resonant as well. In other words, in making a full round trip of the device the field once again replicates its phase (modulo 2π). The optical field in the spacer is antiphase to that in the low index gain regions or core regions, as they will be referred to from here forward. If the antiguide is designed properly, the intensity of the optical field in the spacer is only a fraction of the intensity of the optical field in the cores. The fundamental point to be realized here is that the optical fields of the gain regions are coupled *coherently*. The resultant far field pattern is presented in Fig. 4-5. Most of the power in the far field resides in a single narrow beam. Some energy appears in the side lobes but, if designed properly, it can be quite small.

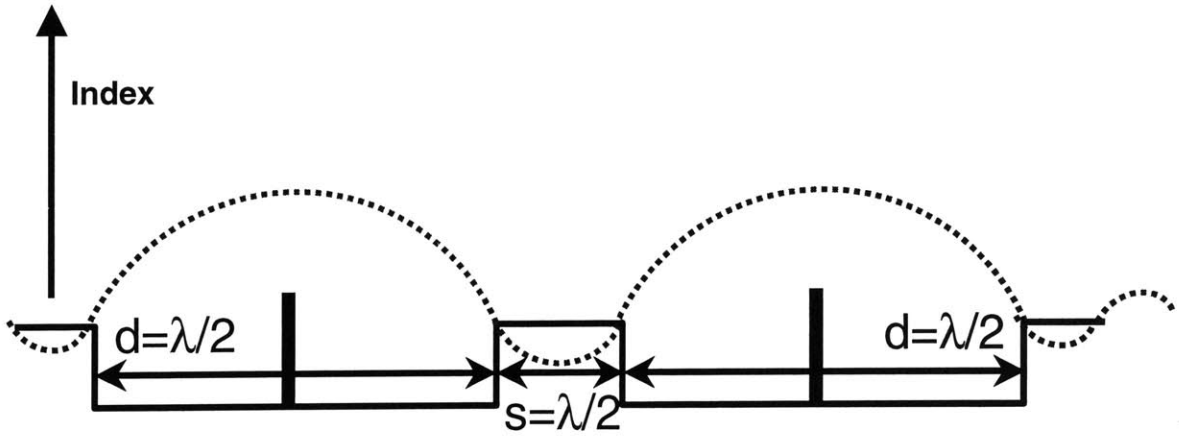

Figure 4-5. Two antiguiding structures coupled via a high index section. Each section is a half wavelength wide in the lateral direction. Such a structure is functionally equivalent to a series of resonant Fabry-Perot filters. The greater the number of sections, the smaller the radiation loss.

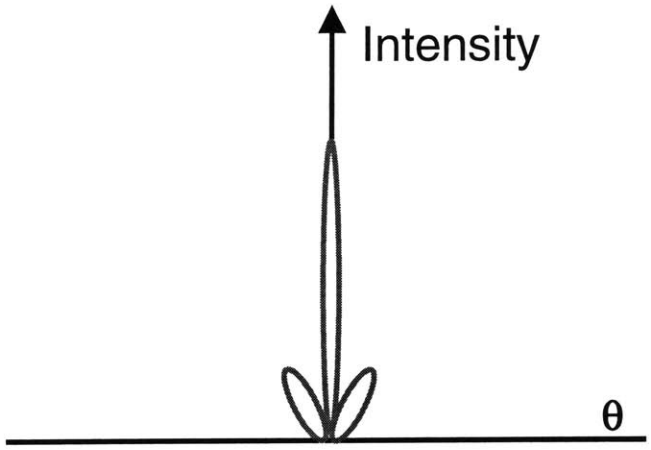

Figure 4-6. The farfield intensity pattern that would be generated by the near field pattern of Fig. 4-5.

A matter of no small concern is the reduction of lateral radiation loss from the edges of the antiguiding structure. The maximum index contrast which is available is material system dependent and can be expected to be in the range ≈ 0.1-0.3 for most semiconductors. There is also a design limit as to how wide the core regions may be made, which will be addressed quantitatively in the next section. Distributed Bragg reflectors (DBRs) represent a method of increasing the effective reflectivity for the outermost core regions. The inclusion of properly dimensioned DBRs with the previously described multisection antiguiding structure is termed an anti-resonant

reflecting optical waveguide (ARROW). The design of the ARROW structure, and its incorporation with a bipolar cascade laser, is the subject of the next section.

4.2 The antiresonant reflecting optical waveguide bipolar cascade laser

The qualitative understanding of ARROW structures garnered in the previous section hint toward their application to BCLs. Obviously, the far field characteristics described in Section 4.1 permit for efficient coupling into single mode fiber. The relationship between ARROW designs and the far field patterns they generate requires quantitative exploration. Quantitatively describing this relationship, as well as other issues such as loss minimization, threshold current calculations, and design trade-offs are the purpose of this section.

ARROW waveguide lasers have been extensively investigated for high power applications [3,4,5]. In these devices the active regions are electrically coupled in *parallel* and the ARROW is implemented in the lateral direction (normal to the growth direction). In the ARROW-BCL the active regions are electrically coupled in *series* and the waveguide is implemented in the vertical (epitaxial growth or transverse) direction. Implementing the ARROW via epitaxial growth allows the precise control of dimensions and optical indices afforded by modern epitaxial technology.

To ensure maximum coupling between the core regions, both the core regions and spacers must be dimensioned such that their widths are equal to a multiple of a vertical (or transverse) half-wavelength, designated λ_1 in the high index regions and λ_0 in the low index regions. Stated another way, the product of the z-component (where the z-direction is taken to be the same as the growth direction as shown in Fig. 4-7) of the k-vector and the height of the core (or spacer) region must be equal to an integer multiple of π. This in essence makes the core and spacer regions equivalent to a stack of resonant Fabry-Perot cavities. The dispersion relationship relating the lateral dimensions of the spacers and cores, the optical indices and the wavelength of operation is:

$$\left(\frac{1}{s^2}\right)-\left(\frac{1}{d^2}\right)=\frac{4\left(n_1^2-n_o^2\right)}{\lambda^2} \tag{4.1}$$

where s is the spacer width, d is the core width, n_1 is the index of the higher index material, n_o is the index of the lower index material and λ is the freespace wavelength.

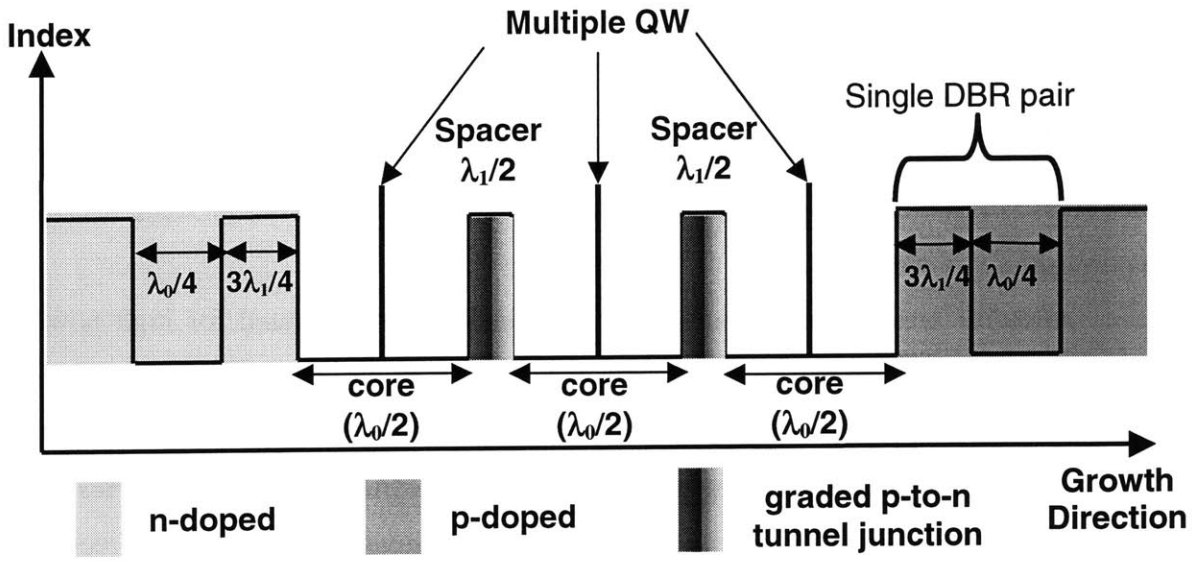

Figure 4-7. The concept of an antiresonant reflecting optical waveguide bipolar cascade laser. The tunnel junctions are placed in the high index core regions. The junction may be placed anywhere in the high index region to control loss and higher order modes. The cladding to either side of the core regions consists of a single distributed Bragg reflector pair.

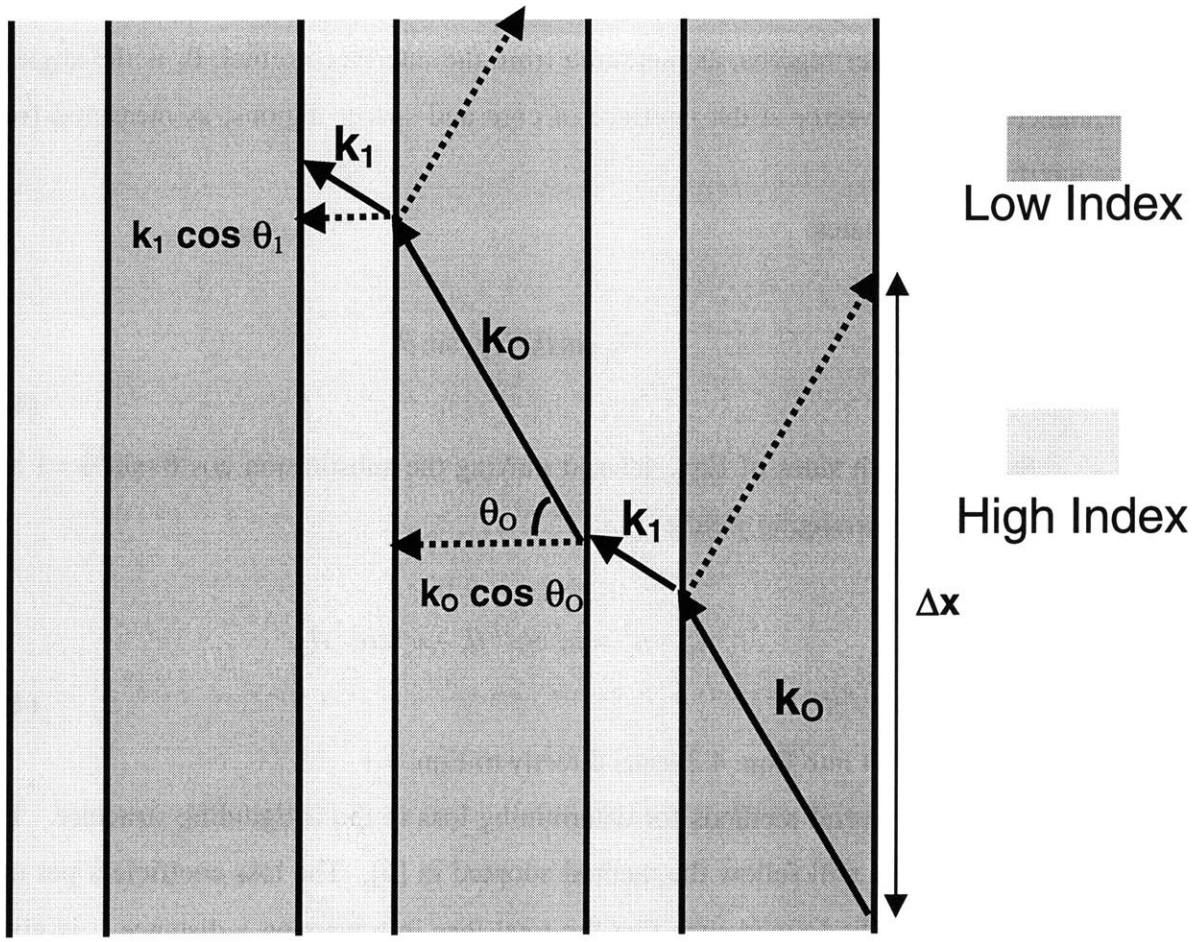

Figure 4-8. A top down view of the antiguide. The layer widths are chosen such that the lateral component of the k-vector times the layer width is equal to a multiple of π.

In order to derive Eqn. 4.1, the previously described resonance conditions for the spacer and core regions are quantified as:

$$k_{zo} = k_o \cos\theta_o = \frac{\pi}{d} \tag{4.2a}$$

$$k_{z1} = k_1 \cos\theta_1 = \frac{\pi}{s} \tag{4.2b}$$

where k_{zo} and k_{z1} are the component of the k-vectors in the vertical/transverse direction in the low and high index regions, respectively, and k_o and k_1 are the magnitudes of the k-vectors in the same regions. θ_o is the angle of incidence of the k_o-vector at the interface

of the core and spacer regions, as measured from the interface normal. θ_1 is the angle of incidence of the k_1-vector at the interface of core and spacer regions, as measured from the interface normal.

Snell's law states:

$$n_1 \sin\theta_1 = n_o \sin\theta_o \tag{4.3}$$

Squaring both sides of Eqn. 4.3 and making the substitution $\cos^2\theta+\sin^2\theta = 1$ and performing some rearranging yields:

$$n_1^2 - n_o^2 = n_1^2 \cos^2\theta_1 - n_o^2 \cos^2\theta_o \tag{4.4}$$

Substituting Eqn. 4.4 into Eqn. 4.2 leads directly to Eqn. 4.1.

There are several methods for determining loss in the antiguiding structure. The approach taken here will follow the method adopted in [6]. The loss coefficient per unit length, α, is normally defined such that the total loss in traversing a distance L is given by:

$$\frac{P(L)}{P(0)} = e^{-\alpha L} \tag{4.5}$$

where P(x) is the power in the wave at point x.

Taking a ray optics approach, consider a ray incident upon the boundary of two materials of differing optical index. A percentage T of the incident power will be transmitted at the interface, where T is the power transmission coefficient at the interface. The ray will then bounce and travel a distance Δx before bouncing again upon the same interface (Fig. 4-8). The power remaining in the wave after one bounce is then equal to:

$$P(\Delta x) = P(0)(1-T) = P(0)R \tag{4.6}$$

where R is the power reflectivity at the interface.

In traversing the length of the device assume the ray bounces M times at one of the interfaces, or a total of 2M times if both interfaces are included. Eqns. 4.6 and 4.7 then combine to give:

$$R^{2M} = e^{-\alpha L} \tag{4.7}$$

From basic geometric considerations the distance Δx between bounces is just $2 \cdot d \cdot \tan\theta$. M may therefore be set equal to $L/(2 \cdot d \cdot \tan\theta)$ where θ is the angle of incidence of the field upon the core/DBR interface as measured from the core/DBR interface normal. Solving for α in Eqn. 4.7, then applying Snell's law and Eqn. 4.1 gives:

$$\alpha = -\frac{\lambda \times \ln(R)}{n_o d^2 \sqrt{1 - \left(\frac{\lambda}{2 n_o d}\right)^2}} \tag{4.8}$$

Eqn. 4.8 agrees well with published data for laterally coupled ARROW laser structures [4]. Minimization of the radiation loss dictates a glancing angle of incidence between the optical field and the interfaces between the cores and spacers. This criterion is met by using wide core regions; typically up to several microns depending upon emission wavelength and index contrast (Fig. 4-9). Widening the core regions also places more of the total optical field into the core regions (as opposed to the spacer regions). This is desirable in that when the ARROW is on resonance the optical field in the spacers is anti-phase with respect to the optical field in the core. Large fields in the spacers hence broaden and diminish the total power contained in the far field main lobe, thereby diminishing the possibility for efficient coupling into single mode optical fiber. The larger the index contrast between the high and low index regions the greater the total percentage of the optical field which resides in the core regions for a given *d/s* ratio. Large index contrasts also serve to reduce optical radiation loss. It can be rigorously shown that if the number of core elements in the ARROW is *N*, then the loss is equal to α/N [7]. A more physically appealing explanation arises by realizing that at resonance

the spacer regions are transparent to the optical field making the core region appear to be N·d wide. This reduces the number of bounces a ray undergoes in traversing the structure by N. Since each additional core region adds a diode drop to the voltage across the structure there is a physical limit to the number of core regions that may be placed in the structure as set by the ability to effectively heatsink the structure [8].

The inclusion of the DBR pair also has the benefit of equalizing the optical field intensity value in the anti-guiding cores. Note that the high index section of the DBR is chosen to be (2m+1)/4 of a vertical (transverse) wavelength (see Fig. 4-7) as this ensures the optical field in the outermost (low index) section of the DBR is in-phase with the optical field in the core regions [3,4,5]. Such an arrangement does not, however, provide the lossless field confinement found in traditional edge emitting lasers where the active regions reside in the high index (guiding) section of the waveguide. For the ARROW structure to provide an acceptably low level of radiation loss several design criteria must therefore be met.

Fig. 4-9 shows the calculated near field pattern for a three-core ARROW waveguide of 2.75 μm corewidth and n_o of 3.17 and n_1 of 3.40. Note that very little of the total field intensity exists in the spacer regions. This is readily understood from the previous derivation of the optical loss per unit length due to leakage. The angle of incidence in the high index spacer is smaller than in the low index core. This implies that the leakage of power from the spacer to the core is greater than from the core to the spacer.

Aside from the advantages realized in the far field as previously described, the small field intensity present in the spacer regions allows the highly doped tunnel junctions to be placed in them (see Fig. 4-10) without suffering large optical absorption loss. Further, the center of the tunnel junction, the only section that needs to be highly doped, may be placed away from the center of the spacer anti-node. The far field pattern of the device of Fig. 4-9 is shown in Fig. 4-10. The full-width at half-maximum for this device is 4.8 degrees while 60% percent of the total output power is contained in the main lobe. This device is calculated to have a 140% fiber coupled modulation efficiency assuming uncoated facets. This value was calculated for a three-core cleaved facet

device of 88% slope efficiency per core and 88% coupling efficiency into the fiber (i.e. 3×88%×88%×60%=140%).

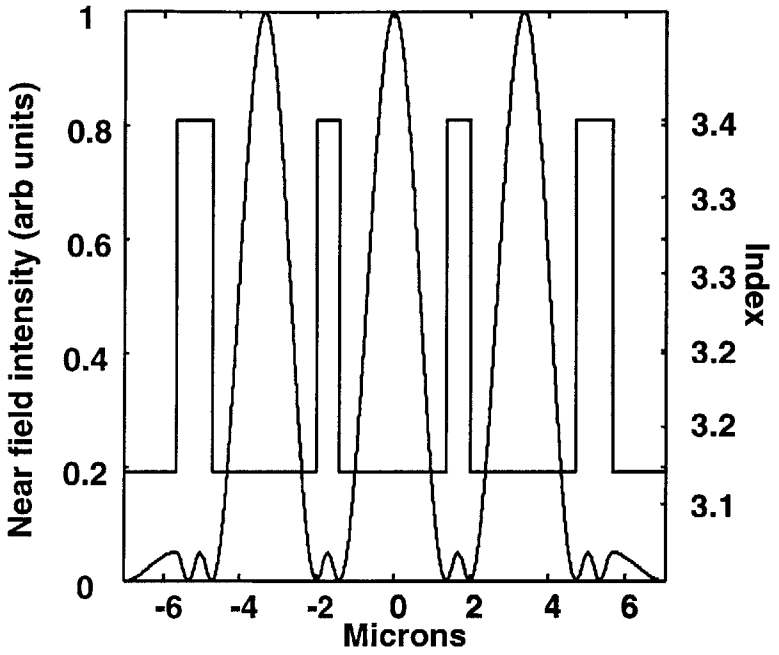

Figure 4-9. Nearfield optical field intensity for a three-core ARROW-BCL. Over 96% of the field intensity resides in the cores, while only 0.7% exists in the highly doped spacer regions.

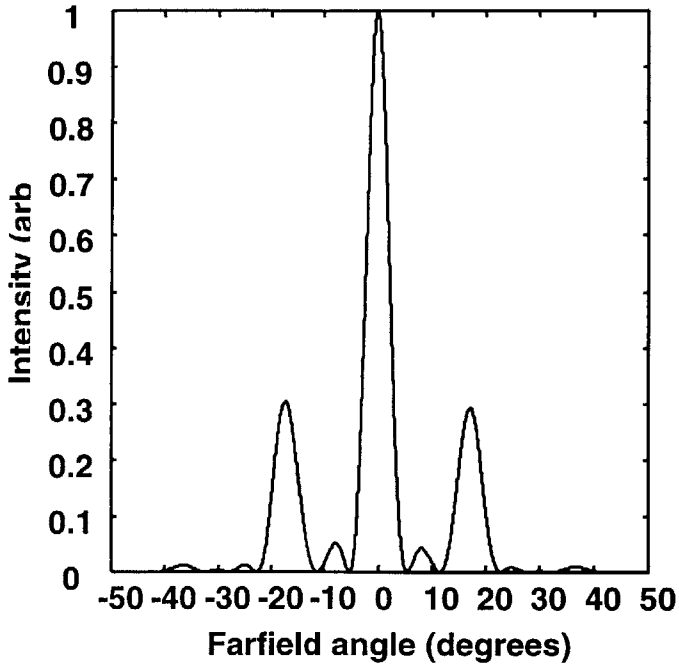

Fig. 4-10. Farfield intensity pattern for the device of Fig. 4-3. 60% of the total power resides in the main lobe. The main lobe has a full-width at half-maximum of 4.8 degrees.

Fig. 4-11 shows the field overlap with the highly doped spacer regions and the total absorption loss in the three core ARROW BCL. The tunnel junctions are assumed to be only 10 nm in extent and to reside at the very edge of the spacers. It is quite clear that very little of the total optical field intensity is located in the spacers. Fig. 4-11 shows the total absorption loss in the device. The DBR pairs to either side of the structure and the spacers are all assumed doped at 5×10^{17} (with the exception of the rather small regions occupied by the tunnel junctions). Even though the absorption loss in the p-doped region is 35 cm^{-1} per 10^{18} of doping the total absorption loss in the device is well below the radiation losses. The origin of the large threshold current densities is the rather poor QW confinement factor.

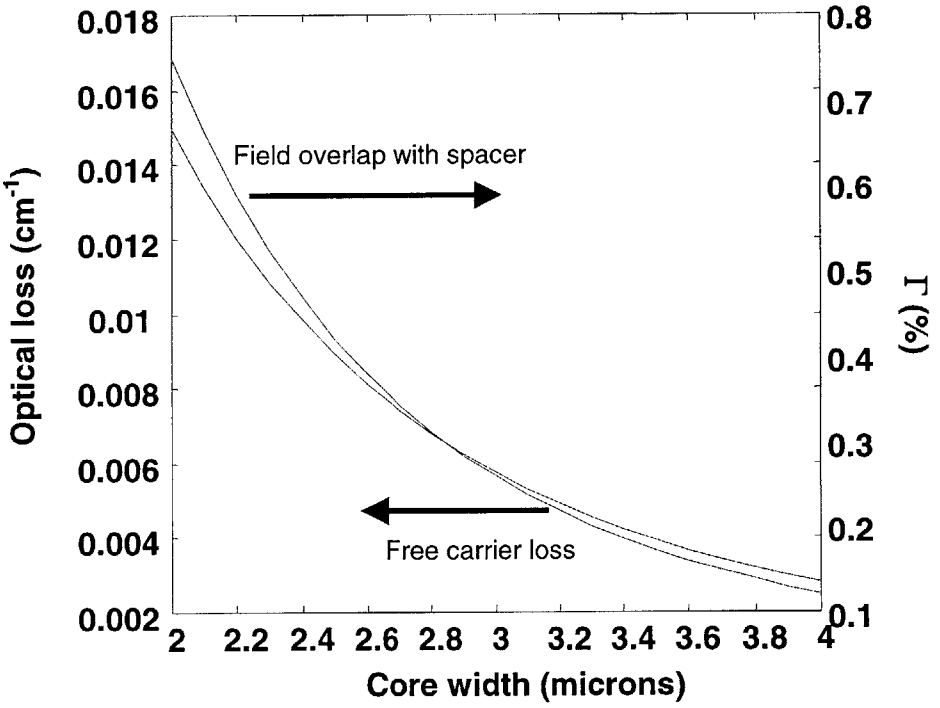

Figure 4-11. Free carrier absorption loss in the DBRs and spacers (left ordinate) and the optical field intensity overlap with the spacer regions in a three-core ARROW-BCL. The device parameters are as given in Table 4.1. Note that very little of the optical field intensity resides in the spacers.

While increasing the core width has advantages with respect to minimizing radiation losses and achieving desirable far field characteristics, increasing the core width also reduces the optical confinement factor (Γ) with the active area (assuming a fixed number of QW). Since the threshold current density is exponentially dependent upon both Γ and the total optical loss, a design tradeoff exists between optimizing the far field characteristics of the ARROW BCL and minimizing the threshold current density. Fig. 4-13 shows that a clear minimum exists for the threshold current density versus core width in the given material system. The threshold current density is calculated using the following [9]:

$$J_{th} = \frac{qN_w wBN_{tr}^2}{\eta_i} e^{\left(\frac{2(\alpha_i+\alpha_m+\alpha_R)}{\Gamma g_o}\right)} + \frac{qN_w wCN_{tr}^3}{\eta_i} e^{\left(\frac{2(\alpha_i+\alpha_m+\alpha_R)}{\Gamma g_o}\right)} \tag{4.9}$$

where q is the electron charge, N_w is the number of quantum wells, w is the quantum well width, N_{tr} is the transparency carrier density, η_i is the injection efficiency, B is the bimolecular recombination coefficient, C is the Auger recombination coefficient, α_i is the internal optical field loss per unit length, α_m is the mirror loss per unit length, α_R is the radiation loss per unit length, Γ is the quantum well confinement factor, and g_o is the gain coefficient. At an emission wavelength of 1.55 μm the second term in Eqn. 4.9 is a significant contribution to the threshold current.

Fig. 4-12 shows the threshold current density as the number of quantum wells is increased from 5 to 10 to 15 wells. The core width at which the minimum threshold current is achieved is a rather weak function of the number of QWs. Increasing the number of wells to 10 from 5 shows two positive trends. The minimum threshold current density is reduced substantially, and the curve flattens. The latter is advantageous in that wider core regions increase the total percentage of optical power in the main lobe and reduce the full-width at half-maximum. Increasing the number of wells to 15 from 10 increases the threshold current density with the exception of very wide core regions.

Table 4.1 lists the values used in calculating the results of Fig. 4-9-12. Using a core width of 2.25 μm reduces the percentage of emitted optical power in the main lobe to 56% as well as reducing the fiber coupled modulation efficiency to 130%.

There is an additional advantage to narrower cores; transport effects across the very broad cores greatly reduce the laser's modulation bandwidth. Transport effects can be mitigated by using doped cores, albeit at the expense of greatly increased optical absorption loss. An alternate approach would be to further diminish the core width, but to increase the number of DBR pairs. The latter has the disadvantage of markedly increasing the stack height and series resistance of the device. It is also limited in applicability as the radiation loss versus core width is a strongly nonlinear function.

There is usually an inverse relationship between bandgap energy and optical index of refraction. Hence, a lower index material will typically have a larger bandgap than a higher index material. The placement of the quantum wells in the low index regions of the waveguide therefore heightens the barrier potential for the bound electrons and holes captured in the wells. The thermal sensitivity of the active region diminishes accordingly as the quasi-Fermi levels may penetrate more deeply into the wells before the carriers are likely to escape. It has been shown in [10] that deepened wells also reduce both the carrier capture time and the carrier capture time to carrier escape time ratio. A short capture time is important as placing the quantum wells in the high bandgap (low index) regions removes the double heterostructure normally present in most diode lasers. A large carrier capture to carrier escape ratio (which can approach or exceed a value of one for some lasers under typical operating conditions) heightens gain compression and dampens the frequency response of the laser [10,11]. The deepened quantum wells can therefore be expected to improve the BCL's resonance frequency over a broad operating range. Appendix D presents a design for a single-stage (noncascaded) vertical ARROW laser. Such a device would provide proof of concept for the vertical ARROW to be implemented as an ARROW-BCL.

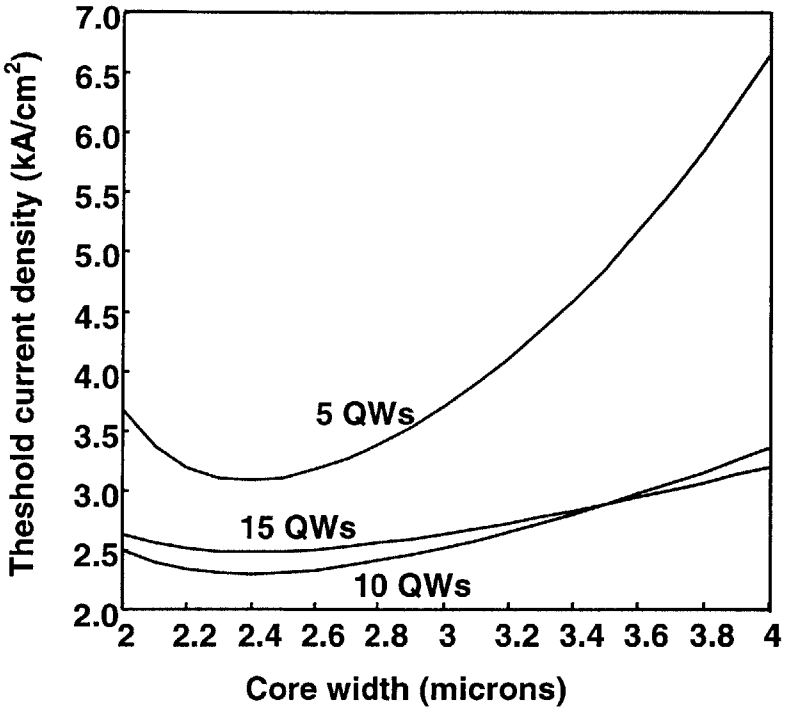

Figure 4-12. Threshold current density versus core width for 5, 10 and 15 quantum wells per core for a three-core ARROW-BCL. Note for that for 10 and 15 quantum wells the threshold current density sensitivity to core width is rather small. This permits a reasonable design trade-off between farfield characteristics and threshold current.

Parameter	*Value*	*Units*
n_o	3.17	dimensionless
n_I	3.40	dimensionless
Number of QW	5	dimensionless
B (spontaneous emission)	0.22×10^{-10}	cm^3/sec
C (Auger recombination)	9×10^{-29}	cm^6/sec
N_{tr} (transparency carrier dens)	1.82×10^{18}	$1/cm^3$
η_I (injection efficiency)	0.80	dimensionless
L (device length)	500	μm
R (facet reflectivity)	0.32	dimensionless
n & p doping density	5×10^{17}	$1/cm^3$

Table 4.1

Only two concerns arise when considering the ARROW-BCL. The device height can be even greater than for vertical cavity surface emitting lasers (VCSELs); possibly as large as 15 μm in lasers emitting at 1.55 μm. The extended times needed to grow such tall epitaxial layers could exceed the ability of the growth technology to maintain growth rates and optical index values over the course of the growth, particularly for the quarternary layers. It is encouraging that the distributed Bragg reflectors in VCSELs and superlattices, each of which require exacting standards in dimensions and compositional alloying, have been grown with excellent results. Of greater concern is the impact the very broad core regions will have on the frequency response of the ARROW-BCL. The transport time associated with traversing half the core width to the active region can be mitigated by doping the cores but with a concomitant increase in optical loss.

Overcoming this final difficulty will require careful balancing of several design parameters.

4.3 Summary and conclusions

This chapter has presented the design and modeling of a new type of bipolar cascade employing an antiresonant reflecting optical waveguide to achieve coherent single mode performance from the device. Calculations of the absorption and radiation losses as well as threshold current were presented for a three-core device operating at an emission wavelength of 1.55 μm. The device was found to benefit from using an active area containing ten quantum wells. Farfield calculations indicate 64% of the output power can be put in the main lobe of the device with a full-width at half-maximum of 4.8 degrees. The spacer regions contain very little of the optical field intensity allowing the highly doped tunnel regions to be placed within them while minimally increasing the absorption loss of the device. Adjusting the placement of the tunnel in the spacer regions allows a degree of control over the amount of absorption loss that may be introduced. The waveguide structure optically couples the separate active regions coherently producing a narrow angle optical beam suitable for coupling into single mode fiber. The use of multiple active regions, wide core regions, and the relatively large index contrasts available in most semiconductor material systems allow the device designer to greatly reduce the radiation loss from the ARROW structure. A single stage laser was designed to provide proof of concept of the vertical ARROW laser.

References:

[1] J. K. Kim, E. Hall, O. Sjolund, L. A. Coldren, "Epitaxially-stacked multiple-active-region 1.55 μm lasers for increased differential efficiency", App. Phys. Lett., vol. 74, 3251-3, 1999.

[2] N. Laurent, D. Rondi, S. Leger, E. Rosencher, "Injection locking between laser layers in an InP-InGaAsP bipolar cascade laser", OSA Conf. on Lasers and Electro-Optics, Washington DC, vol. 6, 468-469, 1998.

[3] C. Zmudzinski, D. Botez, L. J. Mawst, A. Bhattacharya, M. Nesnidal, R. F. Nabiev, "Three-core ARROW-Type diode laser: Novel high-power, single-mode device, and effective master oscillator for flared antiguided MOPA's", Journ. Select. Topics in Quant. Elec., vol. 1, no. 2, 129-137, 1995.

[4] L. J. Mawst, D. Botez, C. Zmudzinski, and C. Tu, "Antiresonant reflecting optical waveguide-type, single-mode diode lasers", Appl. Phys. Lett., vol. 61, no. 5, 503-505, 1992.

[5] L. J. Mawst, D. Botez, C. Zmudzinski, and C. Tu, "Design optimization of ARROW-type diode lasers", IEEE Phot. Tech. Lett., vol. 4, no. 11, 1204-1206, 1992.

[6] A. Yariv, P. Yeh, "Optical waves in crystals", John Wiley and Sons, Inc., 1984.

[7] D. Botez, A. P. Napartovich, "Phase-locked arrays of anitguides: Analytical theory", IEEE Journ. of Quant. Electron., vol. 30, no. 4, 975-980, 1994.

[8] S. G. Patterson, E. Lau, K. P. Pipe, R. J. Ram, "Temperature characteristics of bipolar cascade lasers", App. Phys. Lett, vol. 77, no. 2, 172-174, 2000.

[9] L. A. Coldren, S. W. Corzine, "Diode lasers and photonic integrated circuits", John Wiley and Sons, Inc., 1995.

[10] S. C. Kan, D. Vassilovski,, T. C. Wu, K. Y. Lau, "Quantum capture and escape in quantum-well lasers-Implications on direct modulation bandwidth limitations", IEEE Photon. Tech. Lett., vol. 4, no. 5, 428-431, 1992.

[11] K. Y. Lau, "Dynamics of quantum well lasers", in *Quantum Well Lasers*, P. S. Zory, ed., Academic Press Inc. San Diego, Ca. 1993.

Chapter 5: Summary and directions for further work

5.0 Introduction

The goal of this thesis was to realize a bipolar cascade laser and, in so doing, gain a better understanding of the materials science and physics of the device. A considerable amount of knowledge has been acquired during the course of this work. The bipolar cascade laser's operating principles and inherent limitations are now more clearly understood and design methodologies have been established in order to improve the device's quantum efficiency and modulation properties. A new type of device, the antiresonant reflecting optical waveguide bipolar cascade laser (ARROW-BCL) has been proposed to overcome an inherent limitation of the designs considered in this thesis. The proposal raises new questions about the material science, physics design and limitations of this new laser.

Undoubtedly the single greatest contribution of this work to the laser community is the realization of the first bipolar cascade laser to operate continuously at room temperature. Section 5.1 summarizes the milestones attained in the process of realizing this achievement and the subsequent study of the BCL. Section 5.2 indicates directions for the study and extension of current and proposed designs as well as suggestions for more an even more exotic BCL.

5.1 Summary

The initial part of the materials research for this thesis was directed toward the realization of tunnel junctions with low reverse bias resistance. This necessitated achieving very high doping densities. In the case of the p-type dopant, beryllium, growth efforts yielded a doping density of 2×10^{19} cm^{-3} in GaAs. The n-type doping density was nearly equal to this at 1.6×10^{19} cm^{-3} in GaAs using silicon as the dopant. It was determined that to achieve such high densities a substrate temperature of 480 °C was required during growth. The intermediate temperature growth resulted in oxygen incorporation on the order of $\sim10^{18}$ cm^{-3}. Oxygen exists as a deep state in GaAs and

assists the tunneling process, leading to tunnel junctions with substantially less resistance than could be concluded from the measured doping densities alone.

Modeling of the tunnel junctions was done using the Wentzel-Kramers-Brillioun approximation for tunneling and numerically calculating an integral equation for the tunneling current. Good agreement was found between the model and the measurements of a tunnel junction. The model was then used to determine the trends that could be expected in the tunnel junction's I-V characteristics and contact resistance if doping densities and materials composition were varied.

The materials studies indicated growth temperature restrictions that had to be placed upon the growth of the active stages. Growth and photoluminescence studies were conducted to determine an appropriate materials system for growing high optical quality active regions within the latter constraints. InGaP, lattice-matched to GaAs, was determined to be the best candidate for the cladding material. Growth studies were also conducted to ascertain appropriate growth conditions for the quantum wells. These efforts lead to the first demonstration of a bipolar cascade laser operating continuous wave, at room temperature. A record differential quantum efficiency of 99.3% was achieved.

Studies of the BCLs were conducted to determine their light output and voltage versus bias current properties (L-I and I-V, respectively). The L-I curves showed separate threshold currents from the top and bottom gain stages. This effect was attributed to lateral current spreading. The I-V curves clearly showed two diode voltage drops plus a small differential resistance. Some devices demonstrated antiguiding effects typical of narrow stripe gain guided lasers. Wide stripe devices (~40 μm) were not as adversely effected by the lateral current spreading but never achieved the high differential slope efficiencies of the narrower stripe devices.

Extensive thermal modeling was done of the BCL. Direct surface measurements using a micro thermal couple probe were done and these were compared to finite element simulations with excellent agreement between the two. The results were compared to an analytical model with good agreement below the first threshold but anomalous divergent behavior beyond that point. The slope efficiency and threshold current sensitivity to temperature were characterized. Good agreement was found between the measurements

and reports in the literature on conventional quantum well lasers in the same material system.

The modulation response of the bipolar cascade laser was measured. Both the relaxation oscillation frequency (maximum of 1.5 GHz) and spur-free dynamic range (104 dB-$Hz^{2/3}$) of the laser were found to be below anticipated values. The compromised performance was attributed to the thermal effects established through measurement and simulation.

A second generation device was designed taking into account all that was learned from the measurements and simulation of the first generation BCL. The waveguides were broadened to reduce optical loss. $In_{0.1}Ga_{0.9}As$ was substituted for GaAs as the tunnel junction material to further reduce the resistance of the junction. Two quantum wells were used in the active regions to reduce sensitivity to thermal effects. Oxidation layers were added to the cladding regions to provide both a current aperture and index guiding for the optical field. The current aperture alleviates the double threshold behavior while the index guiding reduces the deleterious effects of the carrier density-induced anti-guiding behavior.

The first generation and second generation BCLs both employed separate waveguides for the gain stages. Such an arrangement couples poorly into single mode fiber as the two waveguides are essentially optically uncoupled. Bringing the waveguides physically closer results in unacceptably high loss from the tunnel junctions. A new device was proposed to produce a coherent output optical beam suitably narrow for efficient single mode optical fiber coupling while still minimizing the optical field overlap with the optically lossy tunnel junctions. The new device uses an antiresonant reflecting optical waveguide (ARROW) grown vertically (transverse direction) into the structure during the epitaxial phase. The gain stages are contained in the low index material and the tunnel junctions are contained in the high index spacer regions. The near and far optical field patterns were calculated for the ARROW-BCL. A set of design curves was generated for radiation and absorption loss and threshold current density versus a variety of parameters. A first generation, single stage design was proposed.

5.2 Directions for future work

The directions in which BCL research should move should be driven by the contemplated applications. Most of this thesis has been aimed toward achieving high differential slope efficiency and consideration of issues related to slope efficiency seem to be a natural starting point. High differential laser slope efficiency is of concern in directly modulated high fidelity analog links. It is desirable to achieve a differential slope efficiency so large that, including all optical losses, link gain is achieved without the aid of amplifiers. In concept, one need only include more gain stages in the cascade to achieve this end. In practice, as has been demonstrated in Chapter 3, the diode voltage drop associated with each gain stage can result in thermally compromised performance.

The answer to the question of how many gain stages may be successfully cascaded depends upon the outcome of the characterization of the second generation BCL. Some back of the envelope calculations should shed some light on the issue, however. In the case of the device used for the thermal measurement study in Chapter 3, the threshold current density was roughly 1 kA/cm^2 for the top gain stage. Assuming uncoated cleaved facets, a loss of 15 cm^{-1} for a narrow stripe, gain guided laser [1], a loss of 1.5 cm^{-1} in the broad waveguide (second generation) BCL [2], and a gain coefficient of 2400 cm^{-1} for the active region, the second generation BCL can be expected to have a threshold current approximately 1/3 of the first generation design. A three-fold reduction in the threshold current density places a cascade of six gain stages within reason. Based upon the results of the of the discrete cascade experiment outlined in Chapter 1 [3], a six stage BCL emplaced in a short haul, multimode, analog optical link should achieve link gain.

Similar arguments can be made for the ARROW-BCL, but more gain stages would be required for a given link efficiency and loss per unit length to compensate for the energy lost in the side lobes of the farfield radiation pattern. Longer wavelength devices provide a degree of trade-off between the reduction in the diode voltage drop resulting from the generation of less energetic photons with the increase in threshold current resulting from Auger recombination processes. In the analysis presented in Chapter 4, threshold current densities on the order of 2 kA/cm^2 were calculated for an

ARROW-BCL emitting at 1.55 μm. Emission at 1.55 μm reduces the per gain stage voltage to ~0.82 V from the ~1.25 V at a wavelength of 980 nm. Based upon the performance of the 980 nm BCLs, at least three gain stages should be possible at 1.55 μm. The inclusion of additional gain stages does reduce the radiation loss by a factor of 1/N (see Chapter 4), but the advantage offered in by this method decreases with each subsequent stage added. Communications wavelength lasers are more heat sensitive than the near-infrared lasers, but the deep QWs of the ARROW structure should offset this but it is presently unclear what effect the absence of the double hetero-barrier will have on the carrier dynamics of the ARROW-BCL. The study and understanding of the ARROW-BCL's carrier and modulation behavior should be quite interesting but one of the clearest imperatives for further research is the determination of the maximum number of cascadable sections at a given wavelength for a given design.

A more practical limitation may arise in setting the maximum number of gain stages in the ARROW-BCL. The stack height of an ARROW-BCL for a three-core device at 1.55 mm is already on the order of 12-15 μm. Vertical cavity surface emitting lasers (VCSELs) are of similar stack height at the same emission wavelength. Additional gain stages raise the height by approximately 2-3 μm per stage. There is no clear technological reason preventing epitaxial structures of such extended dimension to be grown, but the time required to do so may prove prohibitive. Historically, the difficulties in growing several stages of an ARROW-BCL pale in comparison to the technological hurdles negotiated in growing the first VCSELs. The increase in stack height of the ARROW-BCL compared to long wavelength VCSELs, both in an absolute and percentage change sense, is small with respect to the increase in stack height of VCSELs over edge emitters.

From the perspective of the optical systems engineer, the important figure of merit for an optical link is the signal-to-noise ratio (SNR). The current generated at the detector (which is proportional to the incident optical power) is directly proportional to the differential slope efficiency of the laser. The detected signal power then goes to the square of the laser's differential slope efficiency or, equivalently, to the square of the number of gain stages, as the detected electrical power goes to the square of the photocurrent. The electrical noise power generated by the noise on the photon stream is

in direct proportion to the photocurrent. The SNR can then be expected to increase roughly as N, where N is the number of sections in the cascade. It would ideally require the study of the SNR in a number of bipolar cascade lasers of varying numbers of cascaded sections, nearly equivalent in any other way, under various operating conditions to experimentally pinpoint the precise relationship. In particular, it should be very interesting to determine and contrast the noise performance of BCLs of multiple waveguide design with those of single waveguide design, such as the ARROW-BCL. The theoretical prediction of the outcome of such an experiment was made by Rana and Ram in [4].

The analysis presented in the previous paragraph failed to include other noise sources, not the least of which is the noise contribution from the tunnel junctions. The noise of the tunnel junction in reverse bias was modeled as shot noise in [4]. This assumption is experimentally supported in [5], where the measured noise spectrum of tunnel diodes in reverse bias was found to be pure shot noise. Reference [6] predicts a 1/m reduction in the shot noise of a tunnel diode, where m is the number of tunneling paths (introduced by traps in the forbidden region), but such a reduction was not found in the measurements conducted in the study of [5]. The reduction is expected to appear only at frequencies in excess of $1/\tau_c$, where τ_c is the trap capture time, so the noise reduction offered by the deep states may still prove useful only at frequencies beyond the modulation bandwidth of the laser. At the large values of bias needed to achieve large modulation bandwidths in a laser, the noise of the tunnel junction could be substantial and warrants further study.

The analog optical link designer must also concern herself with the deleterious effects of intermodulation distortion. The keystone element of the BCL, the tunnel junction, is a non-linear device and represents a source of intermodulation distortion in addition to any others that are found in conventional edge emitting lasers. The analysis of the distortion introduced by the nonlinearity of the tunnel junctions will be a function of the parameters of the tunnel junctions and other parasitic circuit elements in the BCL. Without specific knowledge of the particular BCL under consideration, or the requirements of the link in which it is to be used, it is difficult to make broad based conclusions about the limits the tunnel junction(s) place on the BCL's spur-free dynamic

range [7]. If the other issues limiting the number of casacadable sections are resolved, then the nonlinearities in the tunnel junctions could prove to be the overall limiting factor in the number of usable gain sections in analog, fiber optic links. Research in this area should focus primarily on the tunnel junctions themselves initially, but would also be a natural outgrowth of the previous suggestions for future work.

The discussion thus far has centered on analog applications but the majority of communication links are digital. The BCL appears to have an advantage here as, for a given *current* pulse amplitude, the number of generated photons is increased by a factor of N compared to a conventional laser of similar parameters. The bit error rate in a digital system is an exponential function of the number of photons per bit [8] making it appear as though the BCL would be an ideal candidate for digital applications. As previously pointed out, the cascading process requires an N-fold increase in voltage making the BCL the device of choice only in the case where the electrical source can generate sufficient voltage. Consider a system with a 5 V rail. If 2 V is lost in biasing the current source's constituent elements, the remaining 3 V is sufficient to drive three gain stages in a 1.55 μm BCL. A threefold increase in the number of photons generated per pulse reduces the bit error rate by e^{-3} [8]. The limitation in the ARROW-BCL for digital applications will be the ability to rapidly move carriers in and out of the very wide core regions as the laser is switched between the high and low states. Ideally the modulation bandwidth of a laser is nearly equal to the relaxation oscillation frequency. Transport times associated with the diffusion of carriers from the edge of the core sections to the QWs can substantially reduce the intrinsic bandwidth of the laser [9]. The very wide core regions will substantially reduce the intrinsic bandwidth of the ARROW-BCLs. The maximum on-off keying speed of the BCL will be less than or equal to the modulation bandwidth of the laser. The depletion capacitance of the tunnel junction is negligible with respect to that of the core regions. Digital modulation of BCLs has been completely neglected thus far.

Distributed feedback lasers (DFB) are normally employed in digital links to meet the requirement of single-longitudinal mode performance. The ARROW-BCL would definitely be the BCL design of choice in this respect as the coherent optical coupling of all the gain stages would require only a single corrugated section, and single regrowth,

near the topmost layer. The requirement to have identical corrugations near each gain stage in the multiple waveguide BCL would render implementation all but impossible. The DFB ARROW-BCL would appear to be the natural evolution of the ARROW-BCL concept. The placement of the corrugation could be problematic, however. A field null exists at the topmost core-to-first period DBR layer in the unperturbed ARROW structure making it unsuitable for placement of the corrugation. Placement of the corrugation in either of the topmost DBR layers permits only relatively weak interaction with the optical field. Considering the width of the core regions, it may be possible to place the corrugation midway between the core-to-DBR interface and the QWs. This placement permits effective interaction between the optical field and the perturbation while retaining sufficient distance for the regrowth to morphologically smooth prior to reaching the interface. The coherent coupling of the optical fields in the core regions of the ARROW obviates the need for more multiple corrugation/regrowth steps.

As indicated in Chapter 4, the lateral ARROW laser has been studied for high power applications. Lateral ARROW lasers use very broad cores to side step the catastrophic optical damage and filamentation problems associated with large power densities [10]. Vertical ARROW lasers can be expected to enjoy similar optical power handling cpabilities. The ability to electrically cascade lasers in the vertical direction, coupled with the use of ARROW waveguides, brings the idea of two-dimensional edge-emitting 2-d ARROW arrays, perhaps for erbium-doped fiber pumping, into the realm of possibility. The problems with power dissipation and wall plug efficiency would take on heightened meaning in this application, as now the lateral heat dissipation path will be blocked by the adjacent sections of the lateral ARROW lasers. This difficulty, coupled with the need for acquiring expertise in lateral ARROW laser structures, renders the pursuit of two-dimensional arrays an advanced research topic. In particular, it is not clear if any advantage would be gained in using two-dimensional arrays over simply increasing the number of core regions in a lateral ARROW laser while introducing sufficient interelement loss to suppress higher order modes [11,12,13].

The bipolar cascade laser, in all its incarnations, should remain an active area of research for some time to come. Many interesting scientific and engineering challenges remain both from fundamental and applied standpoints. Undoubtedly, many new

properties and ideas await discovery. Moving the device from the research laboratory into real world optical links would be an exciting development but much more developmental work in areas such as heat sinking and packaging are required before this may become a reality. In all, an exciting new area of research in the world of quantum well lasers has opened.

References:

[1] H. C. Casey, Jr., M. B. Panish, "Heterostructure Lasers", New York, Academic Press, 1978.

[2] M. R. Gokhale, J. C. Dries, P. V. Studenkov, S. R. Forrest, and D. Z. Garbuzov, "High-Power High-Efficiency 0.98-μm Wavelength InGaAs-(In)GaAs(P)-InGaP Broadened Waveguide Lasers Grown by Gas-Source Molecular Beam Epitaxy", IEEE J. Quantum Electron., vol. 33, no. 12, 2266-2276, 1997.

[3] C. H. Cox III, H. V. Roussell, R. J. Ram, R. J. Helkey, "Broadband, directly modulated analog fiber link with positive intrinsic gain and reduced noise figure", IEEE International Topical Meeting on Microwave Photonics, Technical Digest, Piscataway, NJ, 157-60, 1998.

[4] F. Rana, R. J. Ram, "Photon noise and correlations in semiconductor cascade lasers", Appl. Phys. Lett., vol. 76, no.9, 1083-1085, 2000.

[5] A. L. Conjeaud, B. Orsal, A. Dhouib, R. Alabedra, and L. Gouskov, "Si-implanted n+-InP/p-InP junctions: Electrical characterization and noise", J. Appl. Phys. Vol. 59, no. 5, 1707-1713, 1986.

[6] G. Lecoy, Thèse d'Etat, U. S. T. L. Montpellier, 1969.

[7] H. T. Lee, personal communication.

[8] G. P. Agrawal, "Fiber-optic communication systems", John Wiley and Sons, Inc. New York, 1992.

[9] L. A. Coldren, S. W. Corzine, "Diode lasers and photonic integrated circuits", John Wiley and Sons, Inc., 1995.

[10] D. Z. Garbuzov, N. I. Katsavets, A. V. Kochergin, and V. B. Khalfin, "An experimental and theoretical study of the local temperature rise in of mirror facets in InGaAsP/GaAs and AlGaAs/GaAs SCH SQW laser diodes", Proc. AIP Conf. 240, 6-13, 1991.

[11] C. Zmudzinski, D. Botez, L. J. Mawst, A. Bhattacharya, M. Nesnidal, R. F. Nabiev, "Three-core ARROW-Type diode laser: Novel high-power, single-mode device, and effective master oscillator for flared antiguided MOPA's", Journ. Select. Topics in Quant. Elec., vol. 1, no. 2, 129-137, 1995.

[12] L. J. Mawst, D. Botez, C. Zmudzinski, and C. Tu, "Antiresonant reflecting optical waveguide-type, single-mode diode lasers", Appl. Phys. Lett., vol. 61, no. 5, 503-505, 1992.

[13] L. J. Mawst, D. Botez, C. Zmudzinski, and C. Tu, "Design optimization of ARROW-type diode lasers", IEEE Phot. Tech. Lett., vol. 4, no. 11, 1204-1206, 1992.

A. Mathematical description of the tunnel junction

This appendix places on firmer mathematical footing tunneling integral equation presented in Chapter 2 [1,2]. Four criteria must be met in realizing a tunnel junction: 1) There must be some finite probability of tunneling, 2) there must be occupied states to tunnel from, 3) there must be unoccupied states to tunnel to and 4) crystal momentum must be conserved in the tunneling process. As described in Chapter 2, the tunneling probability may be calculated to excellent approximation using the Wentzel-Kramers-Brillioun (WKB) found in any quantum mechanics text:

$$T_t \cong \exp\left[-2\int_{-x_1}^{x_2} |k(x)|dx\right] \tag{A.1}$$

where T_t is the tunneling probability, |k(x)| is the absolute value of the wave vector in the tunnel barrier, and $-x_1$ and x_2 are the classical turning points. The classical turning points are defined as the point in space where the electron energy is just equal to the tunneling potential energy.

The value of the wave vector is given by:

$$k(x) = \sqrt{\frac{2m^*}{\hbar^2}(U-E)} = \sqrt{\frac{2m^*}{\hbar^2}\left(\frac{\left(\frac{E_g}{2}\right)^2 - (q\mathrm{E}x)^2}{E_g}\right)} \tag{A.2}$$

where E_g is the bandgap energy, q is the electron charge, U is the tunneling potential, and E is the total electric field (built-in and applied) assuming a parabolic potential and a uniform electric field. The total momentum must be conserved in the tunneling process, and thus any transverse momentum must be accounted for in a calculation of the tunneling probability. The energy may be divided into components associated with momentum perpendicular to the tunnel junction E_x, and energy associated with momentum components transverse to the tunnel junction, $E_\perp$. For $E_\perp > 0$ it can be shown :

$$PE - E_x = \frac{E_g^2/4 - E_o^2}{E_g} + E_\perp \tag{A.3}$$

with classical turning points given by:

$$-x_1', x_2' = \mp \frac{1}{qE}\sqrt{E_g^2/4 + E_g E_\perp} \tag{A.4}$$

Substituting Eqns. A.3 and A.4 into Eqn. 2.1 and carrying out the integral gives:

$$T_t \equiv \exp\left(-\frac{\pi m^{*1/2} E_g^{3/2}}{2\sqrt{2} q\hbar E}\right)\exp\left(-\frac{2E_\perp}{\overline{E}}\right) \tag{A.5}$$

where m* is the electron effective mass and where:

$$\overline{E} \equiv \frac{4\sqrt{2} q\hbar E}{3\pi m^{*1/2} E_g^{1/2}} \tag{A.6}$$

sets the range of meaningful transverse momentum.

To determine the current at equilibrium detailed balance can be invoked by considering the current from the occupied states of the valence band to the empty states of the conduction band, $I_{V\to C}$, and the current from the occupied states of the conduction band to the unoccupied states of the valence band, $I_{C\to V}$, separately.

$$I_{C\to V} = A\int_{E_C}^{E_V} f_C(E)n_C(E)T_t[1-f_V(E)]n_V(E)dE \tag{A.7a}$$

$$I_{V\to C} = A\int_{E_C}^{E_V} f_V(E)n_V(E)T_t[1-f_C(E)]n_C(E)dE \tag{A.7b}$$

where the $f_{C,V}(E)$ are the are the conduction band and valence band quasi-Fermi distributions in the n- and p-doped regions respectively, $n_{C,V}(E)$ are the density of states in the conduction and valence bands respectively, T_t is the tunneling probability assumed to be equal for both tunneling directions, and A is a constant. The total tunneling current at bias is then given as follows:

$$I_t = I_{C\to V} - I_{V\to C} = A\int_{E_C}^{E_V}[f_C(E)-f_V(E)]T_t n_C(E)n_V(E)dE \tag{A.8}$$

To derive the current as a function of bias to include transverse momentum effects the incident current per unit area in the energy range $dEdE_\perp$ is considered:

$$dJ = \frac{qm^*}{2\pi^2\hbar^3}dEdE_\perp f(E) \tag{A.9}$$

where:

$$E_\perp = \frac{\hbar^2 k_\perp^2}{2m_\perp^*} \tag{A.10}$$

Eqns. A.9 may be derived most easily by first considering the flux of electrons in k-space and then converting to energy by assuming the parabolic bands given by Eqn A.10. Consider a particle of charge q, moving in a constant electric field, E_{field}, such that the velocity in k-space is:

$$\frac{dk}{dt} = \frac{qE_{field}}{\hbar} \tag{A.11}$$

The number of states in a ring of radius $k_\perp$ in k-space is:

$$\text{number of states} = 2\frac{2\pi k_\perp dk_\perp}{(2\pi/L)^3} \tag{A.12}$$

where the extra multiplicative factor of 2 accounts for spin degeneracy.

The total charged flux (number per unit volume of crystal, per unit time) is given by the electron charge, times the velocity in k-space, times the number of available states times the probability of occupancy:

$$\text{Flux} = \frac{q^2 E_{field} 2\pi}{\hbar 4\pi^3} k_\perp dk_\perp f(E) \tag{A.13}$$

Making use of Eqn. A.10:

$$k_\perp = \sqrt{\frac{2m^* E_\perp}{\hbar^2}} \tag{A.14}$$

$$dk_{\perp} = \frac{m^*}{\hbar}\left(\frac{2m^*E_{\perp}}{\hbar^2}\right)^{-\frac{1}{2}} dE_{\perp}$$

(A.15)

Substituting Eqns. A.14 and A.15 into Eqn. A.13 yields:

$$\text{Flux} = \frac{q^2 E_{field} f(E)}{2\pi^2\hbar^3} dE_{\perp}$$

(A.16)

The current density is then given by Eqn. A.16 times a differential region in space dx. In the uniform field $qE_{field}dx$ may be replaced by dE, as $qE_{field}=dE/dx$, leading directly to equation A.9.

Proceeding as in Eqns. A.7 and A.8 the current density integral is then given by:

$$J_t = \frac{qm^*}{2\pi^2\hbar^3}\exp\left(-\frac{\pi m^{*1/2}E_g^{3/2}}{2\sqrt{2}q\hbar E}\right)\int dE_{\perp}dE\left[f_C(E)-f_V(E)\right]\exp\left(-2\frac{E_{\perp}}{E}\right)$$

(A.17)

The limits of integration are dictated by the conditions $0 \leq E_{\perp} \leq E_1$ and $0 \leq E_{\perp} \leq E_2$, where E_1 and E_2 are the electron energies measured from the n-band and p-band edges respectively [5].

The integration over $E_{\perp}$ is easily carried out resulting in:

$$J_t = \frac{qm^*}{2\pi^2\hbar^3}\exp\left(-\frac{\pi m^{*1/2}E_g^{3/2}}{2\sqrt{2}q\hbar E}\right)\left(\frac{E}{2}\right)\int\left[f_C(E)-f_V(E)\right]\left(1-\exp\left(-2\,E/E\right)\right)dE$$

(A.18)

where:

$$E \equiv \left(qV_{bi}N^*/2\varepsilon_s\right)^{1/2}, \quad N^* \equiv \frac{N_A N_D}{(N_A+N_D)}$$

(A.19)

V_{bi} is the built in potential, ε_s is the semiconductor permittivity, and N_A and N_D are the p- and n-type dopant concentrations respectively.

References:

[1] E.O. Kane, "Theory of tunneling", J. Appl. Phys., vol. 32, no. 1, 83-91, 1960.
[2] E.O. Kane, "Zener tunneling in semiconductors", J. Phys. Chem. Solids, vol. 12, 181-188, 1959.

Appendix B. Laser physics basics

In order to appreciate the essential elements of laser design it is first necessary to understand some important aspects of laser physics. The details presented here closely follow the intuitively appealing phenomenological approach presented in Chapter 2 [1]. The interested reader may refer to later chapters of [1], as well as [2,3], for more thorough and rigorous treatments of laser physics.

It is helpful to start out by defining two of the terms to be used in the discussion [1]:

Active region: the region where recombining carriers contribute to useful gain and photon emission.

Internal quantum efficiency, denoted η_i: the fraction of terminal current that generates carriers in the active region.

In the definition of the active region it is important to note the use of the words *useful gain.* In other words, simply because radiative recombination takes place in a region of the laser doesn't imply that region is a part of the active region. It is equally important to note that in the definition of η_i all carriers which make their way from the electrical terminals to the active region are included in the definition, whether or not they eventually participate in radiative recombination contributing to the laser's gain.

The goal in this derivation is to write down rate equations for the carrier and photon densities. The time rate of change of the carrier density in the active region may be equated to the generation rate of the carriers minus the recombination rate of the carriers in the same manner as for other semiconductor devices:

$$\frac{dN}{dt} = G_{gen} - R_{rec} \tag{B.1}$$

where N has units of cm^{-3} and G_{gen} and R_{rec} have units of $1/(cm^3 \cdot sec)$. The carriers in the active region are sourced by the injected current, I, of which the percentage η_i gets to the

active area. Dividing by the electron charge, q and the active area volume, V, to keep the equation dimensionally consistent, yields:

$$G_{gen} = \frac{\eta_i I}{qV} \tag{B.2}$$

There are several contributions to the R_{rec} term in Eqn. B.1. Carriers may recombine in the active region through spontaneous radiative and non-radiative mechanisms. They may also, preferably, recombine during a stimulated emission process. Only the latter process requires the presence of photons, while the first three may be related to the carrier density alone. Some types of non-radiative recombination are due to defects or impurities and hence can be written as being proportional to the carrier density, AN, where A is the constant of proportionality. Another type of non-radiative process, Auger recombination, requires three carriers and is therefore taken to be proportional to the carrier density cubed, CN^3, where C is referred to as the Auger coefficient. Auger recombination is normally not of much concern for shorter wavelength infrared lasers (emission wavelength $\leq$ 1.1 μm), but is substantial at longer wavelengths (1.3-1.55 μm). More rigorously speaking, the Auger recombination term should read as PN^2, or NP^2, where P is the hole density. Since quasineutrality is assumed to hold within the active region it is legitimate, however, to make the substitution P→N.

Spontaneous emission is a radiative process and is proportional to the product of the number of electrons and the number of holes. Again assuming quasineutrality this may be written BN^2, where B is known as the bimolecular recombination coefficient and is typically on the order of 10^{-10} cm^3/s. In sum, these radiation mechanisms may be expressed mathematically as:

$$R_{rec} = BN^2 + (AN + CN^3) + R_{st} = BN^2 + \frac{N}{\tau} + R_{st} \tag{B.3}$$

On the far right hand side of Eqn. B.3 the notion of a carrier lifetime, τ, has been introduced. In the case of spontaneous emission τ is a linear function of N (assuming B

is truly a constant). When there is a meaningful amount of Auger recombination current it is clear that τ is quadratic in N. Leaving R_{st} unaddressed for the moment the rate equation for N has now become:

$$\frac{dN}{dt} = \frac{\eta_i I}{qV} - \frac{N}{\tau} - R_{st} \tag{B.4}$$

It is also possible to right down a rate equation governing the photon density in the *cavity mode* of interest. If more than one mode in the cavity is of interest, then a separate photon rate equation must be written down for each mode. The approach to the photon density rate equation is the same as that which was taken for the electron density; set the time rate of change of the photon density equal to the photon sources and sinks. The primary source of photons in the lasing mode is through stimulated recombination of carriers, given by the stimulated recombination rate, R_{st}. It is necessary to be careful here as we cannot simply use R_{st} as a source term. The volume occupied by the photons is typically much larger than the active region volume. Therefore we must multiply R_{st} by V, to get the number of carriers stimulated to recombine, and divide that quantity by V_p, the photon volume, to arrive at the stimulated photon number per unit of *photon* volume. The ratio of V/V_p is normally termed as the *confinement factor* and is denoted by Γ.

In a similar vane the spontaneous recombination rate, R_{sp}, is also multiplied by Γ. This term still requires some further modification. Unlike the stimulated emission, which by definition emits only into the lasing mode, the spontaneous emission may go into any of the allowed cavity modes (although, typically, not with equal probability). To account for this the spontaneous emission term must be multiplied by the probability that a spontaneously emitted photon will go into the lasing mode of interest. This term is denoted β and is referred to as the *spontaneous emission factor*. Finally, to account for photon loss, a photon lifetime τ_p is assigned, leading to a loss term of the form N_p/τ_p, where N_p is the photon number density in the lasing mode of interest. The origin and form τ_p of will be addressed shortly.

To determine the functional form of the stimulated emission term, consider a photon density, N_p, which grows by the amount ΔN_p in traversing the distance Δz. Setting this equal to an exponentially increasing term yields:

$$N_p + \Delta N_p = N_p e^{g\Delta z} \tag{B.5}$$

where g is the gain per unit length.

Assuming the distance is sufficiently small that the exponential term may be written as exp(x)=1+x and realizing that Δz is equal to $v_g \Delta t$, where v_g is the group velocity, gives:

$$\left(\frac{dN_p}{dt}\right)_{gen} = R_{st} = \frac{\Delta N_p}{\Delta t} = v_g g N_p \tag{B.6}$$

Collecting all the terms that have been thus far derived into the rate equations results in:

$$\frac{dN}{dt} = \frac{\eta_i I}{qV} - \frac{N}{\tau} - v_g g N_p \tag{B.7a}$$

$$\frac{dN_p}{dt} = \Gamma v_g g N_p + \Gamma \beta_{sp} B N^2 - \frac{N_p}{\tau_p} \tag{B.7b}$$

The form of τ_p may be determined by examining the round trip condition that must be met in order for the laser to achieve threshold. The gain of the laser must be increased to the point that all losses encountered by the electric field in making one complete traversal of the optical cavity are compensated for. Equivalently, this may be restated as the requirement that in the course of one complete round trip of the optical cavity the electric field replicates itself. Assuming two mirrors of reflection coefficients r_1 and r_2 (assumed real), internal photon loss of α_i (cm^{-1}), a *modal gain* of Γg and a cavity length L, these statements can be expressed mathematically as:

$$r_1 r_2 e^{(\Gamma g - \alpha_i)L} = 1$$

(B.8)

Solving this equation for Γg:

$$\Gamma g_{th} = \alpha_i + \frac{1}{L}\ln\left(\frac{1}{r_1 r_2}\right) = \alpha_i + \alpha_m$$

(B.9)

where g_{th} denotes the threshold value of gain and α_m defines the mirror loss per unit length. Multiplying by v_g allows the RHS of Eqn. B.9 to be recast as an inverse photon decay rate; τ_p can now be defined as:

$$\frac{1}{\tau_p} = v_g(\alpha_i + \alpha_m)$$

(B.10)

Since the physics of the gain of the quantum well are beyond the scope of this discussion it is simply here stated that the peak gain of a quantum well versus carrier density may be well approximated as:

$$g = g_o \ln\left(\frac{N}{N_{tr}}\right)$$

(B.11)

where N_{tr} denotes the transparency carrier density. The transparency carrier is defined as the carrier density at which the material crosses over from being lossy (i.e. negative gain) into providing (positive) gain. It is important to note that the gain will never exceed the value given in Eqn. B.9. If the gain were to exceed its threshold value then the optical field would grow monotonically without bound as it circulated about the cavity. But this is a contradiction for if the field grows larger and larger the stimulated emission rate increases, thereby reducing the carrier density and, as per Eqn. B.11, the gain, until the field again just replicates upon making one full round trip of the optical cavity.

Without explicitly solving Eqns. B.7 some useful relationships that will be needed in this and Chapter 4 can be derived. At steady state the time derivative in Eqn. B.7a may be set equal to zero. Then a threshold current may be defined as:

$$I_{th} = \frac{N_{th} q V}{\eta_i \tau}$$

(B.12)

In Eqn. B.12 the requirement that the gain be clamped above threshold dictates that the carrier density must also clamp at some value N_{th}. If N clamps then the spontaneous, nonradiative, and leakage rates must also clamp as they depend monotonically upon N. Therefore it can be concluded that, ideally, above threshold any additional carriers that are injected into the active region are transduced into photons. This permits Eqn. B.7a to be rewritten for currents above the threshold current as:

$$\frac{dN}{dt} = \eta_i \frac{(I - I_{th})}{qV} - v_g g N_p \qquad (\mathrm{I} > \mathrm{I_{th}})$$

(B.13)

In the steady state this equation may be solved for the photon density as:

$$N_p = \frac{\eta_i (I - I_{th})}{q v_g g_{th} V}$$

(B.14)

It stands to reason that the power that is emitted from the laser must be proportional to N_p. The energy stored in the cavity is the product of N_p times the energy per photon, hν (where h is Planck's constant), times the photon volume V_p. The energy couples out of the cavity at a rate $v_g \alpha_m$,giving:

$$P_o = v_g \alpha_m N_p h \nu V_p$$

(B.15)

Substituting Eqn. B.14 into Eqn. B.15 yields:

$$P_o = \eta_i \left(\frac{\alpha_m}{\alpha_i + \alpha_m} \right) \frac{h\nu}{q} (I - I_{th})$$

(B.16)

Differentiating this equation with respect to I and dividing by the photon transition energy yields one of the parameters of greatest concern in the BCL, the differential quantum efficiency:

$$\eta_d = \left(\frac{q}{h\nu} \right) \frac{dP_o}{dI} = \eta_i \frac{\alpha_m}{\alpha_m + \alpha_i} \qquad (\mathrm{I} > \mathrm{I_{th}})$$

(B.17)

In the case of the BCL, it may be argued that the increase in differential slope efficiency results from an N fold increase in the single stage η_i, where N is the number of sections in the cascade. As the electron moves through the cascade it is essentially being recycled or reinjected into an active region for each of the gain sections.

Given the equations derived to this point it is also possible to estimate the threshold current of a laser. Knowledge of the threshold current's dependence upon device and material parameters provides the designer with the necessary information to improve laser performance. Combining Eqns. B.10 and B.11 yields the expression for the threshold carrier density:

$$N_{th} = N_{tr} e^{\frac{g_{th}}{g_o}} = N_{tr} e^{\frac{(\alpha_i + \alpha_m)}{(\Gamma g_o)}}$$

(B.18)

Combining Eqn. B.18 with Eqn. B.12, and using the approximation that $N/\tau \cong BN^2$:

$$I_{th} \cong \frac{qVBN_{tr}^2}{\eta_i} e^{2\frac{(\alpha_i + \alpha_m)}{(\Gamma g_o)}}$$

(B.19)

A more general expression than Eqn. B.19 for a multiple quantum well laser is:

$$I_{th} \cong \frac{qN_w VBN_{tr}^2}{\eta_i} e^{2\frac{(\alpha_i+\alpha_m)}{(N_w \Gamma g_o)}}$$

(B.20)

where N_w is the number of quantum wells, V is the volume of a *single* quantum well and Γ is assumed to increase linearly with the number of wells. The linear approximation for Γ is true for a small number of wells (≤ 3), or when the waveguide is so broad that the field intensity is close to being constant across the quantum wells.

The approximation for N/τ used in deriving Eqns. B.19 and B.20 is generally justified for high quality laser material. However, for lasers with emission in the range of telecommunication wavelengths (λ~1.3-1.6 μm) Auger recombination can make a significant contribution to the threshold current and an Auger term must added to Eqn. B.18:

$$I_{thAuger} \cong \frac{qN_w VCN_{tr}^3}{\eta_i} e^{3\frac{(\alpha_i+\alpha_m)}{(N_w \Gamma g_o)}}$$

(B.21)

One more result needs to be derived for the purposes of this chapter. The laser, being an oscillator, has a natural frequency termed the relaxation oscillation frequency. The relaxation oscillation frequency of the laser sets the upper limit at which the laser may be modulated. To arrive at this quantity a small signal analysis of the rate equations given by Eqns. B.7 is required. The following substitutions are made for the current, carrier density and photon density in the rate equations:

$$\begin{aligned} I &= I_O + I_1 e^{j\omega t} \\ N &= N_O + N_1 e^{j\omega t} \\ N_p &= N_{pO} + N_{p1} e^{j\omega t} \end{aligned}$$

(B.22)

The calculation continues by eliminating the steady state terms from the rate equations and solving for the small signal solution. The details are unenlightening so this final result, for the relaxation oscillation frequency, is simply presented here:

$$\omega_R^2 = \frac{v_g \left(dg / dN \right) N_{pO}}{\tau_p} \tag{B.23}$$

References:

[1] L. A. Coldren, S. W. Scott, "Diode Lasers and Photonic Integrated Circuits", John Wiley and Sons, Inc., 1995.
[2] S. L. Chuang, "Physics of Optoelectronic Devices", John Wiley and Sons, Inc., 1995.
[3] W. W. Chow, S. W. Koch, M, Sargent III, "Semiconductor-Laser Physics", Springer-Verlag Berlin Heidelberg, 1994.

Appendix C: Growth data for the bipolar cascade laser

The substrate temperature, Knudsen cell temperatures, the gas flow rates, chamber pressures and times used during the growth of the first bipolar cascade laser are given below in Table C.1. It should be noted that the temperatures, times and flow rates given are specific to the calibrations done prior to this particular growth on the particular gas-source molecular beam epitaxy machine used. Future attempts at growing this structure may make use of this data as a starting point but calibration of the particular system to be used, as close to the date of growth as possible, is a requirement.

Material	T_{sub}	T_{Ga}	T_{In}	T_{Si}	T_{Be}	AsH_3	PH_3	$P_g(10^{-5}\ T)$	*Time*	*Thickness*
GaAs:Be (Cap)	480→ 515	**926**	834	1045	**725**	1.0		1.3	720s	0.1 μm
InGaP:Be (Cladding)	480	**926**	**834**	1045	**645**		1.6	1.8	2700s	0.75 μm
GaAs	480	**926**	834	1045	645	1.0		1.3	183s	0.025 μm
GaAs	515	**945**	783	1045	645	1.0		1.3	400s	0.085 μm
InGaAs (QW)	515	**945**	**783**	1045	645	1.0		1.3	28s	0.008 μm
GaAs	515	**945**	783	1045	645	1.0		1.3	400s	0.085 μm
GaAs	480	**926**	834	1045	645	1.0		1.3	183s	0.025 μm
InGaP:Si (Cladding)	480	**926**	**834**	**1150→ 1045**	755→ 645		1.6	1.8	2700s	0.75 μm
GaAs:Si (Tunnel)	480	**926**	834	**1150**	755	1.0		1.3	183s	0.025 μm
GaAs:Be (Tunnel)	480	**926**	834	1150	**755**	1.0		1.3	183s	0.025 μm
InGaP:Be (Cladding)	480	**926**	**834**	1045→ 1150	**645→ 755**		1.6	1.8	2518s	0.75 μm
GaAs	480	**926**	834	1045	645	1.0		1.3	183s	0.025 μm
GaAs	515	**945**	783	1045	645	1.0		1.3	400s	0.085 μm
InGaAs (QW)	515	**945**	**783**	1045	645	1.0		1.3	28s	0.008 μm
GaAs	515	**945**	783	1045	645	1.0		1.3	400s	0.085 μm
GaAs	480	**926**	834	1045	645	1.0		1.3	183s	0.025 μm
InGaP:Si (Cladding)	480	**926**	**834**	**1045**	645		1.6	1.8	2518s	0.75 μm
GaAs:Si (Buffer)	640→ 480	**965→ 926**	750→ 834	**1045**	550	1.0		1.3	30min	0.5 μm

Table C.1

Notes:

1) Bold quantities indicate the cell was active during the growth of the layer.
2) The substrate was <100> GaAs:Si (~10^{18} cm^{-3}).
3) Values given for AsH_3 and PH_3 are in standard cubic centimeters per minute.
4) The cracker temperature was 900 °C.
5) The substrate, gallium and indium were ramped from the values given to the first InGaP layer values over the final 10 minutes of the buffer layer.
6) The beryllium and silicon cells were ramped up/down in the last/first 6.5 minutes of the InGaP layers to either side of the tunnel junction.
7) The ramp of the beryllium in the cap layer occurred in the final 6 minutes of the growth.

Appendix D: Single stage ARROW laser design

The following table contain the design for a single stage vertical ARROW laser design. This design would provide proof of concept of the vertical ARROW laser concept and open the door for ARROW-BCL designs.

Layer	*Material*	*Bandgap*	*Doping*	*Thickness*
Layer 28	InGaAs	Lattice matched	p-doped 2×10^{19}	0.2 μm
Layer 27	InP	----------	p-doped 5×10^{18}	0.5 μm
Layer 26	InP	----------	p-doped 2×10^{17}	1.0 μm
Layer 25	InGaAsP	λ=1.2 μm	p-doped 2×10^{17}	0.93 μm
Layer 24	InP	----------	p-doped 2×10^{17}	1.35 μm
Layers 6-23 This section is repeated 9 times.	0.8% compressively strained QW	λ=1.54 μm to 1.56 μm emission	undoped	7 nm
	InP	----------	undoped	9 nm
Layer 5	0.8% compressively strained QW	λ=1.54 μm to 1.56 μm emission	undoped	7 nm
Layer 4	InP	----------	undoped	1.35 μm
Layer 3	InGaAsP	λ=1.2 μm	n-doped 5×10^{17}	0.93 μm
Layer 2	InP	----------	n-doped 5×10^{17}	1.5 μm
Layer 1	InGaAsP	λ=1.2 μm	n-doped 10^{18}	0.93 μm
Substrate	InP	----------	n-doped ~10^{18}	----------

Table D.1

Appendix E: Matlab programs

This following pages provide the Matlab code used in calculating the data for many of the figures in Chapters 2 through 4. The code is commented but is, in general, not very user friendly. The parameter values must be changed from within the .m files and some .m files must be run, to generate necessary data, prior to the running of others. Many programs have sections of commented-out code that may be useful for calculating other quantities of interest or may not be functional at all in its current setting. It is presented here for archival purposes.

```
%This program calculates the L-I and I-V characteristics of
%the BCL


x=0.8;%Ga mole fraction in In(1-x)Ga(x)As
q=1.6e-19;%electron charge in coulombs
mo=9.11e-31;%electron mass in kg
L_z=80e-10;%length of quantum well in meters
k=1.38066e-23;%Joules/Kelvin
T=300;%Temperature in Kelvin
k_T=k*T/1.6e-19;%thermal energy in eV
hbar=6.63e-34/(2*pi);%in J*s
gamma1=6.85.*x + 20.4.*(1.-x);%Luttinger parameters
interpolated between GaAs and InAs
gamma2=2.1.*x + 8.3.*(1.-x);
emwell=(.067.*x + .025.*(1.-x))*mo;%electron effective mass
in qw in kg
hmwell=mo./(gamma1-2.*gamma2);%heavy-hole effective mass in
qw in kg
Ec_qw=0.0391;%Energy to first electron quantized state
measured from conduction band edge
Ev_qw=-0.0091;%Energy to first hole quantized state measured
from valence band edge
Ec_hh=1.2653;%Energy gap of In0.2Ga0.8As including strain
effects
No=1.8e18;%Transparency density i cm^-3
B=0.8e-10;%Bimolecualr recombination coefficient
C=0;%Auger coefficient
n_group=4.2;%Group velocity
c=3e10;%Speed of light in cm/s
L_laser=500e-4;%Length of Fabry-Perot cavity in cm
Stripe_top=20e-4;%Stripe width of laser
Stripe_bot=Stripe_top*1.5;%Assumed width of lower laser
caused by lateral diffusion
Vact_top=L_laser*L_z*Stripe_top*100;%Active regions of top
and bottom junctions /Factor of 100 converts Lz to cm
Vact_bot=L_laser*L_z*Stripe_bot*100;
gamma=0.0268;%Field overlap integral with QWs
Vph_top=Vact_top/gamma;%Volume occupied by photons from the
definition of gamma
Vph_bot=Vact_bot/gamma;
beta=0.869e-4;%spontaneous emission coefficient
eta=0.75;%current injection efficiency
vgr=c/n_group;%group velocity
geomnmir=.32;%power reflection coefficient for semiconductor
to air
alpham=L_laser^-1*log(geomnmir^-1);%Mirror and internal loss
constants in cm^-1
alphai=12;
tau_i=(alphai*vgr)^-1;%Mirror and internal loss in sec^-1
tau_m=(alpham*vgr)^-1;
tau=(1/tau_i + 1/tau_m)^-1;%Photon lifetime
h=6.63e-34;%Plancks constant in J*s
nu=3e8/980e-9;%photon frequency
```

```
q=1.6e-19;%electron charge
go=2100;%gain coefficient
range=[-50*k_T 50*k_T];%range of values for the quasiFermi
levels used in find zero of functions
hole_int_low_lim=Ev_qw-15*k_T;%lower integration limit
hole_int_up_lim=Ev_qw;%upper integration limit

elect_int_low_lim=Ec_qw;
elect_int_up_lim=Ec_qw+15*k_T;

%Calculate the threshold electron density
n_thresh=No*exp(1/(gamma*tau*vgr*go))

%Calculate the threshold quaiFermi level
Ef_n_thresh=fzero('n_dens_minus_n_int',range,[],n_thresh,x,m
o,L_z,k_T,hbar,Ec_qw,emwell,elect_int_low_lim,elect_int_up_l
im)/k_T;

%Generate a set of electron quasi-Fermi levels for the
topmost junction

Ef_n_top0=-
k_T*floor(Ef_n_thresh)/2:k_T:k_T*floor(Ef_n_thresh);
Ef_n_top1=k_T*floor(Ef_n_thresh)+.1*k_T:0.1*k_T:k_T*floor(Ef
_n_thresh*10)/10;
Ef_n_top2=k_T*floor(Ef_n_thresh*10)/10+.01*k_T:.01*k_T:k_T*f
loor(Ef_n_thresh*1e2)/1e2;
Ef_n_top3=k_T*floor(Ef_n_thresh*1e2)/1e2+.001*k_T:0.001/10*k
_T:k_T*floor(Ef_n_thresh*1e3)/1e3;
Ef_n_top4=k_T*floor(Ef_n_thresh*1e3)/1e3+.0001*k_T:0.0001/10
*k_T:k_T*floor(Ef_n_thresh*1e4)/1e4;
Ef_n_top5=k_T*floor(Ef_n_thresh*1e4)/1e4+.00001*k_T:0.00001*
k_T:k_T*floor(Ef_n_thresh*1e5)/1e5;
Ef_n_top6=k_T*floor(Ef_n_thresh*1e5)/1e5+.000001*k_T:0.00000
1*k_T:k_T*floor(Ef_n_thresh*1e6)/1e6;
Ef_n_top7=k_T*floor(Ef_n_thresh*1e6)/1e6+.0000001*k_T:0.0000
001*k_T:k_T*floor(Ef_n_thresh*1e7)/1e7;
Ef_n_top=[Ef_n_top0 Ef_n_top1 Ef_n_top2 Ef_n_top3
Ef_n_top4];


elect_int_low_lim=Ec_qw;
elect_int_up_lim=Ec_qw+15*k_T;



%Calculate the electron carrier density in the topmost
junction based upon the tabulated quasiFermi levels
for k=1:length(Ef_n_top)
   carrier_density_top(k)=(emwell*1.6e-19*1e-
6/(L_z*pi*hbar^2))*quad8('Electron_Fermi_Dist',elect_int_low
_lim, elect_int_up_lim,[],[],Ef_n_top(k));
end
```

```
%Assuming n=p (quasi-neutral) calculate the hole quasiFermi
level for a given elctron (hole) density

for m=1:length(Ef_n_top)

Ef_p_top(m)=fzero('n_dens_minus_p_int',range,[],carrier_dens
ity_top(m),x,mo,L_z,k_T,hbar,hmwell,...
      Ev_qw,hole_int_low_lim,hole_int_up_lim);
end

%Calculate the gain in the top junction as a function of
carrier density
g_top=go*log(carrier_density_top/No);

%Calculate current
I_top=((q*Vact_top*B*carrier_density_top.^2/eta).*(1 +
gamma.*beta*vgr*g_top./(1/tau - gamma*vgr*g_top)));
I_bot=I_top*Vact_bot/Vact_top;

%interpolate the I values for the bottom junction
carrier_density_bot=interp1(I_bot,carrier_density_top,I_top,
'spline');

%calculate the electron and hole quasiFermi levels for the
bottom junction
for m=1:length(Ef_n_top)
   m

Ef_p_bot(m)=fzero('n_dens_minus_p_int',range,[],carrier_dens
ity_bot(m),x,mo,L_z,k_T,hbar,hmwell,...
      Ev_qw,hole_int_low_lim,hole_int_up_lim);
end

for m=1:length(Ef_n_top)

Ef_n_bot(m)=fzero('n_dens_minus_n_int',range,[],carrier_dens
ity_bot(m),x,mo,L_z,k_T,hbar,Ec_qw,emwell,elect_int_low_lim,
elect_int_up_lim);
end


%Calculate gain for bottom junctions

g_bot=go*log(carrier_density_bot/No);

Nph_top=[gamma*beta*B*carrier_density_top.^2./(1/tau -
gamma*vgr*g_top)];
Nph_bot=[gamma*beta*B*carrier_density_bot.^2./(1/tau -
gamma*vgr*g_bot)];

Pout_top=(vgr*alpham*Nph_top.*Vph_top*h*nu/2);
Pout_bot=(vgr*alpham*Nph_bot.*Vph_bot*h*nu/2);
Pout=Pout_top+Pout_bot;
```

```
Volt_junc_top=Ef_n_top-Ef_p_top+Ec_hh;
Volt_junc_bot=-2*Ef_p_bot+Ec_hh;
V_tun_junc=I_top*6;
V=Volt_junc_top+Volt_junc_bot+V_tun_junc;

I=I_top;

figure(1)
plot(I*1e3, Pout*1e3)
title('Power/Facet vs. Current')
xlabel('Current (mA)')
ylabel('Optical Output Power (mW)')

figure(2)
plot(I*1e3, Pout_top*1e3)
title('Power/Facet Top vs. Current')
xlabel('Current (mA)')
ylabel('Optical Output Power (mW)')

figure(3)
plot(I*1e3, Pout_bot*1e3)
title('Power/Facet Bottom vs. Current')
xlabel('Current (mA)')
ylabel('Optical Output Power (mW)')

figure(4)
plot(I*1e3,V);
title('I vs V')
xlabel('Current (mA)')
ylabel('Voltage (Volts)')

figure(5)
plot(I*1e3,carrier_density_top)
title('Carrier density in top QW vs Current')
xlabel('Current (mA)')
ylabel('Carrier Density in top QW (cm^-3)')


figure(6)
plot(I*1e3,carrier_density_bot,I*1e3,carrier_density_top)
title('Carrier density in bottom and top QWs vs Current')
xlabel('Current (mA)')
ylabel('Carrier Density in bottom QW (cm^-3)')


%figure(7)
%plot(I,carrier_density_bot,'-
x',I_bot,carrier_density_top,'r-o')
%axis([0 5e-4 0 5e18])
%title('Carrier density in bottom QW vs Current')
%xlabel('Current (Amps)')
%ylabel('Carrier Density in bottom QW (cm^-3)')
```

```
% This is an auxiliary program to the BCL program for
determining carrier densities

function f=p_dens(Ef_p,n_dens,x,mo,L_z,k_T,hbar,hmwell,...
      Ev_qw,hole_int_low_lim,hole_int_up_lim)

f=n_dens-(hmwell*1.6e-19*1e-
6/(L_z*pi*hbar^2))*quad8('Hole_Fermi_Dist',hole_int_low_lim,
hole_int_up_lim,[],[],Ef_p);
```

```
% This is an auxiliary program to the BCL program for
determining carrier densities
function f=p_dens(Ef_p,n_dens,x,mo,L_z,k_T,hbar,hmwell,...
      Ev_qw,hole_int_low_lim,hole_int_up_lim)

f=n_dens-(hmwell*1.6e-19*1e-
6/(L_z*pi*hbar^2))*quad8('Hole_Fermi_Dist',hole_int_low_lim,
hole_int_up_lim,[],[],Ef_p);
```

```
%This program calculates quantities of interest in slab
wavguides

global ko n_clad w k_prime n_core
w=.22e-4;%cm  where w is the waveguide width
d=0.008e-4;%cm  where d is the QW width
ko=(2*pi/0.98e-4)%cm^-1
n_core=3.52;
n_clad=3.275;
range=[0 pi/2];
answer=fzero('waveguide',range)
k_x=(2/w)*answer
alpha=(2/w)*answer*tan(answer)
confinement=(1+((cos(answer))^2)/((alpha*w/2)*(1+sin(2*answe
r)/(2*answer))))^-1
qw_confinement=(d+k_x^-1*sin(k_x*d))/(w+k_x^-
1*sin(k_x*w)+2*alpha^-1*(cos(k_x*w/2)^2))
```

```
%This program calculates the tunneling I-V characterisitcs

q=1.6e-19;%electron charge in Coulombs
m_electron=9.11e-31;%electron mass in kg
%m_eff=0.063*m_electron;%conduction band electron effective
mass
%m_eff=5.5237e-032;%electron effective mass in 15% InGaAs
h_bar=6.63e-34/(2*pi);%Planck's constant in J*s
k=1.38e-23;%Joules/Kelvin
y=logspace(log10(6e18),20,10);
%Ga mole fraction index
%xstrt=1.0;
%xstp=.85;
%x=xstrt:-.05:xstp;
x=0.15
%materials parameters as a function of Ga mole fraction(=x)
gamma1=6.85.*x + 20.4.*(1.-x);
gamma2=2.1.*x + 8.3.*(1.-x);
C11=11.879.*x + 8.329.*(1.-x);
C12=5.376.*x + 4.526.*(1.-x);
a=-9.77.*x - 6.0.*(1.-x);
b=-1.7.*x - 1.8.*(1.-x);
lattice=5.6533.*x + 6.0584.*(1.-x);
nu=C12./(C11+C12);

%strain values
f=(lattice-5.65325)./lattice;
epsxx=-f;
epsyy=-f;
epszz=-2.*C12.*epsxx./C11;
%Energy gaps and barrier heights for InGaAs QW and AlGaAs
barrier
Egapqw=.324 + .7.*x +.4.*x.^2;
Egapbar=1.424;
Ec_hh=Egapqw+a.*(epsxx+epsyy+epszz)-b/2.*(epsxx+epsyy-
2.*epszz);

%masses for wells and barriers
emwell=(.067.*x + .025.*(1.-x))*m_electron;
hmwell=m_electron./(gamma1-2.*gamma2);

T=300;%room temperature in Kelvin

for l=1:length(x)

   E_gap=Ec_hh(l);
   m_eff_e=emwell(l);
   m_eff_v=hmwell(l);
   m_eff=(m_eff_e^-1+m_eff_v^-1)^-1;


%
%temperature dependent energy gap in eV for GaAs pg 101 of
"Semiconductor basic data" by Madelung
```

```
%E_gap=1.519-5.408e-4*T.^2./(T+204);
%E_gap=1.2782;%Energy gap in 15% InGaAs
N_A=2e19;%Acceptor doping concentration per cubic centimeter
N_D=2e19;%Donor doping concentration per cubic centimeter
N_eff=N_A*N_D/(N_A+N_D);%"reduced" doping
eps=8.854e-14*13.1;%Farads/cm for GaAs
N_c=2.51e19*(m_eff/m_electron)^1.5*(T/300)^1.5;%effective
density of states in the conduction band per cubic
centimeter band-back cover of "Microelectronic devices" by
Yang
N_v=2.51e19*(m_eff_v/m_electron)^1.5*(T/300)^1.5;%effective
density of states in the valence band per cubic centimeter
band-back cover of "Microelectronic devices" by Yang
%V_n=((k*T)/q)*(log(N_D/N_c)+(sqrt(2)/4)*(N_D/N_c)+(3/16-
sqrt(3)/9)*(N_D/N_c)^2+1.48386e-4*(N_D/N_c)^3-4.42563e-
6*(N_D/N_c)^4);%distance Fermi level is above conduction
band edge in Volts
%V_p=((k*T)/q)*(log(N_A/N_v)+(sqrt(2)/4)*(N_A/N_v)+(3/16-
sqrt(3)/9)*(N_A/N_v)^2+1.48386e-4*(N_A/N_v)^3-4.42563e-
6*(N_A/N_v)^4);%distance Fermi level is below valence band
edge in Volts
K_1=4.9;%coefficient in Pade approx.
K_2=sqrt(-2*(3/16-sqrt(3)/9)/K_1);%coefficient in the Pade
approximation
V_n=((k*T)/q)*(log(N_D/N_c)+(1/sqrt(8))*(N_D/N_c)+(K_1*log(1
+K_2*(N_D/N_c))-K_1*K_2*(N_D/N_c)));%Pade approximation for
location of Fermi level
V_p=((k*T)/q)*(log(N_A/N_v)+(1/sqrt(8))*(N_A/N_v)+(K_1*log(1
+K_2*(N_A/N_v))-K_1*K_2*(N_A/N_v)));%Pade approximation for
location of Fermi  level
V_bi=V_n+V_p+E_gap;%built-in potential in (e)Volts due to
doping
V_a=-15*k*T/q:0.1*k*T/q:5*k*T/q;%Range of applied voltages
in volts

for m=1:length(V_a)
   w_depl=sqrt(2*eps*(V_bi-
V_a(m))/(q*N_A*N_D*(N_D+N_A)))*(N_A+N_D);%width of the
depletion region in units of cm
   %E_bi=sqrt(q*V_bi*N_eff/(2*eps));%built in electric field
in V/cm due to doping
   E_bi=2*(V_bi-V_a(m))/w_depl;%'max' built in electric
field in V/cm due to doping

E_bar=(sqrt(2)*h_bar*E_bi*100)/(pi*sqrt(m_eff)*sqrt(E_gap*q)
);%constant defined by Kane in units of eV
   int_coeff=1e-4*q^3*m_eff/(2*pi^2*h_bar^3)*exp(-
pi*sqrt(m_eff)*(E_gap*q)^1.5/(2*sqrt(2)*h_bar*E_bi*100*q));
   E_v(m)=(V_bi-V_a(m)-E_gap)./(k*T/q);%Range of energies
over which to integrate
   E_1=0:0.01:E_v(m)/2;
   E_2=E_v(m)/2:0.01:E_v(m);
```

```
   del_Fermi_1=exp(E_1-V_n/(k*T/q)).*(1-exp(-
V_a(m)./(k*T/q))./((1+exp(E_1-
(V_a(m)+V_n)./(k*T/q))).*(1+exp(E_1-V_n/(k*T/q))));
   del_Fermi_2=exp(E_2-V_n/(k*T/q)).*(1-exp(-
V_a(m)./(k*T/q))./((1+exp(E_2-
(V_a(m)+V_n)./(k*T/q))).*(1+exp(E_2-V_n/(k*T/q))));
   j_1=trapz(E_1,del_Fermi_1.*(1-exp(-
2*E_1/E_bar)).*(E_bar/2));
   j_2=trapz(E_2,del_Fermi_2.*(1-exp(-2*(E_v(m)-
E_2)/E_bar)).*(E_bar/2));
   j(m)=(j_1+j_2)*int_coeff;
end
stripe_width=20e-4;%width of stripe in cm
laser_length=500e-4;%length of laser in cm
i{1}=j*stripe_width*laser_length;
end
figure
%plot(V_a,i{1})
plot(V_a,i{1},V_a,i{2},V_a,i{3}, V_a, i{4})
axis([-0.4 0.1 -140 5])
xlabel('Voltage (Volts)')
ylabel('Current (mA)')


%plot(V_a,E_v)
```

```
%  This program calculates the BCL band diagram

q=1.6e-19;%electron charge in Coulombs
m_electron=9.11e-31;%electron mass in kg
y=0.4;%Aluminum mole fraction
T=300;%System temperature in Kelvin
m_eff_v=(0.50+0.29*y)*m_electron;%valence band electron
effective mass
m_eff_v_t=0.50*m_electron;%valence band hole effective mass
in GaAs tunnel junction
m_eff_c=(0.0665+0.083*y)*m_electron;%conduction band hole
effective mass
m_eff_c_t=0.0665*m_electron;%conduction band electron
effective mass in GaAs tunnel junction
h_bar=6.63e-34/(2*pi);%Planck's constant in J*s
k=1.38e-23;%Boltzmann constant in Joules/Kelvin
E_gap_i=1.424;%Bandgap energy in eV of GaAs intrinsic region
E_gap=(1.424+1.247*y);%Bandgap energy in eV of AlGaAs as a
function of Al mole fraction 'y'
N_A=5e17;%Acceptor doping concentration per cubic centimeter
N_D=5e17;%Donor doping concentration per cubic centimeter
N_D_t=1.478e19;%Donor doping concentration in the tunnel
junction per cubic centimeter
N_A_t=4.28e19;%%Acceptor doping concentration per cubic
centimeter
N_eff=N_A*N_D/(N_A+N_D);%"reduced" doping
eps=8.854e-14*13.1;%Farads/cm for GaAs
eps_cl=(13.1-3.0*y)*8.854e-14;%Farads/cm for AlGaAs
(cladding) of Al mole fraction 'y'

N_c=2.51e19*(m_eff_c/m_electron)^1.5*(T/300)^1.5;%effective
density of states in the conduction band per cubic
centimeter
N_v=2.51e19*(m_eff_v/m_electron)^1.5*(T/300)^1.5;%effective
density of states in the valence band per cubic centimeter
N_c_t=2.51e19*(m_eff_c_t/m_electron)^1.5*(T/300)^1.5;%effect
ive density of states in the conduction band per cubic
centimeter
N_v_t=2.51e19*(m_eff_v_t/m_electron)^1.5*(T/300)^1.5;%effect
ive density of states in the valence band per cubic
centimeter band
K_1=4.9;%coefficient in Pade approx.
K_2=sqrt(-2*(3/16-sqrt(3)/9)/K_1);%coefficient in the Pade
approximation
V_n=((k*T)/q)*(log(N_D/N_c)+(1/sqrt(8))*(N_D/N_c)+(K_1*log(1
+K_2*(N_D/N_c))-K_1*K_2*(N_D/N_c)));%Pade approximation for
location of Fermi level
V_p=((k*T)/q)*(log(N_A/N_v)+(1/sqrt(8))*(N_A/N_v)+(K_1*log(1
+K_2*(N_A/N_v))-K_1*K_2*(N_A/N_v)));%Pade approximation for
location of Fermi  level
V_n_t=((k*T)/q)*(log(N_D_t/N_c_t)+(1/sqrt(8))*(N_D_t/N_c_t)+
(K_1*log(1+K_2*(N_D_t/N_c_t))-K_1*K_2*(N_D_t/N_c_t)));%Pade
approximation for location of Fermi level
```

```
V_p_t=((k*T)/q)*(log(N_A_t/N_v_t)+(1/sqrt(8))*(N_A_t/N_v_t)+
(K_1*log(1+K_2*(N_A_t/N_v_t))-K_1*K_2*(N_A_t/N_v_t)));%Pade
approximation for location of Fermi  level
V_bi=V_n+V_p+E_gap;%built-in potential in (e)Volts due to
doping across the laser p-i-n structure

del_E_gap=E_gap-E_gap_i;%Bandgap difference between cladding
and intrinsic region
del_E_v=0.33*del_E_gap;%Bandgap offset at valence band
del_E_c=0.67*del_E_gap;%Bandgap offset at conduction band

V_bi_n_t=del_E_c-V_n_t+V_n%built-in potential in (e)Volts
due to doping at n-cladding to n-tunnel
V_bi_p_t=del_E_v-V_p_t+V_p%built-in potential in (e)Volts
due to doping at p-cladding to p-tunnel

x_i=0.22e-4;%intrinsic layer width in cm
x_p=(-
q*N_A*x_i/eps+sqrt((q*N_A*x_i/eps)^2+4*(q*N_A/eps_cl)*V_bi))
/(2*q*N_A/eps);%depletion region on the p-cladding side
x_n=x_p*(N_A/N_D);%depletion region on the n-side of the
cladding
x_cl=0.75e-4;%width of cladding region in cm
x_flat_p=x_cl-x_p;%width of undepleted region in p-type
cladding
x_flat_n=x_cl-x_n;%width of undepleted region in n-type
cladding

del=0.01e-4;%spatial increment
x_1=-x_flat_p:del:-x_p;%flat p-region
x_2=-x_p:del/100:0;%depleted p-region
x_3=0:del:x_i;%intrinsic region
x_4=x_i:del/100:x_n+x_i;%depleted n-region
x_5=x_i+x_n:del:x_i+x_n+x_flat_n;%flat n-region


E_v(1:length(x_1))=0;%flat region
E_v(length(E_v)+1:length(E_v)+length(x_2))=-
q*N_A*(x_2+x_p).^2/(2*eps_cl);%p-depletion
E_v(length(E_v)+1:length(E_v)+length(x_3))=del_E_v-
q*N_A*x_p^2/(2*eps_cl)-q*N_A*x_p*x_3/eps;%intrinsic
E_v(length(E_v)+1:length(E_v)+length(x_4))=-q*N_A*x_p^2-
q*N_A*x_p*x_i/eps-q*N_D/(2*eps_cl)*(2*x_n*(x_4-x_i)-(x_4-
x_i).^2);%n-depletion
E_v(length(E_v)+1:length(E_v)+length(x_5))=-q*N_A*x_p^2-
q*N_A*x_p*x_i/eps-q*N_D/(2*eps_cl)*x_n^2;

del_active=length(E_v);

E_c(1:length(x_1)+length(x_2))=E_v(1:length(x_1)+length(x_2)
)+E_gap;
E_c(length(E_c)+1:length(E_c)+length(x_3))=E_v(length(E_c)+1
:length(E_c)+length(x_3))+E_gap_i;
```

```
E_c(length(E_c)+1:length(E_c)+length(x_4)+length(x_5))=E_v(l
ength(E_c)+1:length(E_c)+length(x_4)+length(x_5))+E_gap;

x_n_cl=sqrt((2*eps_cl/(q*N_D))*(V_bi_n_t-k*T/q));%depletion
width (in cm) in n-cladding at junction to n-side of tunnel
junction
x_p_cl=sqrt((2*eps_cl/(q*N_A))*(V_bi_p_t-k*T/q));%depletion
width (in cm)in p-cladding at junction tp p-side of tunnel
junction

%x_6=-x_n_cl:del/100:0;%depleted region in n-cladding at the
junction of n-cladding to n-tunnel
%E_v(length(E_v)+1:length(E_v)+length(x_6))=E_v(length(E_v))
-q*N_D*(x_6+x_n_cl).^2;%Valence band energy in the cladding
at junction to n-tunnel
%E_c(length(E_c)+1:length(E_c)+length(x_6))=E_v(length(E_c)+
1:length(E_c)+length(x_6))+E_gap;%Conduction band energy in
depleted region
%x_6=x_6+max(x_5);%reset the position


V_bi_t=V_n_t+V_p_t+E_gap_i;%built-in potential in tunnel
homojunction
x_p_t=sqrt(2*eps*V_bi_t/(q*N_A_t*N_D_t*(N_D_t+N_A_t)))*N_D_t
;%depletion region on the p-side of the tunnel junction
x_n_t=x_p_t*N_A_t/N_D_t;%depletion region on the n-side of
the tunnel junction
x_7=-x_n_t:del/1000:0;%depleted n-region of the tunnel
junction
x_8=0:del/1000:x_p_t;%depleted p-region of the tunnel
junction
E_v(length(E_v)+1:length(E_v)+length(x_7))=E_v(length(E_v))+
del_E_v+q*N_D_t/(2*eps)*(x_7+x_n_t).^2;
E_c(length(E_c)+1:length(E_c)+length(x_7))=E_v(length(E_c)+1
:length(E_c)+length(x_7))+E_gap_i;
E_v(length(E_v)+1:length(E_v)+length(x_8))=E_v(length(E_v))+
q*N_A_t/(2*eps)*(2*x_8*x_p_t-x_8.^2);
E_c(length(E_c)+1:length(E_c)+length(x_8))=E_v(length(E_c)+1
:length(E_c)+length(x_8))+E_gap_i;
x_7=x_7+max(x_5)+x_n_t;
x_8=x_8+max(x_7);

E_v(length(E_v)+1:length(E_v)+del_active)=E_v(1:del_active);
E_c(length(E_c)+1:length(E_c)+del_active)=E_c(1:del_active);

z=[x_1 x_2 x_3 x_4 x_5];
x_9=max(x_8)-min(x_1)+z;

x=[x_1 x_2 x_3 x_4 x_5 x_7 x_8 x_9];
plot(x,E_v,x,E_c)
```

```
% This program calculates the thrshold current for the
%ARROW BCL

q=1.6e-19;
N_w=10;
w=0.007e-4;
B=0.22e-10;
C=9e-29;
N_tr=1.82*1e18;
eta_i=0.80;
L=500e-4;
R1=0.32;
R2=0.95
g_o=1864;
alpha_m=(1/(2*L))*log((R1*R2)^-1);
%alpha_r=[38.7 20.0 11.0 6.4 3.8 2.4 1.6 1.0 0.7]/3;

%gamma=[0.0265 0.0263 0.0212 0.0193 0.0177 0.0163 0.0152
0.0142 0.0133]
%core_width=[2 2.25 2.5 2.75 3.0 3.25 3.5 3.75 4.00]



J_th=(q*N_w*w*B*N_tr^2/eta_i)*exp(2*(alpha_i+alpha_r+alpha_m
)./(gamma*g_o))+(q*w*N_w*C*N_tr^3/eta_i)*exp(3*(alpha_i+alph
a_r+alpha_m)./(gamma*g_o));
plot(core_width,J_th)

[haxes, hline1,hline2]=plotyy(core_width, J_th, core_width,
alpha_r)
xlabel('Core width (microns)')
title('Single core ARROW at 1.55 microns')
%xlabel('Core width (microns)')
%ylabel('Threshold current density (A/cm^2)')
```

```
% This program finds the ARROW resonances

for m=1:21
   core_width=2.0+0.1*(m-1);
   corewidth(m)=core_width

qrtr_lambda_o=core_width/2;

n_o=3.17;
n_1=3.4;

%lambda=linspace(1,1000,100000);
lambda=1.55;

s=sqrt((4*(n_1^2-n_o^2)/lambda^2+core_width^-2)^-1)
three_qrtr_lambda_1=3*s/2

theta_o=linspace(0,pi/2,10000);
theta_1=asin(n_o*sin(theta_o)/n_1);

%theta_o=0;
%theta_1=0;

r_o_to_1=(n_o*cos(theta_o)-
n_1*cos(theta_1))./(n_o*cos(theta_o)+n_1*cos(theta_1));
%t_o_to_1=2*sqrt(n_o*n_1*cos(theta_o).*cos(theta_1))./(n_o*c
os(theta_o)+n_1*cos(theta_1));
%t_1_to_o=2*sqrt(n_o*n_1*cos(theta_o).*cos(theta_1))./(n_o*c
os(theta_o)+n_1*cos(theta_1));
t_o_to_1=2*n_o*cos(theta_o)./(n_o*cos(theta_o)+n_1*cos(theta
_1));
t_1_to_o=2*n_1*cos(theta_1)./(n_o*cos(theta_o)+n_1*cos(theta
_1));
r_1_to_o=-r_o_to_1;
k_x_1=2*pi*n_1*cos(theta_1)./lambda;
k_x_o=2*pi*n_o*cos(theta_o)./lambda;


phase_core=j*k_x_o*core_width;
phase_three_qrtr_lambda_1=j*k_x_1*three_qrtr_lambda_1;
phase_qrtr_lambda_o=j*k_x_o*qrtr_lambda_o;

spacer(m)=s;
three_qrtr_layer(m)=three_qrtr_lambda_1;
for i=1:length(theta_o)
T_o_to_1=(1/t_o_to_1(i))*[1 r_o_to_1(i); r_o_to_1(i) 1];
T_1_to_o=(1/t_1_to_o(i))*[1 r_1_to_o(i); r_1_to_o(i) 1];

T_core=[exp(phase_core(i)) 0; 0 exp(-phase_core(i))];
T_three_qrtr_lambda_1=[exp(phase_three_qrtr_lambda_1(i)) 0;
0 exp(-phase_three_qrtr_lambda_1(i))];
T_qrtr_lambda_o=[exp(phase_qrtr_lambda_o(i)) 0; 0 exp(-
phase_qrtr_lambda_o(i))];
```

```
whole_structure=T_1_to_o*T_qrtr_lambda_o*T_o_to_1*T_three_qr
tr_lambda_1*T_1_to_o*T_core*T_o_to_1*T_three_qrtr_lambda_1*T
_1_to_o*T_qrtr_lambda_o*T_o_to_1;
reflector_structure=T_o_to_1*T_three_qrtr_lambda_1*T_1_to_o*
T_qrtr_lambda_o*T_o_to_1;

Structure_Transmistivity(i)=(whole_structure(1,1)*whole_stru
cture(1,1)')^-1;
Transmistivity(i)=(reflector_structure(1,1)*reflector_struct
ure(1,1)')^-1;
Reflectivity(i)=1-Transmistivity(i);
alpha(i)=2*log(Reflectivity(i)^-
1)*lambda*1e4/((2*n_o*core_width^2)*sqrt(1-
(lambda/(2*n_o*core_width))^2));
end
for i=1000:length(theta_o)
   alpha_prime(i)=2*1e4*log(Reflectivity(i)^-
1)/(2*core_width*tan(theta_o(i)));
end


%figure
%plot(theta_o*180/pi, Reflectivity,'-g');
%xlabel('Propagation Angle in Core')
%ylabel('Single Reflector Reflectivity')
%figure
%plot(theta_o*180/pi, Transmistivity);
%xlabel('Propagation Angle in Core')
%ylabel('Single Reflector Transmistivity')
%figure
%plot(theta_o(1000:length(theta_o))*180/pi,alpha(1000:length
(theta_o)));
%xlabel('Propagation Angle in Core')
%ylabel('Loss___ (cm^-1)')
%figure
%plot(theta_o*180/pi,alpha);
%xlabel('Propagation Angle in Core')
%ylabel('Loss (cm^-1)')
%figure
%plot(theta_o*180/pi, Structure_Transmistivity);
%xlabel('Propagation Angle in Core')
%ylabel('Structure Transmistivity')

theta_res=acos(lambda/(2*n_o*core_width));
theta_o_prime=theta_o-theta_res;
index=find(min(abs(theta_o_prime))==abs(theta_o_prime));
loss(m)=alpha(index)


w=0.007;%QW width
b=0.009;%Barrier width

gamma_1=(w+core_width*sin(pi*w/core_width)/pi)/(core_width+c
ore_width/pi);
```

```
gamma_2=(w+core_width*sin(pi*(b+3*w/2)/core_width)/pi-
core_width*sin(pi*(b+w/2)/core_width)/pi)/(core_width+core_w
idth/pi);

gamma_3=(w+core_width*sin(pi*(2*b+5*w/2)/core_width)/pi-
core_width*sin(pi*(2*b+3*w/2)/core_width)/pi)/(core_width+co
re_width/pi);

gamma(m)=gamma_1+2*(gamma_2+gamma_3)
end
core_width=corewidth
alpha_r=loss
gamma
spacer
three_qrtr_layer
```

```
%This program calculates the farfield information for a
%three core ARROW-BCL

for k=1:21
core_width=1.9+0.1*k;%in microns
qrtr_lambda_o_width=core_width/2;%in microns
num_cores=3;
num_spacers=2;
num_qrtr_wave_reflec=2;
num_three_qrtr_wave_reflec=2;

lambda=1.55;

n_o_=3.17;%index of core
n_1_=3.4;%index of spacer
theta_o=acos(lambda/(2*core_width*n_o_));
%theta_o=82.3*pi/180;
theta_1=asin((n_o_/n_1_)*sin(theta_o));

spacer_width=sqrt((4*(n_1_^2-n_o_^2)/(lambda^2)+core_width^-
2)^-1)%in microns
three_qrtr_lambda_o_=3.17;%index of core
three_qrtr_lambda_1_width=(3/2)*spacer_width;%in microns

n_o=3.17*cos(theta_o);%effective index for low index
material
n_1=3.4*cos(theta_1);%effective index for high index
material
device_width=num_cores*core_width+num_spacers*spacer_width+n
um_qrtr_wave_reflec*qrtr_lambda_o_width+...
   num_three_qrtr_wave_reflec*three_qrtr_lambda_1_width;

%spacer_width=spacer_width*3;
r_o_to_1=(n_o-n_1)/(n_o+n_1);%reflection coefficient going
from material of index n_o to material of index n_1
t_o_to_1=2*(n_o)/(n_o+n_1);%transmission coefficient going
from material of index n_o to material of index n_1
t_1_to_o=2*(n_1)/(n_o+n_1);%transmission coefficient going
from material of index n_o to material of index n_1
r_1_to_o=-r_o_to_1;%reflection coefficient for wave
propogating from material of index n_1 to material of index
n_o
k_x_1=2*pi*n_1/lambda;%transverse k-vector in material of
index n_1
k_x_o=2*pi*n_o/lambda;%transverse k-vector in material of
index n_o

x=linspace(-device_width/2,device_width/2,4096);
ind{1}=[1:max(find(-device_width/2+qrtr_lambda_o_width>x))];
ind{2}=[max(ind{1})+1:max(find((-
device_width/2+qrtr_lambda_o_width+three_qrtr_lambda_1_width
)>x))];
```

```
ind{3}=[max(ind{2})+1:max(find((-
device_width/2+qrtr_lambda_o_width+three_qrtr_lambda_1_width
+core_width)>x))];
ind{4}=[max(ind{3})+1:max(find((-
device_width/2+qrtr_lambda_o_width+three_qrtr_lambda_1_width
+core_width+spacer_width)>x))];
ind{5}=[max(ind{4})+1:max(find((-
device_width/2+qrtr_lambda_o_width+three_qrtr_lambda_1_width
+2*core_width+spacer_width)>x))];
ind{6}=[max(ind{5})+1:max(find((-
device_width/2+qrtr_lambda_o_width+three_qrtr_lambda_1_width
+2*core_width+2*spacer_width)>x))];
ind{7}=[max(ind{6})+1:max(find((-
device_width/2+qrtr_lambda_o_width+three_qrtr_lambda_1_width
+3*core_width+2*spacer_width)>x))];
ind{8}=[max(ind{7})+1:max(find((-
device_width/2+qrtr_lambda_o_width+2*three_qrtr_lambda_1_wid
th+3*core_width+2*spacer_width)>x))];
ind{9}=[max(ind{8})+1:4096];

index(ind{1})=n_o_;
index(ind{2})=n_1_;
index(ind{3})=n_o_;
index(ind{4})=n_1_;
index(ind{5})=n_o_;
index(ind{6})=n_1_;
index(ind{7})=n_o_;
index(ind{8})=n_1_;
index(ind{9})=n_o_;

phase_core=k_x_o*core_width;
phase_spacer=k_x_1*spacer_width;
phase_three_qrtr_lambda_1=k_x_1*three_qrtr_lambda_1_width;
phase_qrtr_lambda_o=k_x_o*qrtr_lambda_o_width;

T_o_to_1=(1/t_o_to_1)*[1 r_o_to_1; r_o_to_1 1];
T_1_to_o=(1/t_1_to_o)*[1 r_1_to_o; r_1_to_o 1];

T_core=[exp(i*phase_core) 0; 0  exp(-i*phase_core)];
T_spacer=[exp(i*phase_spacer) 0; 0  exp(-i*phase_spacer)];
T_three_qrtr_lambda_1=[exp(i*phase_three_qrtr_lambda_1) 0; 0
exp(-i*phase_three_qrtr_lambda_1)];
T_qrtr_lambda_o=[exp(i*phase_qrtr_lambda_o) 0; 0 exp(-
i*phase_qrtr_lambda_o)];

input=[0;i];


qrtr_field_r=T_qrtr_lambda_o*T_o_to_1*input;
three_qrtr_field_r=T_three_qrtr_lambda_1*T_1_to_o*qrtr_field
_r;
core_field_r=T_core*T_o_to_1*three_qrtr_field_r;
spacer_field_r=T_spacer*T_1_to_o*core_field_r;
core_field_c=T_core*T_o_to_1*spacer_field_r;
```

```
spacer_field_1=T_spacer*T_1_to_o*core_field_c;
core_field_1=T_core*T_o_to_1*spacer_field_1;
three_qrtr_field_1=T_three_qrtr_lambda_1*T_1_to_o*core_field
_1;
qrtr_field_1=T_qrtr_lambda_o*T_o_to_1*three_qrtr_field_1;
output=T_1_to_o*qrtr_field_1;


AB_9=qrtr_field_r;
AB_8=three_qrtr_field_r;
AB_7=core_field_r;
AB_6=spacer_field_r;
AB_5=core_field_c;
AB_4=spacer_field_1;
AB_3=core_field_1;
AB_2=three_qrtr_field_1;
AB_1=qrtr_field_1;
AB_0=output;

AB=[AB_1,AB_2,AB_3,AB_4,AB_5,AB_6,AB_7,AB_8,AB_9];

k_vector=[k_x_o, k_x_1, k_x_o, k_x_1, k_x_o, k_x_1, k_x_o,
k_x_1, k_x_o];

z=x;

for m=1:9
   y(ind{m})=AB(1,m)*exp(-i*k_vector(m)*(z(ind{m})-
z(min(ind{m})))) + AB(2,m)*exp(i*k_vector(m)*(z(ind{m})-
z(min(ind{m}))));
end

maximum=max(abs(y));
y_prime=y/max(real(y));
[haxes, hline1, hline2]=plotyy(z,(real(y_prime)).^2, z,
index)
axes(haxes(1))
axis([min(z) max(z) 0 1])
ylabel('Near field intensity (arb units)')
axes(haxes(2))
axis([min(z) max(z) 3.1 3.47])
ylabel('Index')
xlabel('Microns')
figure
doubley(z,index,real(y))
doubley(z,index,(real(y)).^2)


AB_0;


theta_far=linspace(-pi/4,pi/4,length(z));
arg=i*2*pi*sin(theta_far);
for 1=1:length(theta_far)
```

```
    integrand=y.*exp(arg(l)*z);
    far_field_trap(l)=cos(theta_far(l))*trapz(z,integrand);
end
figure
far_field_trap_prime=far_field_trap/max(real(far_field_trap)
);
plot(180*theta_far/pi,real(far_field_trap_prime))
figure
plot(180*theta_far/pi,(real(far_field_trap_prime)).^2)
%half_main_lobe_power(k)=trapz(theta_far(find(max(abs(real(f
ar_field_trap)))==abs(real(far_field_trap))):find(min(abs(re
al(far_field_trap(length(theta_far)/2:...
%
max(find(theta_far<=7*pi/180))))))==abs(real(far_field_trap)
))),...
%(abs(real(far_field_trap(find(max(abs(real(far_field_trap))
)==abs(real(far_field_trap))):find(min(abs(real(far_field_tr
ap(length(theta_far)/2:...
%
max(find(theta_far<=7*pi/180))))))==abs(real(far_field_trap)
))))))).^2);
half_total_power(k)=trapz(theta_far,(real(far_field_trap)).^
2)/2;
%percent_main_lobe(k)=half_main_lobe_power(k)/half_total_pow
er(k)

near_total_power(k)=trapz(z,(real(y)).^2);
gamma_qrtr_lambda_o(k)=(trapz(z(min(ind{1}):max(ind{1})),(re
al(y(min(ind{1}):max(ind{1})))).^2)/(near_total_power(k)))*2
;
gamma_three_qrtr_lambda_1(k)=(trapz(z(min(ind{2}):max(ind{2}
)),(real(y(min(ind{2}):max(ind{2})))).^2)/(near_total_power(
k)))*2;
gamma_spacer(k)=(trapz(z(min(ind{4}):max(ind{4})),(real(y(mi
n(ind{4}):max(ind{4})))).^2)/(near_total_power(k)))*2;
gamma_core(k)=(trapz(z(min(ind{3}):max(ind{3})),(real(y(min(
ind{3}):max(ind{3})))).^2)/(near_total_power(k)))*3;
end

%main_lobe=percent_main_lobe
gamma_qrtr_reflec=gamma_qrtr_lambda_o
gamma_three_qrtr_reflec=gamma_three_qrtr_lambda_1
gamma_s=gamma_spacer
gamma_element=gamma_core
gamma_total=gamma_qrtr_reflec+gamma_three_qrtr_reflec+gamma_
s+gamma_element

n_doping=5e17;
p_doping=5e17;
n_loss=3*n_doping/1e18;
p_loss=35*p_doping/1e18;
alpha_i=(gamma_qrtr_reflec+gamma_three_qrtr_reflec+gamma_s)*
(n_loss+p_loss)/2
```

```
%doubley(z,index,real(y_prime))
%ylabel('Intensity (arb)')

%Nsamples = length(y);
%Nfft = 2^18;
%fourier_xfm=fft(y,Nfft);
%del_x=device_width/Nsamples;
%range=floor(del_x*Nfft/lambda);
%m=1:range;
%theta_x=asin(lambda*(m-1)/(del_x*Nfft));
%far_field=cos(theta_x).*fourier_xfm(1:range);
%theta_x_minus=-theta_x;
%theta_x_minus=theta_x_minus(length(theta_x_minus):-1:1);
%thetax=[theta_x_minus theta_x];
%far_field_reverse=far_field(length(far_field):-1:1);
%farfield=[far_field_reverse far_field];
%figure
%plot(180*thetax/pi,real(farfield)/max(real(farfield)));
%figure
%plot(180*thetax/pi,(real(farfield)/max(real(farfield))).^2)
;

%axis([0 1 min(real(farfield)) max(real(farfield))])
%first_zero=min(find(min(abs(real(far_field(1:35))))==abs(re
al(far_field(1:35)))))
%center=max(find(max(abs(real(far_field)))==abs(real(far_fie
ld))));
%half_main_lobe_power=trapz(theta_x(center:first_zero),(real
(far_field(center:first_zero))).^2);
%half_total_power=trapz(theta_x,(real(far_field)).^2);
%percent_main_lobe=half_main_lobe_power/half_total_power
```